Dissertationen aus der Naturwissenschaftlich-Technischen
Fakultät der Universität des Saarlandes

CO Gas Sensor for Consumer Electronic Applications

Elisabeth Margarethe Preiß

universaar
Universitätsverlag des Saarlandes
Saarland University Press
Presses Universitaires de la Sarre

Elisabeth Margarethe Preiß

CO Gas Sensor for Consumer Electronic Applications

universaar
Universitätsverlag des Saarlandes
Saarland University Press
Presses Universitaires de la Sarre

D 291
Dissertation zur Erlangung des Grades der Doktorin der Ingenieurwissenschaften
der Naturwissenschaftlich-Technischen Fakultät der Universität des Saarlandes
Dekan: Prof. Dr. Guido Kickelbick

Berichterstatter: Prof. Dr. Helmut Seidel, Prof. Dr. Udo Weimar
Vorsitz: Prof. Dr. Chihao Xu
Akad. Mitarbeiter: Dr. Tilman Sauerwald

Tag des Kolloquiums: 18.01.2018

Universitätsverlag des Saarlandes
Saarland University Press
Presses Universitaires de la Sarre

Postfach 151150, 66041 Saarbrücken

ISBN 978-3-86223-272-7 gedruckte Ausgabe
ISBN 978-3-86223-273-4 Onlineausgabe
URN urn:nbn:de:bsz:291-universaar-1803

Projektbetreuung *universaar*: Matthias Müller

Satz: Elisabeth Margarethe Preiß
Umschlaggestaltung: Julian Wichert

Bibliografische Information der Deutschen Nationalbibliothek:
Die Deutsche Nationalbibliothek verzeichnet diese Publikation in der Deutschen Nationalbibliografie; detaillierte bibliografische Daten sind im Internet über <http://dnb.d-nb.de> abrufbar.

In memory of Sophie Taeuber-Arp, artist, (*1889 Davos–†1943 Zürich) who was found dead by CO poisoning.

Es war Sophie Taeuber, die mir durch das Beispiel ihrer klaren Arbeiten und ihres klaren Lebens den rechten Weg, den Weg zur Schönheit, zeigte. In dieser Welt bestehen Oben und Unten, Helligkeit und Dunkelheit, Ewigkeit und Vergänglichkeit in vollendetem Gleichgewicht. So schloss sich der Kreis. Hans Arp

...and experience can't be replaced by anything... Raman Kashyap, Professor, Ecole Polytechnique de Montréal

Kurzzusammenfassung

Gassensoren in Smartphones und anderen mobilen Geräten haben das Potential, zukünftig Lebensqualität und Sicherheit zu verbessern. Dafür ist ein hoher Grad an Miniaturisierung und die Reduzierung der Leistungsaufnahme notwendig. In dieser Arbeit wurden verschiedene Aspekte miniaturisierter, resistiver CO-Sensoren auf Basis von Metalloxiden (MOX) untersucht. Herstellung erfolgte mit gepulster Laserabscheidung (PLD) auf Platinstrukturen, die mit einem Lift-Off-Prozess strukturiert wurden. Per Simulation und Experiment wurden Einflüsse der Lackgeometrie auf die Metallstruktur aufgezeigt. Bei den untersuchten MOX-Dünnschichten lag der Fokus auf SnO_2. Dessen elektrische und gassensitive Eigenschaften hängen stark von den Abscheidungsbedingungen ab: Höhere Abscheidungsdrücke (>10 Pa) führen zu höheren Grundwiderständen sowie zu einem höheren Signal für CO in trockener Luft. Diese Eigenschaften korrelieren mit der nanoporösen Morphologie des Materials. Bei Messungen in feuchter Luft reduzierte sich das CO-Signal im Vergleich zu trockener Luft. Durch den per Sputtern aufgebrachten Zusatz von Edelmetallen, insbesondere von Palladium (Pd), konnten die Eigenschaften deutlich verbessert werden. CO-Sensitivität in feuchter Luft konnte für hochporöses WO_3 ebenfalls gezeigt werden. In einer Parameterstudie wurde in Experiment und Simulation zudem der Einfluss der geheizten Membrangeometrie auf die Leistungsaufnahme des Sensors untersucht.

Abstract

Gas sensors in smartphones and other mobile devices have the potential to contribute to improving the quality of life and security. This calls for a high degree of miniaturization and a reduction in power consumption. In this work, various aspects of miniaturized, resistive CO gas sensors based on metal oxides (MOX) were investigated. Deposition took place through pulsed laser deposition (PLD) on structures of platinum that were patterned using a lift-off process. The influence of the resist geometry on the metal structures was demonstrated by experiment and simulation. With regard to the MOX thin films, the focus was set on SnO_2. Both its electrical and gas-sensing properties were highly influenced by the deposition parameters: Higher deposition pressures (>10 Pa) are leading to higher base resistances and to a higher sensor signal for CO in dry air. These properties correlated with the nanoporous morphology of the material. For measurements in humid air, the response to CO was reduced compared to dry air. Different noble metal additives, in particular Pd, were introduced by sputtering, thereby significantly improving properties. CO-sensitivity in humid air was also demonstrated for highly porous WO_3. In a parameter study, the impact of the heated membrane geometry on the power consumption of the sensor was further investigated in simulation and experiment.

Contents

List of Acronyms and Abbreviations

Al_2O_3	aluminum oxide
CH_4	methane
CO_2	carbon dioxide
Co_3O_4	cobalt oxide
Cr_2O_3	chromium oxide
CuO	copper oxide
Ga_2O_3	gallium oxide
H_2	hydrogen dioxide
In_2O_3	indium oxide
NO_2	nitrogen dioxide
NO_x	nitrogen oxide
NiO	nickel oxide
SnO_2	tin dioxide
TiO_2	tintanium oxide
WO_3	tungsten trioxide
ZnO	zinc oxide
AFM	atomic force microscopy
Ag	silver
ALD	atomic layer deposition
ArF	argon fluorite
Au	gold
CO	carbon monoxide
CVD	chemical vapor deposition
DC	direct current
DFT	density functional theory
DRIE	deep reactive ion etching
DRIFTS	diffuse reflectance infrared Fourier transform spectroscopy
EC	electrochemical cell
FEM	finite element method
FFT	fast Fourier transformation
HMDS	hexamethyldisilazane

HRTEM	high resolution transmission electron microscopy
IC	integrated circuit
IDE	interdigitated electrode
ITO	indium tin oxide
IV	current-voltage
KOH	potassium hydroxide
KrF	krypton fluorite
LOR	lift-off resist
LPG	liquified petroleum gas
MAK	Maximale Arbeitsplatzkonzentration
MEMS	microelectromechanical systems
MFC	mass flow controller
MFM	mass flow meter
MOX	metal oxide
Nd:glass	neodymium-doped glass
Nd:YAG	neodymium-doped yttrium aluminium garnet
OSHA	Occupational Safety and Health Administration
Pd	palladium
PdO	palladium oxide
PECVD	plasma enhanced chemical vapor deposition
PEL	legal airborne permissible exposure limit
PLD	pulsed laser deposition
ppm	parts per million
Pt	platinum
PTFE	polytetrafluorethylene
PVD	physical vapor deposition
r.h.	relative humidity
RF	radio frequency
RGTO	rheotaxial growth and thermal oxidation
RT	room temperature
sccm	standard cubic centimeters per minute

SEM	scanning electron microscopy
TCR	temperature coefficient of resistance
TEM	transmission electron microscopy
Ti	titanium
TLM	transmission line measurement
TMAH	tetramethylammonium hydroxide
XeCl	xenon chloride
XPS	X-ray photoelectron spectroscopy
XRD	X-ray diffraction

List of Symbols

A	constant specific for the sensor signal
a	membrane edge length
α	coefficient for the ionization state of oxygen
α_1	angle of the deposition flux seen by the surface
α_{abs}	sublimation enthalpy
α_{T}	temperature coefficient of resistance
A_{M}	meander area
A_{reduced}	reduced membrane area
A_{S}	effective source surface
b	distance between stripes in TLM
β	surface angle
c	gas concentration
C_{e}	heat capactity of electrons
C_{l}	heat capactity of lattice
D	target-to-substrate distance
d	layer thickness
ΔH_{s}	sublimation enthalpy
d_{lat}	lattice spacing in XRD
E_0	acceptor level energy
E_{C}	conduction band energy
E_{F}	Fermi energy
ϵ	emissivity
ϵ_0	vacuum permittivity
ϵ_r	relative permittivity
E_{V}	valence band energy
E_{Vac}	energy of vacuum level
F_{mass}	mass flow
F_{th}	erosion threshold fluence
F_{volume}	volume flow
G	Gibbs free energy
γ	surface inclination
γ_1	coefficient typical for the morphology
γ_{el}	coupling-constant of electron-lattice
H	enthalpy
h_1	thickness of the LOR
h_2	upper resist layer thickness
I	current
J	atomic flux

k	scaling factor dependent on the sputtering rate
k^*	scaling factor
k_{ads}	adsorption constant
κ	parameter specific for the sensor sensitivity
k_{B}	Boltzmann constant
k_{des}	desorption constant
λ	wavelength
λ_{air}	thermal conductivity of the air
λ_{D}	Debye length
λ_{m}	thermal conductivity of the membrane
λ_{th}	thermal conductivity
M	molar mass
n_{S}	concentration of surface electrons
O(l)	lattice oxygen atom at a surface bridging place
O_{O}	oxygen atom at an oxygen lattice place
p	pressure
Φ	work function
p_{O_2}	oxygen deposition pressure
Q	heat flux
q	elementary charge
$Q_{\text{conduction}}$	heat flux through heat conduction through the air
Q_{membrane}	heat flux through membrane
$Q_{\text{radiation}}$	heat flux through radiation
R	resistance
r_{grain}	radius of cylindrical grains
R_0	resistance prior to gas exposure
R_{contact}	contact resistance
R_{gas}	resistance under gas exposure
r_{heater}	heater radius
ρ	density
ρ_{air}	gas density of air
ρ_{r}	resistivity
r_{a}	atmospheric radius
r_{membrane}	membrane radius
R	distance to the source element
R_{r}	reflectivity
R_{s}	gas constant for air
$R_{\square}$	sheet resistance
R_{total}	total resistance in TLM
S	entropie

σ	Stefan-Boltzmann constant
Sn^+	Sn Lewis site
Sn_{Sn}	tin atom at a tin lattice place
S_{oxid}	sensor signal to oxidizing gases
S_{red}	sensor signal to reducing gases
S_s	surface site
S_t	total concentration of surface sites
T	temperature
t_{90}	response time
T_{amb}	ambient temperature
τ_e	relaxation time constant of electrons
τ_l	relaxation time constant of lattice
T_{dep}	deposition temperature
θ	surface coverage
θ_{inc}	angle of incidence in XRD
T_{hot}	heater temperature
T_m	melting temperature
T_r	relative temperature
U	voltage
u	undersputtering length
v	undercut length
$V_O^{\bullet\bullet}$	double-ionized oxygen vacancy
V_S	surface potential
w	width
w_1	lithography width
w_2	lift-off width
X	electron affinity
z_0	depth of the surface depletion layer

1. Introduction

1.1. Motivation

Devices based on modern electronics increasingly support our daily life. Whether in the car, at the workplace or in the household—these devices are equipped with numerous sensors and output options. They might either be optical in nature like (touch)-displays or acoustic like voice entry and output. Most of the miniaturized sensors in such systems measure physical values. The sense of smell is typically neither stimulated [1] nor can electronic devices such as smartphones detect smells [2]. Gas sensors or chemical sensors in general can measure with great precision, but the effort is usually high. Sensors with a high selectivity—i.e. having a good ability to differ between different gases, for instance spectroscopic sensors—are often large and difficult to handle. Compact chemical sensors have great potential for use in future applications. In many cases, it is not only practical but also necessary to detect certain gases, e.g. in alarm systems for explosive and toxic gases. Here, the gas sensors used have a small footprint, but they are also maintenance free and gas sensitive, though not temperature sensitive. Quite often semiconducting metal oxide (MOX) sensors are applied [3].

Carbon monoxide (CO) is an odorless, toxic gas that can cause headache, dizziness, and fatigue even in very low concentrations. The *legal airborne permissible exposure limit (PEL)* is 50 ppm given by OSHA[1] [4]. In Germany PEL, is defined as *Maximale Arbeitsplatzkonzentration (MAK)*, and only 30 ppm of CO exposure is permitted [5]. The number of CO-induced fatalities in the US and in Germany is in the range of several hundreds every year [6, 7]. CO is found as a by-product of incomplete combustion, e.g. from oil and gas burners and combustion engines. Exemplary use cases of miniaturized CO sensors are provided in Figure 1.1. These include home safety, city/parking, and early fire detection. The sensor can be either integrated in a mobile device such as a smartphone or in a local sensor node.

[1] Occupational Safety and Health Administration (OSHA); parts per million (ppm): A volume concentration unit frequently used for gases, equal to ml/m^3. The PEL is averaged over an eight-hour work-shift.

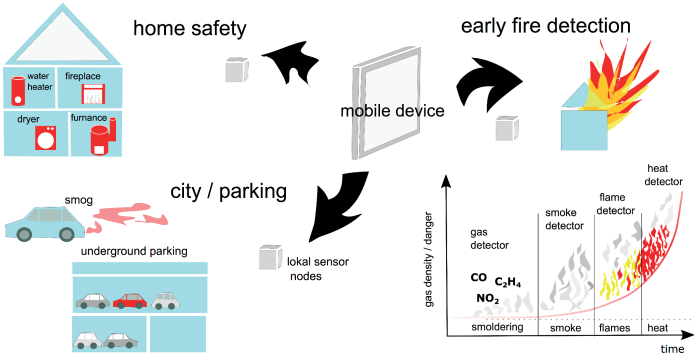

Figure 1.1. Illustration of exemplary use cases for miniaturized CO sensors; parts are adopted from [8].

1.2. CO-Detection Principles

Besides MOX, popular principles for CO-detectors include electrochemical cells (ECs) and colorimetric devices. Metal oxides have a history of over 50 years in their application as resistive gas sensors. The effect of a change in conductance on semiconductors was originally observed by Brattain and Bardeen in 1952 while studying the surface potential in different atmospheres [9]. The effect on MOX was studied by Seiyama and Kagawa [10], and the MOX gas sensor was patented by Taguchi in 1962 [11]. Commercial devices were first based on sintered pellets with painted contacts (Taguchi sensor), whereas today they are usually screen-printed on ceramic substrates. The disadvantages of conventional metal oxide sensors include the high power consumption in the range of 1 W, thus making battery operation impossible. Furthermore, they have limited selectivity and medium long term stability. In recent products, the power consumption is reduced by the reduction in size of the active part of the devices, such as the Figaro TGS 3870 [12].

Electrochemical cells (ECs) are standard sensors for CO detection. Their advantages include selectivity, the possibility of battery operation and relatively low cost. The sensor principle is based on a potential change by an oxidation or reduction reaction of the sensing electrode with the analyte gas. This leads to an ionic conduction in the liquid electrolyte that introduces an electric current in the external circuit. A sample product for an amperometric EC is the Figaro TGS 5042 [13]. This product has cross-sensitivity to hydrogen dioxide (H_2), but the sensor signal to CO is higher than that for H_2 for the same concentration

range. In many cases, ECs require filters and their lifetime is limited especially in high temperature environments.

In colorimetric gas sensors, a dye, in combination with a polymer, reacts when it comes into contact with the target gas, resulting in a color change [14]. Advantages include low cost, simple application, and no need for a battery. However, one great disadvantage is that there is no acoustic signal output. A sample product is the *sleep safe detector* from Arctic Electric for applications such as in camping [15]. A new concept combines the colorimetric principle with electronic signal output via optical detection based on light-emitting diodes [16].

1.3. Structure and Content of this Work

The present work evaluates several concepts of a miniaturized carbon monoxide sensor, thereby focussing on low-cost and mass-production possibilities. This includes both the choice and the fabrication method of a gas sensitive film, as well as the optimization of the whole sensor chip. In particular, large area pulsed laser deposition (PLD) is used and investigated for the deposition of MOX thin films. Special attention is given to tin dioxide (SnO_2) as the most popular MOX for sensing of reducing gases. Besides, alternative materials such as tungsten trioxide (WO_3) are studied for comparison.

Concerning the optimization of the whole chip fabrication process, the possibility of Pt structuring by a lift-off method is evaluated in detail. This method is applied to get smooth metal profiles that can provide good electrical contacts to the thin films. In the following, the power consumption of the silicon-based chip will be further optimized. Therefore, the possibilities of reducing the power consumption by making an appropriate choice of the sensor geometry are evaluated. This was done by comparing electrical measurements and simulations based on finite element method (FEM).

2. Fundamentals

2.1. Metal Oxides for Resistive Gas Sensing

2.1.1. Semiconducting MOX

Metal oxides (MOX) are used in a wide range of applications as some of them exhibit outstanding mechanical, electrical, dielectrical and chemical properties. The fields of application include abrasives (Al_2O_3), transparent electrodes for photovoltaics and organic light-emitting diodes[1] (doped In_2O_3), varistors (ZnO), high-k-dielectrics (Al_2O_3), and catalysts (CuO).

Most metals (non-noble) react with oxygen at reasonable temperatures to form oxides—or even at room temperature, in an electrochemical reaction. MOX generally exhibit an ionic crystal structure, indicating strongly localized electrons and ionic bonds. Many have a large band gap thus forming good insulators, such as Al_2O_3. Others present a Fermi level that can be influenced by dopants and thus show a semiconductor-like behavior. Examples of such oxides under investigation in resistive gas sensing are summarized in Table 2.1, e.g. the transition metal oxide ZnO and the post-transition metal oxide In_2O_3. As transition metal oxides are characterized by multi-valency (different oxidation states), they can form two or more different oxides. In contrast, non-transition metal oxides generally have only one preferred oxidation state, an exception being SnO_2 [18]. Physical properties of exemplary semiconducting MOX are summarized in Table 2.2. For materials with large band gaps, the intrinsic conductivity is negligible at room temperature and the transparency in the visible light range is high. However, when exposed to technical growth conditions, these MOX often conduct well, with carrier concentrations of 10^{15}–10^{19} cm^{-3} due to intrinsic defects. They exhibit an oxygen substoichiometry, so single or double ionized oxygen vacancies are often reported to act as donors in TiO_2, WO_3, ZnO, In_2O_3 and SnO_2. These oxides can be additionally n-doped and thus form stable transparent conducting oxides. Sn-doped In_2O_3 (indium tin oxide (ITO)) is the most popular example. Furthermore, the conductivity of ZnO and SnO_2 can also be greatly enhanced by doping with aluminum and

[1] As they show improved stability compared to 10–20 nm thick metal films with the same degree of transparency [17].

Table 2.1. Overview of semiconducting MOX.

Type	Example
transition metal oxides	TiO_2, WO_3, Cr_2O_3, Co_3O_4, NiO, CuO, ZnO
post-transition metal oxides	Ga_2O_3, In_2O_3, SnO_2

Table 2.2. Overview of physical properties of exemplary MOX [20].

MOX	Conduction type	Bandgap	Crystal structure
SnO_2	n	3.6 eV	Rutile
ZnO	n	3.4 eV	Wurzite
In_2O_3	n	3.0 eV	Bixbyite
WO_3	n	3.0 eV	Monoclinic
CuO	p	1.4 eV	Monoclinic
Co_3O_4	p	1.9 eV	Spinel

antimony, respectively. P-conduction in MOX is also possible due to intrinsic defects, prominent examples being Co_3O_4 and CuO (see Table 2.2), which exhibit a metal-substoichiometry [19].

2.1.2. Material properties of the metal oxide SnO_2

Tin dioxide is certainly the most widely investigated and most widely used metal oxide in commercial gas sensors [21]. Besides, it is also of interest as a transparent conducting oxide for applications such as displays and photovoltaics. There are two different oxides of tin, namely tin monoxide (SnO, tin-(II)-oxide) and tin dioxide (SnO_2, tin-(IV)-oxide), the monoxide being metastable and transforming into tin dioxide and tin at more than 300 °C. This shows the dual-valency of Sn, where both Sn^{2+} and Sn^{4+} are stable ions. The compound tin sesquioxide (Sn_2O_3, tin-(II,IV)-oxide) is very rarely formed. SnO_2 is naturally found to crystallize in a tetragonal body-centered structure known as *rutile*, named after the mineral of TiO_2. The tin atom (cation) is surrounded by six oxygen atoms (anions) that are located at the corners of an octahedron [17]. A schematics of the unity cell is shown in Figure 2.1.

In experiments, SnO_2 is found to have a deviation in stoichiometry with a higher tin content. It is widely acknowledged and supported by spectroscopic studies that this is due to the formation of oxygen vacancies and not to the formation of tin interstitials [23, 24]. The double-ionized oxygen vacancies $V_O^{\bullet\bullet}$ are usually assumed to induce the characteristic n-conduction in non-ideal SnO_2 [18, 25], as described by the following equations:

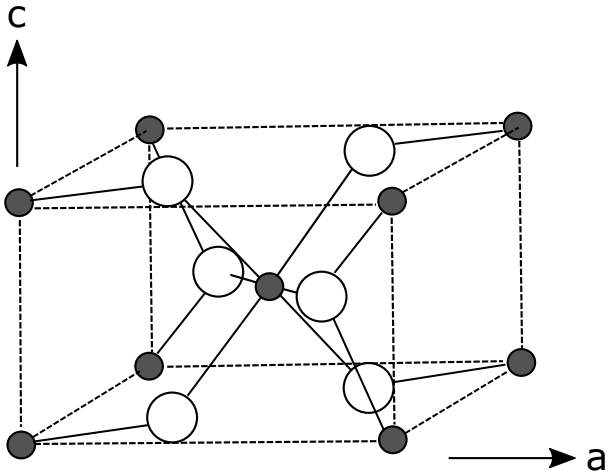

Figure 2.1. Schematics of the unity cell of rutile SnO_2. Oxygen atoms in white and tin atoms in grey, after [22].

$$SnO_2 \rightleftharpoons {Sn_{Sn}}^{4+} + {O_O}^{2-} + V_O + \frac{1}{2}O_2. \tag{2.1}$$

$$V_O \rightleftharpoons V_O^{\bullet\bullet} + 2e^-. \tag{2.2}$$

Sn_{Sn} corresponds to the tin atom at a tin lattice place and O_O to an oxygen atom at an oxygen lattice place. Lower quantities of Sn interstitials can also partly compensate for these defects [18]. However, the electronic structure of SnO_2 is still a matter of debate, because the dominant defects are still not well modeled by density functional theory (DFT) studies. Some authors assume that H impurities (interstitial and Sn substitutes) lead to the n-conduction [26]. There is no experimental evidence for the presence of such defects in SnO_2, though. Lany and Zunger explained the discrepancy between the deep level of $V_O^{\bullet\bullet}$ under equilibrium conditions found by DFT calculations and the experimentally high donor concentrations by metastable oxygen vacancy states due to persistent photoconductivity [27]. In experiments, the donor levels are found to be shallow with 30 meV for single and 150 meV for double ionization [28]. The (110) coordinate surface is often taken as a model surface of SnO_2. It contains surface-bridging oxygen atoms (cf. Figure 2.2) arranged in rows in <110> direction that can be removed (reduced) to form a stable, compact surface, e.g. by heating up in UHV or sputtering [18, 23, 29, 30]. Bridging oxygen can be

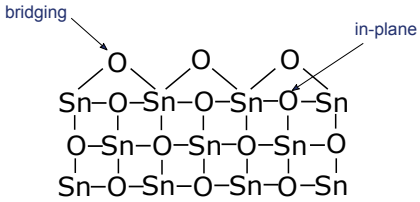

Figure 2.2. SnO_2 (110) surface indicating surface and bridging oxygen atoms.

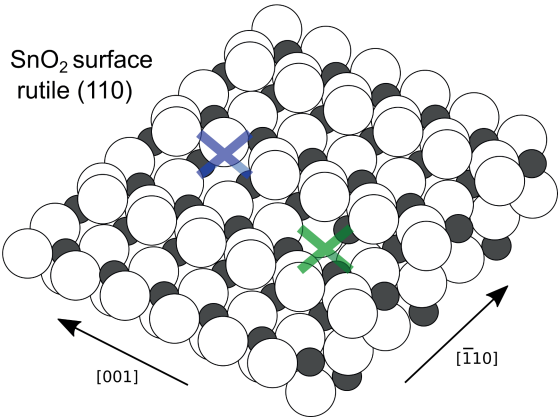

Figure 2.3. Schematics of the SnO_2 (110) rutile surface, oxygen atoms in white and tin atoms in grey. Two oxygen defects marked with crosses (surface (blue) and bulk (green)) are included, after [18].

removed from the (110) surface [18, 30] without providing donors, in contrast to the in-plane oxygen [29] and bulk oxygen defects, see Figure 2.3.

2.1.3. Material properties of the metal oxide WO_3

After SnO_2, WO_3 is the most widely used metal oxide in commercial applications. Tungsten-(VI)-oxide WO_3 is a stable oxide of tungsten under normal conditions. Like SnO_2, WO_3 is also n-conducting due to intrinsic defects. Its crystal structure is triclinic (δ-phase) below 17 °C, monoclinic (γ-phase) between 17 °C and 320 °C, and changes to orthorhombic (β-phase) at higher temperatures up to 720 °C [31]. Consequently, there might by a phase change of the material in the application relevant temperature range for gas sensing of $200 - 400\,°C$.

2.1.4. Electrical properties of semiconducting MOX

Undoped tin oxide features a high, direct band gap of 3.5 eV and carrier concentrations of up to $10^{20}\,\mathrm{cm}^{-3}$ leading to resistivities in the range of 10^{-2}–10^{-4} Ohmcm [17, 28]—it is one of the most investigated materials for transparent semiconductors. The electrical properties of thin film SnO_2 are influenced by growth parameters such as substrate temperature, film thickness, and annealing [17]. Higher growth temperature is known to effect grain-boundary scattering, and the grain size increase leads to higher mobility [17]. Increased grain size can also lead to higher carrier concentration, as the conduction in polycrystalline tin oxide films is mainly limited by the space charge regions due to band bending on the surface of the grains. A model of the potential barrier-based conduction was reported by Petritz [32]. This effect is primarily valid for non-degenerated semiconductors, e.g. SnO_2 with carrier concentrations below $10^{19}\,\mathrm{cm}^{-3}$ [17]. It also represents the important conduction mechanism in the operation mode of gas sensors, which is discussed in Section 2.1.6. SnO_2 can be n-doped by the addition of group-V elements, the most efficient dopants being Sb and F. P-doping of n-MOX is generally difficult, as newly created energy levels close to the valance band tend to be intrinsically compensated for. Hence, this then makes co-doping necessary [33].

2.1.5. Adsorption of gases on MOX

There is a great variety of adsorption processes, each characterized by its typical strength of interaction. Weak and strong interaction of the gas (or adsorbate) on the solid state surface (or adsorbent) are known as physisorption and chemisorption processes. If the chemisorption process includes a direct electron transfer, it is called an ionosorption process. Physisorption is characterized by Van der Waals forces. All gases, even chemically inert noble gases, can be physisorbed on surfaces. Physisorption is completely reversible and practically no energy input is needed for desorption. The Van der Waals binding energies are typically below 25 kJ/mol [34]. Chemisorption/ionosorption is characterized by stronger (chemical) binding energies of at least about 50 kJ/mol [35]. The reversal of adsorption requires an energy input, e.g. by heating or exposure to radiation in the optical regime. Adsorbed atoms can also penetrate into the solid or adsorbed molecules can dissociate and penetrate into the solid (absorption) [19]. Chemical bonds can form, to begin with, if the activation barrier is overcome. When this happens, e.g. through dissociation of a molecule, the system can reach a state of minimized energy. To dissociate a molecule on the surface of an ionic crystal, the attracting force has to be large enough to both attract the

positive and the negative ion [19]. A typical application of dissociative adsorption is heterogeneous catalysis. For ionosorption of a molecule on a surface (e.g. O_2^-), the electron of the ionic binding is not available to the adsorption process, which is why a nearly free electron resulting from an oxygen dislocation in the crystal is required. However, the distance between the surface acceptor and the bulk dislocation can be quite large (range 100 nm) [19]. In chemical reaction processes, a minimum of Gibbs free energy G, is reached by minimizing the potential energy and maximizing entropy:

$$\Delta G = \Delta H - T\Delta S \tag{2.3}$$

where H is the enthalpy, T the temperature, and S the entropy [35]. For $\Delta G < 0$ the reaction can occur spontaneously.

The different activation energies of physisorption and chemisorption are represented in the temperature dependence of these processes. While physisorption already takes place at and below room temperature, the maximum of chemisorption of oxygen on MOX is typically above 100 °C, see Figure 2.4 for the example of ZnO [36]. The adsorption of gases on surfaces is limited by several factors. First of all, the number of the most attractive adsorption places is limited. These places are surface irregularities such as dislocations with dangling bonds. During the adsorption process, gas species also adsorb on less attractive surface sites. The second limit is of electric nature. The adsorption leads to a non negligible surface charge (electronic double layer) which limits further adsorption accordingly [19]. Third, if the surface is covered by a complete monolayer, the adsorption may also be reduced because of changing surface properties. In experiments, the dynamic adsorption process of chemisorption is often found to be describable by a logarithmic time evolution. However, a theoretical description is not as straightforward, but the decreasing energy release with an increase in adsorption leads to a similar behavior to that of the Langmuir isotherm, where adsorption is limited by the number of adsorption sites [19].

2.1.6. Semiconducting view of surface adsorption

In the usual operation range of MOX gas sensors between 200 °C and 400 °C, the literature describes the conduction as primarily electric with ionic conduction being negligible. For a compact semiconductor surface, the model for electronic interaction in the case of surface ionosorption is fairly simple. If we take the case of acceptor-type surface species such as oxygen adsorbed on the surface of an n-type semiconductor, see Figure 2.5, this leads to a surface band bending

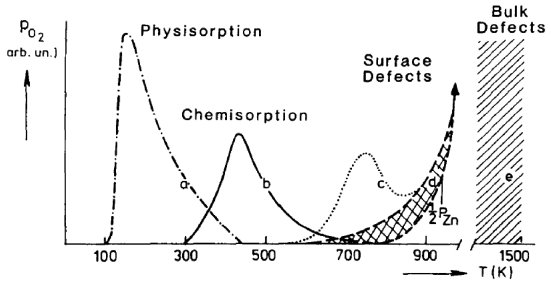

Figure 2.4. Temperature-dependent adsorption and desorption processes, example of oxygen adsorption on a ZnO $(10\bar{1}0)$ surface. The results are based on the investigation of the temperature-dependent pressure of thermally desorbed oxygen: (a) Adsorption at 100 K, (b) adsorption at 300 K, (c) desorption at high temperatures for samples measured directly after preparation, hatched part for repeated adsorption cycles. (d) Temperature range where monocrystalline ZnO is manufactured and bulk defects are produced [35, 36].

of qV_S (q elementary charge, V_S surface potential) and the creation of a surface depletion layer of the characteristic depth z_0.

The surface depletion layer can be expressed by the Poisson equation:

$$\nabla^2 V = -\frac{\rho}{\epsilon_0 \epsilon_r}. \tag{2.4}$$

We assume that the charge ρ of the depletion layer is built up by the donor impurities N_D in the bulk and is constant over the whole depletion layer (Schottky-approximation), with ϵ_0 and ϵ_r being the vacuum and relative permittivity, respectively. Consequently, the case of a surface inversion zone is not regarded here. If we additionally expect a potential change only in z-direction of the semiconductor, we get the following relation:

$$\frac{\mathrm{d}^2 V}{\mathrm{d}z^2} = -\frac{qN_D}{\epsilon_0 \epsilon_r}. \tag{2.5}$$

The following boundary conditions apply:

1. The potential is constant below the space charge region $z = z_0$:

$$\left.\frac{\mathrm{d}V}{\mathrm{d}z}\right|_{z=z_0} = 0. \tag{2.6}$$

2. The potential is set to zero on the surface $z = 0$:

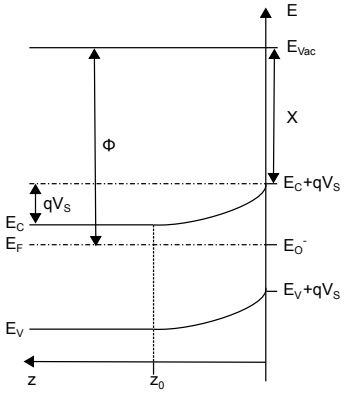

Figure 2.5. Band bending qV_S due to the surface interaction on an n-type MOX and ionosorbed oxygen species at level E_0 in the band gap between the valance band E_V and the conduction band E_C. E_{Vac} is the vacuum level, E_F the Fermi level, Φ the work function and X the electron affinity. Surface dipoles that might cause a change in electron affinity are not included in this schematics.

$$V\big|_{z=0} = 0. \tag{2.7}$$

The differential equation can be solved by integration:

$$V(z) = z(2z_0 - z)\frac{qN_D}{2\epsilon_0\epsilon_r}. \tag{2.8}$$

This results in the Schottky-relation:

$$V_S = V(z = z_0) = z_0^2 \cdot \frac{qN_D}{2\epsilon_0\epsilon_r}. \tag{2.9}$$

The depth of the depletion layer z_0 is given by:

$$z_0 = \sqrt{\frac{2\epsilon_r\epsilon_0 V_S}{qN_D}}. \tag{2.10}$$

Consequently, the surface adsorption is limited by the surface band bending, which is known as the Weisz limit [37]. The surface Fermi level drops until it reaches the level of the surface adsorbates. This increases the energy for further adsorbate molecules, and hence the Fermi level is *pinned*. At this point we do not know how large the energetic surface band bending (qV_S) is, so we cannot calculate z_0. With respect to the Weisz limit, we can estimate the energy for bulk electrons reaching the surface to be $qV_S \leq 1\,\text{eV}$ [20], and consequently,

we can estimate the maximum surface depletion for a known bulk donor concentration N_D. It is typically in the range of 10–100 nm [38]. Very reactive oxidizing agents are expected to create surface states closer to the valance band than oxygen, thus increasing the width of the surface depletion layer. The Weisz limit sets an electronic limit to surface ionosorption, so that species like oxygen can only be chemisorbed—if dominated by a depletion layer—up to 10^{-3} of a monolayer.

The Debye length λ_D is an important characteristic length of doped semiconductors. It depends on the temperature T and on the doping level:

$$\lambda_\mathrm{D} = \sqrt{\frac{\epsilon_r \epsilon_0 k_\mathrm{B} T}{q^2 N_\mathrm{D}}}. \tag{2.11}$$

z_0 can thus be expressed as a function of the Debye length, k_B being the Boltzmann constant [38]:

$$z_0 = \lambda_\mathrm{D} \sqrt{2 \frac{qV_\mathrm{S}}{k_\mathrm{B} T}}. \tag{2.12}$$

If qV_S is in the same order of magnitude as $k_\mathrm{B}T$, λ_D is also in the same order of magnitude as z_0. We can conclude that the surface depletion is dependent, on the one hand, on chemical adsorption expressed by qV_S, and on intrinsic material properties such as the doping level as (expressed by λ_D [39]) on the other hand.

2.1.7. Ionosorption model for the interaction with reducing gases

In the last decades, the scientific community was able to identify the signal-building-mechanism in n-conducting MOX to reducing gases through interaction with pre-adsorbed oxygen species [19, 20, 40]. This model is supported by experiments that do not show a high change in the resistance of SnO_2 if it is exposed to the reducing gas CO in in a vacuum ambient [41]. Oxygen is known to be adsorbed in the molecular form as $O_2{}^-$ in the lower temperature range, while at higher temperatures (above 150 °C), it is adsorbed in the atomic form single and double ionized (O^- and O^{2-}) [42]. In this application-relevant temperature range, only atomic adsorption has to be considered. O^- has been seen to be a lot more reactive than $O_2{}^-$. Changes in O^--signal in the electron spin resonances spectra can be seen with the exposure to CO, H_2 and CH_4 [43].

The adsorption process can be expressed by the following equation:

$$\frac{1}{2}\mathrm{O_2(gas)} + \alpha \cdot \mathrm{e^-} + S_\mathrm{s} \rightleftharpoons \mathrm{O^{-\alpha}(ads)}, \tag{2.13}$$

where O_2(gas) represents an oxygen molecule in the gaseous phase and $O^{-\alpha}$(ads) an adsorbed oxygen species on the surface site S_s, with α=1, for single-ionized, and $\alpha = 2$ for double-ionized oxygen. Using the law of mass action, we then get the following chemical rate equation [42]:

$$k_{\text{ads}} \cdot [S_s] \cdot n_s^{\alpha} \cdot p_{O_2}^{1/2} = k_{\text{des}} \cdot [O^{-\alpha}(\text{ads})], \tag{2.14}$$

where k_{ads} and k_{des} are constants of chemical ad- and desorption that depend on their activation energies and n_S is the concentration of surface electrons. The surface coverage θ is defined as follows:

$$\theta = \frac{[O^{-\alpha}(\text{ads})]}{[S_t]}, \tag{2.15}$$

where $[S_t]$ is the maximum available number of surface sizes, which is equal to the sum of the occupied surface sites and the remaining free surface sites:

$$[S_s] + [O^{\alpha-}(\text{ads})] = [S_t]. \tag{2.16}$$

Thus, we get the following relation:

$$(1 - \theta) \cdot k_{\text{ads}} \cdot n_s^{\alpha} \cdot p_{O_2}^{1/2} = k_{\text{des}} \cdot \theta. \tag{2.17}$$

This equation shows a relation between the concentration of ionosorbed oxygen species and the concentrations of electrons that can reach the surface. We can now build up a relation between surface ionosorption and the Debye length by using the results from the consideration in Section 2.1.6. Here, small and large grains can be distinguished: For large grains, the grain diameter is larger than λ_D so the bulk is unaffected. For small grains, the crystallite size is comparable to λ_D .

Large grains: For large grains we consider overall electroneutrality, and thus the surface charge is equal to the space charge:

$$\alpha \cdot \theta \cdot [S_t] = N_D \cdot z_0. \tag{2.18}$$

If we assume that the electrons in the surface region are Boltzmann-distributed (the Fermi level being far from the band edges) [20], we obtain the following relation between donors and the concentration of surface electrons n_s:

$$n_s = N_D \exp\left(-\frac{qV_S}{k_B T}\right). \tag{2.19}$$

This, along with the Schottky-relation (Equation 2.9), leads to the following relation between surface coverage, the oxygen partial pressure p_{O_2}, and n_s:

$$\theta = \sqrt{\frac{2 \cdot \epsilon \cdot \epsilon_0 \cdot N_D \cdot k_B \cdot T}{\alpha^2 \cdot [S_t]^2 \cdot q^2} \cdot \ln \frac{N_D}{n_s}}. \tag{2.20}$$

Small grains: Two assumptions are made: First, small cylindrical grains with a radius r_{grain} which is much smaller than their length so the Poisson equation is favorably expressed in cylindrical coordinates. Second, flat band case, so the energy difference between the center and surface of the grains is in the range of the thermal energy $k_B T$. The following equation for the surface coverage can be obtained (details can be found in [42, 44]):

$$\theta = \frac{N_D \cdot r_{grain}}{2 \cdot \alpha \cdot [S_t]} \cdot \left(1 - \frac{n_s}{N_D}\right). \tag{2.21}$$

This flat band case can be assumed for SnO_2 grains below a diameter of 50 nm, according to experimental values [42, 44].

The reducing gas CO is expected to react with pre-adsorbed or lattice oxygen [18] with release of CO_2. If we assume a reaction with ionosorbed oxygen the reaction is expressed by adjusting Equation 2.13:

$$CO(gas) + O^{-\alpha}(ads) \rightleftharpoons CO_2(gas) + \alpha \cdot e^- + S_s. \tag{2.22}$$

The following rate equation is obtained [42]:

$$k_{ads} \cdot (1 - \theta) \cdot n_s^{\alpha} \cdot p_{O_2}^{1/2} = (k_{des} + k_{react} \cdot p_{CO}) \cdot \theta. \tag{2.23}$$

Barsan and Weimar [42] found that this leads to the following relation for the surface carrier density of large grains:

$$n_s \propto p_{CO}^{\frac{1}{\alpha+\delta}}, \tag{2.24}$$

and for small grains:

$$n_s \propto p_{CO}^{\frac{1}{\alpha+1}}, \tag{2.25}$$

where δ results from an approximation and has typically positive values smaller than 0.2 [42]. These relations show a power-law dependence and are important for the signal-forming mechanism in porous MOX. Here, grain boundaries play a significant role and the conductance is mostly controlled by the depleted regions with the electron concentration n_s, see Section 2.1.4. Considering the grain shape, correction factors can be introduced [45].

Hydrogen is expected to show a similar reaction route as carbon monoxide, interacting with pre-adsorbed oxygen species under formation of H_2O [46]. For other reducing gases like hydrocarbons, the simplest representative being CH_4, the reaction mechanism might differ; an overview can be found in e.g. [18, 47, 48]. Methane is supposed to dissociate under formation of a methyl group (CH_3) and hydrogen. This methyl group may take part in further reactions. Dissociated hydrogen was assumed to build surface acceptors in the moderate temperature range of less than 150 °C and to react with lattice oxygen at higher temperatures [47]. For propylene, a dissociative reaction under formation of a hydrogen atom and an allyl radical was proposed [34] . Both can then take part in further reactions with oxygen atoms or ions, for example. Ammonia, which is a Lewis base, is expected to not get dissociated on the SnO_2 surface [49]. It was found to form a weak hydrogen bond to an oxygen atom on the SnO_2 surface and to interact with surface OH-groups [47].

Other cases that are not regarded in detail here:

- **P-type MOX:** For p-type MOX, a similar model can be established, see [46, 50]. Since an accumulation layer builds up under the oxygen background, the sensor signal is less dominated by inter-granular barriers. This leads to a less-elevated concentration-dependent sensor signal that is approximately the square root of the sensor signal of an n-type MOX [46, 51].

- **Depletion transfer to accumulation layer**: Exposure to a very strong reducing agent on an n-type MOX or very strong oxidizing agent on a p-type MOX can lead to formation of an accumulation layer (n-type) or a depletion layer (p-type) on the surface [20]. Recent studies show that this can occur under realistic operation conditions for CO-sensing in humid air [52].

- **Inversion: switch between n-type and p-type**: It is possible that a material changes its dominating conduction mechanism from n- to p-type through an extended depletion layer on the surface [20]. If the band bending becomes large enough, e.g. due to interaction with high oxygen concentrations, the hole conduction can be dominant on the surface. Switch from n- to p-type was, for example, detected for α-Fe_2O_3 [53]. This can lead to an inversion of the sensing behavior, hence a decrease in conduction when interacting with reducing gases. A switch from p-type to n-type by an extended accumulation layer is also possible.

2.1.8. Oxidation-reduction model for the interaction with reducing gases

In the last years a discussion of the validation of the former model started as Barsan *et al.* published results of measurements in an atmosphere of reduced oxygen content [51, 54]. Surprisingly, it was discovered that there was a response of pure SnO_2 to reducing gases even in pure nitrogen ambient and it was even higher than the one found under ambient conditions. For this reason, the oxidation-reduction model or oxygen vacancy model [55]—which was already proposed in early gas sensor models—has gained popularity again and was introduced in density-functional-theory (DFT) calculations [56]. A mechanism of adsorption of CO is suggested, where CO reduces the surface creating an oxygen vacancy and freeing CO_2, followed by a reduction of SnO_2.

This can be expressed by the following quasi-chemical equations:

$$\mathrm{O(l)} + \mathrm{CO(ads)} \rightarrow \mathrm{CO_2(ads)} + \mathrm{V_O}, \tag{2.26}$$

$$\mathrm{O_2(gas)} + \mathrm{V_O} \rightarrow \mathrm{O_2(ads)}, \tag{2.27}$$

$$\mathrm{CO(ads)} + \mathrm{O_2(ads)} \rightarrow \mathrm{CO_2(ads)} + \mathrm{O(l)}. \tag{2.28}$$

Here, O(l) represents a lattice oxygen atom at a surface-bridging place. In this reaction, one oxygen vacancy is created per adsorbed CO molecule and SnO_2 is reduced, transferring a charge of approx. 1 e [56, 57]. This mechanism is known as Mars-van Krevelen mechanism [49, 55, 57]. In a following reaction, the oxygen vacancy is consumed by an adsorbed oxygen species (Equation 2.27). All other involved reactions take place without significant charge transfer. Adsorbed CO can also react with this adsorbed oxygen ion and form CO_2 and a lattice oxygen atom (Equation 2.28). In a pure nitrogen background, these last steps of reoxidation are limited, resulting in a higher response [57].

This model has been partly supported by dispersive infrared spectroscopy studies [57]. However, there remains a certain gap between calculation and experimental electrical characterization. On the one hand, the assumption of a charge transfer to a stoichiometric tin dioxide material is only partly realistic as it is widely accepted that n-type MOX exhibit semiconducting behavior due to oxygen non-stoichiometry. This is considered in the more recent DFT study of the SnO_2 (110) surface by Wang *et al.* [58]. Here, realistic reaction paths of CO with pre-adsorbed oxygen on an oxygen-deficient surface in high oxygen background were found. It was further found that a direct reduction of SnO_2 can take place in a low-oxygen environment. On the other hand, it is still unclear to what extent the CO signal is determined by direct reduction and by interaction with

pre-adsorbed oxygen species in real operation conditions. To date, no existing signal-building model includes the direct reduction process.

No CO_2 was measured in the case of the exposure of tin oxide to CO in N_2 [51, 59]—most likely due to a very limited surface reduction [57, 58]. However, in the case of WO_3 CO_2 was measured even in the absence of oxygen [60]. As a result, the surface reaction of CO is assumed to differ in the case of WO_3 compared to SnO_2.

2.1.9. Interaction with water

Water is always present under realistic sensing conditions. Its concentration in the ambient can change in a wide range, depending on both relative humidity and temperature. For instance, the concentration can be especially high on a hot and humid summer day and low on a cold winter day. It is only adsorbed in the molecular form below 200 °C, whereas OH is still present at higher temperatures above 400 °C [29]. In experiments, water was found to act as a reducing gas with n-conducting MOX such as SnO_2, and thus reducing its resistivity by forming donors. However, it is still not clear, which reaction principle is valid. Some principles already introduced in the 1980s and 1990s are presented here [42]:

First mechanism: Presented by Heiland and Kohl [61]:

$$H_2O(\text{gas}) + Sn_{Sn} + O_O \rightarrow (Sn_{Sn}{}^{+} - OH^{-}) + (OH)_O^{+} + e^{-}. \qquad (2.29)$$

In this case, the H_2O molecule is dissociated into two radicals OH and H. OH reacts with a surface tin atom Sn_{Sn} and creates an isolated OH-group. The neutral H atom reacts with a lattice oxygen atom, forming a *rooted* OH-group [42]. The OH-group has a lower electron affinity than the oxygen atom and is ionized. An electron is injected into the conduction band.

Second mechanism: Presented by Heiland and Kohl [61]:

$$H_2O(\text{gas}) + 2\,Sn_{Sn} + O_O \rightarrow 2\,(Sn_{Sn}{}^{+} - OH^{-}) + V_O{}^{\bullet\bullet} + 2\,e^{-}. \qquad (2.30)$$

In this reaction, no rooted OH-groups are formed. However, oxygen vacancies $V_O{}^{\bullet\bullet}$ are formed, as one lattice oxygen atom reacts with hydrogen to form a surface OH-group bound to a Sn atom. Isolated and rooted hydroxyl

groups can be differentiated by spectroscopic techniques such as diffusive infrared spectroscopy [57]. If water adsorption is assumed to take place mainly due to the second mechanism, the change of surface states and charge transfer can be considered in the ionosorption model of Barsan and Weimar [42]. If we assume oxygen vacancies as preferred adsorption sites of oxygen, this mechanism would enhance the CO sensing with the presence of humidity. This is usually not seen experimentally for pure (non-doped) SnO_2.

Third mechanism: Presented by Henrich, Cox and Morrison [18, 20]:

$$Sn^+ + H_2O(gas) \rightarrow (Sn : OH) + H_S{}^+. \tag{2.31}$$

In this case, the water molecule reacts with a surface Lewis site Sn^+ that is represented by a cation on the surface. The remaining proton stays adsorbed and can take part in further chemical reactions as a Bronsted acid site. This is a more indirect effect of an interaction of the hydrogen atom and the hydroxyl group interacting with an acid or basic group on the surface. There might also be an interaction with surface species already adsorbed, so pre-adsorbed oxygen could be displaced by water adsorption [62, 63].

At more than $100\,^\circ C$, hydroxyl groups form in interaction with pre-adsorbed oxygen:

$$H_2O(gas) + O_O{}^-(ads) \rightarrow (OH)_S^- + (OH)_O^- + e^-. \tag{2.32}$$

Consequently, CO and water compete for pre-adsorbed oxygen species, leading to a reduction in the CO signal in humid background.

2.1.10. Interaction with oxidizing gases

From an empirical point of view, oxidizing gases have the effect of an increasing resistance of n-type metal oxides. One of the most prominent examples is the oxidizing gas NO_2, which is present in ambient air due to pollution through combustion processes. The interaction is effectively a chemisorption on the MOX (e.g. adsorbed as $NO_2{}^-$ [36, 64, 65]), which is taking place already at temperatures below $200\,^\circ C$ on SnO_2. This is described by the following equation:

$$NO_2(gas) + e^- \rightarrow NO_2{}^-. \tag{2.33}$$

This reaction might not be reversed; instead, gaseous NO is produced in a further reaction step [65]:

$$NO_2{}^- \rightarrow NO(gas) + O^-. \tag{2.34}$$

Several mechanisms were suggested:

1. Adsorption on oxygen vacancies leading to a recombination [36].
2. Creation of additional surface states that are closer to the conduction band than the states of pre-adsorbed oxygen ions [64, 65].

In addition, an interaction of NO_2 with pre-adsorbed oxygen species is possible [66]:

$$NO_2(gas) + O^- \rightarrow NO_2{}^+ + 2\,O^-, \tag{2.35}$$

$$NO_2(gas) + O_2{}^- + 2\,e^- \rightarrow NO_2{}^- + 2\,O^-. \tag{2.36}$$

Leblanc *et al.* [67] investigated the surface species forming by NO_2 exposure to SnO_2. Different nitrato groups ($NO_3{}^-$) were found by infrared spectroscopy for dry (dehydroxylated) samples in different temperature regimes. In the low temperature range between room temperature and 100 °C, the unidendate groups dominate. These are converted into bidentate complexes in the temperature range of 100–300 °C. For even higher temperature the bridging bidentate groups remain, as they are the most stable surface species. They decompose at 500 °C. For wet (hydroxylated) surface, additional hydrogeno nitrate complexes are formed. The adsorption process of NO_2 is thus strongly dependent on the surface properties and temperature. Adsorption already takes place at temperatures below 100 °C, and consequently, sensor response is already measured at low temperatures. However, the sensor recovery time is very long in this temperature regime as the desorption process is slow. As a result, the ideal temperature range for NO_2 sensing is in the medium range of 50–300 °C [65, 67].

2.1.11. The concentration-dependent sensor signal

Modeling the absolute resistance of a MOX gas sensor is quite challenging, as it represents a complex, potentially porous solid with a high number of interfaces being not experimentally accessible. Figure 2.6 illustrates the difference between compact and porous layers. Curves illustrate band bending in the direction of the current flow for porous layers and orthogonally on the surface for compact films. This can be viewed in a simplified picture as a high resistance either in series or in parallel to the low resistance of the bulk. The degree of porosity can be estimated by nitrogen physisorption and the granularity by methods

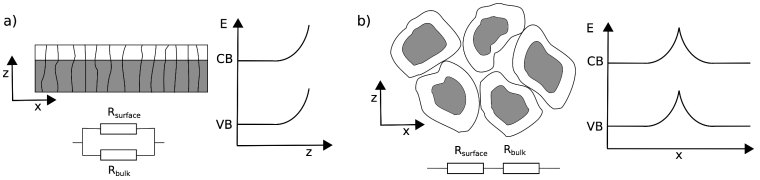

Figure 2.6. Simplified schema of compact (a) and porous (b) n-type metal oxide films. The highly resistive depletion layer is illustrated in white. For the sake of simplicity the contacts are not included. For details, see text.

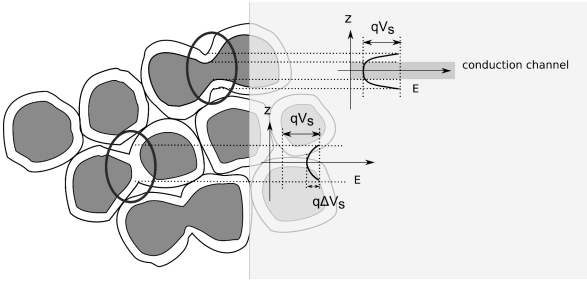

Figure 2.7. Schema of electric contacts at necks between grains, after [42]. Upper example illustrates a conducting grain-grain-boundary, lower example a completely depleted neck.

such as scanning electron microscopy (SEM), transmission electron microscopy (TEM), atomic force microscopy (AFM), or X-ray diffraction (XRD). All these methods are rather complex so that the electric interface cannot be characterized easily. Grain-grain boundaries can be either of gas-accessible (isolating) or of conducting (neck) nature, as illustrated in Figure 2.7. The possibility of completely depleted (isolating) necks is therein also illustrated. These effects may be investigated by percolation theory. The maximum surface depletion mostly depends on the donor concentration and can be estimated as shown at the end of Section 2.1.6. Based on this calculation, we can estimate the maximum total change in a compact layer of an n-type MOX with the depletion layer only at the surface and a thickness much higher than the Debye length, where the conduction is assumed to take place only in the non-depleted region.

For a porous layer with multiple gas-accessible grain-grain boundaries, the conduction is mainly dominated by the grain boundaries. A power-law dependence of the gas signal as a function of concentration can be derived from n_s. A similar case is that of a very thin MOX film completely depleted of electrons. Different exponents are found for different conditions, e.g. for porous layers

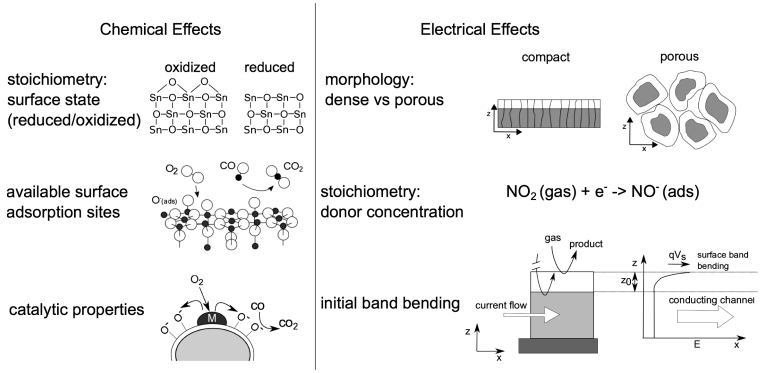

Figure 2.8. Overview of chemical and electrical influences on the gas sensor signal [42, 68, 69].

with not completely depleted grains the conductance $1/R$ is $1/R \propto p_{\mathrm{CO}}^{\gamma_1/(\alpha+\delta)}$, with γ_1 being a value in the range 0.8 to 1.2. Detailed results can be found in [42].

To date, there is still no complete model of the detection mechanism. This is due to the simple measurement principle based on a resistance change on the one hand and the complex signal building mechanism on the other. The function of the gas sensor is influenced by chemical properties (adsorption) of the material and electrical properties that lead to a resistance change (transduction). Moreover, these are no isolated properties, as the Weisz limit (Equation 2.10) expresses a link between adsorption and surface depletion. These properties are illustrated in Figure 2.8. They cannot be distinguished by a simple *black-box* measurement of the resistance change under the gas atmosphere of the sensor. However, there are numerous characterization techniques that can be applied to get further insight into the mechanisms behind the signal. These are summarized in Table 2.3.

The normalized sensor signal S_{red} for n-type MOX is defined as the relative resistance change, when exposed to a reducing gas such as CO:

$$S_{\mathrm{red}} = (R_0 - R_{\mathrm{gas}})/R_{\mathrm{gas}}, \tag{2.37}$$

where R_0 is the initial resistance prior to gas exposure and R_{gas} is the resistance under gas exposure. For the case of oxidizing gases, where the resistance is increased under gas exposure, the following definition is taken:

$$S_{\mathrm{oxid}} = (R_{\mathrm{gas}} - R_0)/R_0. \tag{2.38}$$

Table 2.3. Examples of characterization methods for the investigation of electrical and chemical properties of gas sensors, XPS stands for X-ray photoelectron spectroscopy.

Chemical Effects	Analytical Methods
stoichiometry: surface state (reduced/oxidized)	- XPS
available surface adsorption sites	-XRD - humidity cross-sensitivity
catalytical properties	-catalytic conversion
Electrical Effects	Analytical Methods
morphology: dense vs porous	- SEM, TEM, AFM - N_2 physisorption
stoichiometry: donor concentration	-Hall effect measurement -charge carrier relaxation
initial band bending	-Kelvin probe

These different definitions ensure a positive sensor signal and possible values larger than one in both cases.

2.2. Noble Metal Additives and Heterojunctions

Noble metal additives such as gold (Au), silver (Ag), palladium (Pd), and platinum (Pt) were found to enhance the properties of semiconducting MOX like response and recovery time, sensor signal and stability [39, 70]. Furthermore, they are proved to minimize cross-sensitivity, especially to humidity. They also show catalytic activity to gases; however, the interaction in the sensor is complex and can be of diverse nature, as a plain catalytic effect alone would not enhance the gas-sensing properties. In addition, the additives may also influence the morphology of the material [71]. Two mechanisms are reported to take place in the application of noble metal additives to semiconducting MOX sensors, also illustrated in Figure 2.9 [39, 70]:

1. **The spill-over effect** is a chemical effect that is based on the catalytic activity of the metal additives. The gas reacts with a noble metal cluster on the surface through reduction in its energy barrier. This yields a dissociation of the gas molecules, and the more reactive radicals react with the surface of the MOX: they are *spilled* over the surface.

2. **Fermi-level control** is an electronic effect, that is based on the higher work function of noble metal oxides (e.g. palladium oxide (PdO)) that

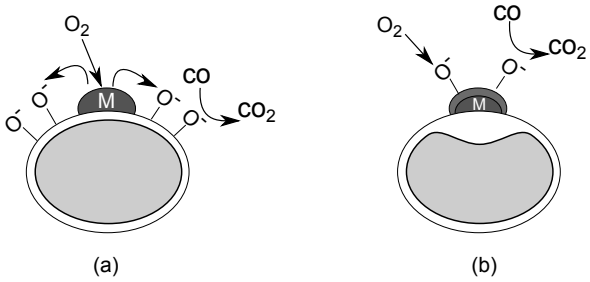

Figure 2.9. Illustration of sensitization interaction of noble metal additives in the surface reaction with gases. (a) Spill-over and (b) Fermi-level control [68].

are formed by interaction with the gases. This increases the extent of the depletion zone.

The addition of noble metals is often referred to as *doping*, although the distribution might not be on an atomic level. It is widely accepted in the literature that, in the case of Pd doping, a Fermi-level control takes place, as Pd is easily oxidized and forms PdO in the same manner as for Ag [39, 70]. The electronic interaction leads to a rise in resistance when metal sensitizers are added [34]. However, a change in the Fermi level measured through Kelvin probe, is a more suitable indicator than a pure resistance measurement [72]. The spill-over mechanism is reported to be dominant for Au-doped films [39, 70], especially in the interaction with hydrogen, but possibly also with CO and oxygen [34, 72]. For Pt-doped films, both Fermi-level control and spill-over are reported [70, 73].

In all cases, the dispersion of the metal additive in the MOX plays a significant role. For a spill-over, small particles are ideal, so that the dissociated species can directly react with the surface of the metal clusters. For gold addition, it was seen that clusters are occurring at low concentrations and spectroscopic studies under sensor operation conditions (operando studies) support the hypothesis of oxygen spill-over in this case [72]. In the case of the Fermi-level control, a wide dispersion on the surface or even an atomic dispersion in the lattice is beneficial to the sensing properties [73]. Here it is still a matter of debate, if the electronic sensitization of atomically distributed metals is the same as Fermi-level control [68]. However, through conventional spectroscopic techniques, small clusters and distributions on an atomic level can hardly be distinguished, e.g. with XPS. Thus, advanced techniques such as X-ray absorption spectroscopy have to be applied [72, 74]. In the case of conventional thick film sensors, usually impregnation of the powder is used, either before or

after stabilization of the base material [34, 75]. For thin films, often a subsequent deposition of a metal layer is conducted, thereby segregating or diffusing in a subsequent thermal treatment step [75–77]. Another possibility is ion implantation [78].

Pure metal oxides often show high catalytic activity. Examples are the p-type oxides CuO and Co_3O_4. CuO has been reported to enhance the CO-selectivity compared to H_2 of SnO_2 [79], SnO_2-ZnO [80, 81], ZnO [82] and In_2O_3 [79]. Here, both a spill-over [82] and a Fermi-level control mechanism are suggested [79, 80]. The literature examples for materials reported for CO detection are summarized in Table 2.4.

Table 2.4. Overview: Metal oxide materials of CO sensors reported in the literature. References in **bold** indicate that the gas sensitive layers were deposited by PLD.

Additive/ Material	**SnO_2**	**In_2O_3**	**WO_3**	**ZnO**	**CuO**	**CrO_x**
-	[41, 80, 83–85]	[86]	[87]	[80, 88, 89]	[46]	-
Pd	[90, 91]	-	-	-	-	-
Pt	[90], **[92, 93]**, [78, 94]	-	-	-	-	-
Au	**[90, 95]**	[86]	**[95]**	-	-	**[95]**
Ni	[78]	[86]	-	[89]	-	-
Al	-	-	-	[96]	-	-
W	-	[86]	-	-	-	-
Ti	-	[86]	-	-	-	**[95]**
Co	-	[86]	**[97]**	-	-	-
Sn	-	[86]	**[97]**	[80]	-	-
Cr	-	[86]	-	-	-	-
Zn	[80, 81]	[86]	-	-	-	-
V	[78]	[86]	-	-	-	-
Mn	[86]		-	-	-	-
Cu	[79–81]	[86]	-	[80, 82]	-	-
Y	-	[86]	-	-	-	-
Zr	-	[86]	-	-	-	-
Mo	[86]	-	-	-	-	-
Rb	[86]	-	-	-	-	-
Ga	-	-	-	**[98]**	-	-
In	[78]	-	-	-	-	-
Sb	[78, 94]	-	-	-	-	-

2.3. Thin Film Gas Sensors

Conventional metal oxide gas sensors are constructed by sintering pellets or by deposition of thick film slurry, using methods such as screen printing or drop coating. In the following, we refer to thin films having a thickness below 5 μm

and if they are created through thin film deposition methods. These can be either physical vapor deposition (PVD), chemical vapor deposition (CVD) or liquid-based such as spray pyrolysis. Examples of thin film methods are described in the following [17, 99, 100]:

- **Thermal and e-beam evaporation:** Historically, one of the first methods used to deposit MOX thin films for gas sensing, see e.g. Ref. [101–104]. The oxygen stoichiometry control is more difficult than in sputtering because of the low ambient pressure.

- **Sputtering:** A PVD technique that is among the most used for the preparation of thin film MOX. Consequently the literature on sputtered MOX thin films for gas sensing is reviewed in the following section.

- **Ion-beam assisted deposition:** Good adhesion to the substrate is often reported for this PVD method [105].

- **Rheotaxial growth and thermal oxidation (RGTO):** This is a PVD technique used to prepare porous thin films of SnO_2 [99, 106]. A thin tin film is deposited, e.g. by sputtering or thermal evaporation at a temperature above the melting point of tin. The tin metal forms liquid droplets by dewetting and is subsequently transferred to tin oxide by thermal treatment in an oxygen ambient [107, 108].

- **Pulsed laser deposition (PLD):** This is another PVD technique with which highly oriented films can be created at a low temperature [17]. Using this method, a large range of deposition parameters is available, enabling the deposition of dense to porous films. PLD for gas sensing is reviewed more intensively in Section 2.4 as it is the method used in this work.

- **Spray pyrolysis:** In spray pyrolysis, a metallic compound dissolved in a liquid is decomposed in a pyrolytic process [17]. By control of the process parameters, dense-to-porous films can be produced [109]. Flame-spray pyrolysis (FSP) is an advanced spray technique where nanoparticles are formed in a flame and suitable to deposit layers with a high degree of porosity [70].

- **CVD:** This technique requires high temperature of at least 400 °C. Here, organometallic compounds are oxidized in situ with oxygen, water, and hydrogen peroxide.

- **Atomic layer deposition (ALD):** A characteristic of this CVD technique is, that it is self-limiting. Thus, controlled deposition of single monolayers is possible. This technique is used to grow thin, homogeneous films with a thickness of less than 100 nm [110–112].

Sberveglieri *et al.* reviewed thin film gas sensors in the early 1990s [106, 113]. A more recent review focusing on the structural modification in MOX gas sensing, also including those deposited by thin film methods, was published by Korotcenkov in 2005 [109]. In the following, both older and more recent results are reviewed. Several tables are included where reported thin film gas sensors are compared, including film thickness, target gas, and sensor signals as defined by Equations 2.37 and 2.38. Publications on gas sensing are generally difficult to compare because often only a small number of gases is measured, and both humidity and operation temperature vary. Additionally, the high non-linearity of the gas response (see Chapter 2.1.7) leads to difficulties in the comparison of signals measured in different concentration regimes, and the reproducibility of materials is also often limited.

Historically, thin films have been investigated from the beginning of MOX sensor development and are among the first published studies on this topic, e.g. by Seiyama *et al.* [10, 101]. They were less sensitive when compared to later reports in Taguchi's patent [11]. After that, research and development focused on the development of sintered ceramic sensors. However, several studies were performed in the 1970s on MOX thin film sensors [41, 114]. In the 1990s, research on thin film gas sensors gained increased popularity, because of the upcoming possibilities of micromachining and miniaturization of sensors.
High response of thin film gas sensors to reducing gases, such as CO or H_2 at low concentrations, is rarely found in the literature, when compared to state-of-the-art thick film sensors. Simon *et al.* [115] concluded that the response of thin film sensors to oxidizing gases is comparable with classical sensors, while the response to reducing gases is lower. Promising results of thin film sensors for oxidizing gases are reported e.g. for In_2O_3-based films by Gurlo *et al.* [64]. A thin film sensor on In_2O_3 basis was developed by the company FIS for sensing of ozone [116]. Besides their often limited sensitivity, another drawback of thin film MOX sensors is that they are often reported to show limited long-term stability. This was attributed to the limitations of thermal treatment for the thin film materials on devices with metal electrodes [102], resulting in insufficient oxygen stoichiometry.

2.3.1. Thin film gas sensors prepared by sputtering

Thin films for gas sensing prepared by sputtering (a PVD method) are very often studied in the literature. Table 2.5 represents an overview of reports, exemplary for the case of SnO_2. Sputtered thin films are generally showing superior quality. They grow densely on the surface and show mostly compact columnar structure. Crystalline metal films can already be achieved by room temperature deposition. However, this is not reported for MOX films in most cases. They are generally amorphous when deposited at low temperatures, e.g. less than 200 °C for SnO_2, and can be crystallized during a subsequent annealing step [17]. These films can be deposited by reactive sputtering, using metal targets in an atmosphere containing oxygen, or otherwise by radio frequency sputtering of ceramic targets. Also in the latter case, oxygen might be necessary in the sputtering atmosphere to improve the stoichiometry of the deposited layer. The morphology of the thin films is typically different compared to conventional screen-printed and fired MOX films which show a high degree of porosity.

Chang *et al.* [114] investigated sputtered thin films for nitrogen oxide (NO_x) gas detection and found a relatively high resistive response to 50 ppm NO_x, compared to the cross-sensitivity to CO and other investigated gases in the same concentration range. This high response for SnO_2 thin films to oxidizing gases was later on reported in many studies [78, 102]. The main reason for this is most likely the high concentration of oxygen defects and the high conductivity, compared to thick film sensors, along with a compact film structure that reduces the impact of the depletion zone on the signal (Equation 2.10). Hence, it is often found that the signal increases with decreasing film thickness [102, 117]. One explanation is given by Schierbaum *et al.*: The signal to NO_2 could be more surface (chemisorption) dominated, whereas the signal to CO is more inter-grain dominated [117]. Oxidizing gases often show high surface reactivity which limits the use of diffusion-dominated porous materials. Studies on donor-doped conducting MOX thin films such as vanadium-doped SnO_2 [78] or tin doped indium oxide (ITO) [99, 118, 119] further support this hypothesis. In these studies a selective response to oxidizing gases was seen.

In contrast, only a few exceptions of sputter-deposited thin film sensors with good response to reducing gases have been reported (see Table 2.6 for SnO_2, Table 2.7 for other oxides). Demarne *et al.* [123] found signals S_{red} of up to 200 for 100 ppm H_2 at an operating temperature of 400 °C for a special type of sputtered layer with nanosized crystallites. In this case, this morphology was reached by deposition of an amorphous film and subsequent crystallization by thermal annealing in nitrogen. Steffes *et al.* [124, 125] investigated nanocrystalline gas-sensitive thin films, that were produced by introducing N_2 in the

Table 2.5. Examples for sputtered SnO_2 thin films for sensing oxidizing gases, as reported in the literature; n.s. stands for *not specified*.

Additive	Thick. range/ nm	Gas	Gas conc./ ppm	Signal relative	Oper. temp./ °C	Ref.
-	100	NO_x	20	21	250	[114]
In, Bi_2O_3	300	NO_x	100	200	280	[99]
Ni, In, Sb, V, Pt	60–100	NO_2	12.5	44	200	[78]
-	290–500	NO_2	0.1	29	n.s.	[120]
-	430	NO_2	50	29000	100	[121]
various	430	NO_2	10	5000	100	[122]

Table 2.6. Examples for sputtered SnO_2 thin films for sensing of reducing gases reported in the literature; n.s. stands for *not specified*. LPG: liquified petroleum gas.

Additive	Thick. range/ nm	Gas	Gas conc./ ppm	Signal relative	Oper. temp./ °C	Ref.
-	50–300	CO	36	1.5	300	[41]
Sb_2O_3, Au	600	H_2	100	6.5	327	[76]
-	10–400	H_2	100	200	400	[123]
SiO_2-filters	n.s.	CO	2000	148	450	[126]
-	1000-5000	ethanol	5	1	320	[127]
Pt	60	CO	100	1	360	[128]
Pt, Pd	300	CO	1000	8	300	[129]
various	90	LPG	50	741	280	[130]
Pd	90	methane	200	200	200	[131]

sputtering atmosphere of the In_2O_3 deposition. By additional Ta-doping, good sensing behavior was also found for reducing gases [124, 125]. However, the influence of the nitrogen input into the films on their long-term stability is not yet fully investigated and understood.

2.3.2. Thin film gas sensors prepared by other deposition techniques

Porous RGTO films have been shown to detect high concentrations of H_2 (1000 ppm) [99] and NO_x (100 ppm) [106], compare Table 2.8. They can be doped with Pd or Au and integrated in microelectromechanical systems (MEMS)-type hotplate devices and used for the detection of low CO concentrations (25 ppm) [107]. Films deposited by spray pyrolysis (undoped SnO_2) have been shown to detect low CO concentrations in dry synthetic air [142]. The adaptation of the pyrolysis temperature leads to a wide range of film morphologies achievable with this technique [109]. Korotcenkov *et al.* found a strong correlation between electrical resistance and gas response for films deposited

Table 2.7. Examples for sputtered MOX (non-SnO_2) thin films for gas sensing reported in literature, n.s. stands for *not specified*. LPG: liquified petroleum gas.

Material	Additive	Thick. range/ nm	Gas	Gas conc./ ppm	Signal relative	Oper. temp./ °C	Ref.
Co_3O_4	-	380	CO	50	0.24	240	[132]
CuO	-	48–93	O_3	0.3	3.4	200	[133]
$CuAlO_2$	-	200	O_3	0.07	100	300	[134]
$LaFeO_3$	-	150–1600	NO_2	10	34	400	[135]
MoO_3	-	300	CO	100	3	400	[136]
ITO	-	n.s.	NO	10	59	300	[99]
In_2O_3	various	n.s.	CO	2000	79	450	[126]
$In_xO_yN_z$	-	150	NO_2	10	400	200	[124]
$In_xO_yN_z$	Ta_2O_5	120	CO	60	1	450	[125]
In_2O_3	Ga_2O_3	60–250	LPG	5000	7	250	[137]
In_2O_3	-	240	O_3	0.1	0.36	25	[138]
WO_3	-	n.s.	NO_2	1	1.3	200	[139]
WO_3	TiO_2	100	H_2	300	29	150	[140]
ZnO	Al	65–390	CO	1000	0.6	400	[96]
ZnO	-	300	NO_2	5	3	280	[141]
ZnO	Cu	260	CO	40	2	350	[82]

by spray pyrolysis with higher response for films with higher resistivity [143]. Flame spray pyrolysis was successfully employed to deposit nanoparticles of Pt-doped SnO_2 for sensing of CO in dry and humid atmosphere [144]. This technique can also be used to directly deposit highly porous layers on substrates. However, these are more likely thick films than thin films [145].

ALD films are referred to as models for compact films with thicknesses in the range of the Debye length due to the well-controllable self-limited layer-by-layer growth of films. As reported in a review by Choi and Park [89], ALD-grown SnO_2 films can show high conductivity. This results from the incorporation of oxygen defects during growth, thereby limiting their response to reducing gases. For crystalline SnO_2, an increase in the sensor signal with a decrease in film thickness was reported [111] when the thickness reaches the range of the depletion zone. It has to be kept in mind that this is an interplay between electrical conductivity and film thickness, both of which are not always independent parameters, as the stoichiometry might change during deposition [111]. Thin films prepared by ALD or by CVD have also been used for the sensing at room temperature by using ultraviolet light desorption [146]. For this application, due to the interaction of ultraviolet light with the surface, the compact structure of the films is beneficial. However, as of today, the use of ALD for

Table 2.8. Examples for non-sputter-deposited/PLD SnO_2 thin films for gas sensing, as reported in the literature; n.s. stands for *not specified*.

Additive	Deposition method	Thick. range/ nm	Gas	Gas conc./ ppm	Signal relative	Oper. temp./ °C	Ref.
Pd	vacuum depos.	300–350	CO	1000	0.2	250	[147]
-	e-beam evap.	10–100	NO_2	5	3.5	200	[102]
Pt, Pd	e-beam evap.	50	CO	100	5	250	[104]
Pt	evapor. + oxid.	270	butane	250	0.5	400	[148]
Cu	thermal evapor.	320	H_2S	20	10^6	140	[149]
Pd	RGTO	300	H_2	1000	350	220	[99]
Au	RGTO	350	CO	250	3	400	[107]
-	RGTO	40–300	CO	100	0.3	400	[108]
-	sol-gel	10–150	H_2S	1.5	300	200	[150]
-	sol-gel	100–480	C_2H_6O	700	245	220	[151]
various	sol-gel	100	CO	100	1	300	[152]
Pd	spray pyrol.	80–100	H_2O	n.s.	n.s.	n.s.	[153]
-	spray pyrol.	5–100	H_2	20000	200	400	[143]
-	spray pyrol.	50–100	CO	4	0.1	350	[142]
-	spray pyrol.	40–340	O_3	1	10^4	230	[154]
Co	spray pyrol.	25–400	O_3	1	10^4	250	[155]
Pd,F, Pd-F	spray pyrol.	-	CO_2	5000	0.2	100	[156]
-	MOCVD	500	H_2	1000	19	450	[157]
-	ALD	10–200	CO	5000	5	300	[158]
-	ALD	2–100	CO	10000	19	450	[111]
-	ALD	1.6–5.3	CO	10000+	5	325	[112]

the preparation of semiconducting MOX is not yet well established, with the exception of ZnO [110].

2.4. Pulsed Laser Deposition

Pulsed laser deposition, or PLD, was originally developed in the 1980s to grow complex oxides for application as high temperature superconductors [159, 160]. It was discovered that those oxides could be stoichiometrically transferred and the growth was highly ordered. Hence, an epitaxial or quasi-epitaxial growth can be reached at relatively low temperatures compared to other PVD methods [161, 162]. The limitation of the deposition to the lateral extent of the plume and resulting difficulties in uniform deposition on large areas are often described as drawbacks of PLD. The formation of micron-sized particles that are deposited as *droplets* on the substrate are a further disadvantage.

2.4.1. The basic concept of PLD deposition

Material ablation is possible with both continuous-wave and pulsed lasers. Pulsed lasers are used primarily to realize high peak powers above the thresholds for material ablation. These are reached with relatively low average power. However, pulse length and emitting wavelengths λ can significantly impact the material interaction process. Different kinds of lasers are reported in the literature for use in pulsed laser ablation, e.g. CO_2 lasers ($\lambda = 10.6\,\mu m$) and solid-state lasers such as Nd:YAG ($\lambda = 1064\,nm$) [163, 164], both emitting in the infrared. Excimer lasers are popular in PLD applications. They emit in the ultraviolet and have pulse length up to 100 ns (e.g. ArF $\lambda = 193\,nm$ [165], KrF $\lambda = 248\,nm$ [166, 167], XeCl $\lambda = 308\,nm$ [168]). Here, the photon energy is larger than the band gaps of the oxides, so the absorption of the laser light is strongly enhanced. Another feature of excimer lasers is their high peak power.

Excimer lasers can be easily pumped by electric discharges, making a sophisticated pumping by another laser unnecessary. The term *excimer* originates from the words *excited dimer*. Noble gases or nitrogen that form the *dimer* molecules in an excited state with a short lifetime were used in the first excimer lasers. Today, combinations of noble gases and halogens are used in practical applications. If the gas mixture is electrically pumped, the energy level of the gas species increases and the noble gas atoms are ionized, forming e.g. Kr^+ in the case of a KrF lasers [169]. At the same time, the halogen molecules are dissociated, forming F atoms. Collisions form complex molecules, e.g. KrF*, with the asterisk indicating an excited state. The excited complexes decay to KrF by emission of radiation. As they are not stable in the ground state, they rapidly dissociate, yielding a perfect population inversion.

The PLD process can be divided into four sub-processes:

1. Absorption of the laser radiation by the target
2. Melting and subsequent evaporation of the target material, *ablation*
3. Plasma expansion into the surrounding media
4. Deposition on the substrate

In sub-process 1, the incident laser radiation interacts with both the nearly free electrons and the lattice of the target. The interaction with the electrons is faster due to their lower inertness. The following relations are found for the typical relaxation time constants of electrons τ_e and lattice τ_l:

$$\tau_e = \frac{C_e}{\gamma_{el}},\ \tau_l = \frac{C_l}{\gamma_{el}}, \tag{2.39}$$

where γ_{el} is the coupling-constant of the electron and the lattice, and C_{e} and C_{l} are the heat capacities of electrons and the lattice respectively. τ_{e} is typically on the order of a few ps and τ_{l} on the order of a few ns. Therefore, the interaction of lasers of different pulse lengths τ have different effects on the material. For ns lasers, there is $\tau \gg \tau_{\text{l}} \gg \tau_{\text{e}}$. The laser pulse interacts both with the electrons and the lattice, so the interaction takes place in the *thermal* regime [170, 171]. Thus, the material is first melted, then evaporated and heat transfer takes place by conduction into the target [172]. Consequently, a large heat-affected zone occurs around the laser-irradiation spot. For ps lasers, we find $\tau_{\text{l}} \gg \tau \gg \tau_{\text{e}}$, so the interaction with the electrons and thus the heat-conduction through the electrons is important. However, compared to a ns laser, the heat-affected zone is reduced in its lateral dimensions.

The ablation threshold of the material—in sub-process 2—depends on the fluence (energy per area) of the laser pulse. The erosion threshold fluence F_{th} in turn depends on the density ρ, the reflectivity R_{r}, the sublimation enthalpy ΔH_{s}, the absorption coefficient α_{abs}, and the molar mass M:

$$F_{\text{th}} \cong \frac{\Delta H_{\text{s}} \cdot \rho}{(1 - R_{\text{r}}) \cdot \alpha_{\text{abs}} \cdot M} \,. \tag{2.40}$$

This threshold value depends both on the material of the ablated target and the wavelength of the incident radiation. Also, at high energies non-linear effects might occur. In PLD, typical fluences in the range of 1–10 J/cm^2 are used [170].

The third sub-process of PLD deposition is of even greater relevance for the morphology of the growing films. For low laser fluences, the laser light is hardly attenuated by the plume of the evaporated material [172]. The plasma formation in PLD, in a plume orthogonal to the surface, occurs already during the evaporation process, if a certain threshold for plasma formation is reached. The high surface temperature results in vaporized material that is already partly ionized, the so-called *thermionic emission* [170]. Further ionization occurs due to the interaction of the evaporated material with the incident laser light. Here, a complex interaction between the plasma and the laser radiation occurs. An inverse bremsstrahlung (the absorption of light by free electrons) is the main absorption process in the plasma [170, 172]. It accelerates the electrons that contribute to the further ionization of neutral species by subsequent collisions. Additionally, radiation is absorbed by neutral species in the plume, thus leading to further generation of charged species by photoionization. Due to the high

concentration of neutral species in the plasma plume [170], this process is important for the absorption energy.

The interaction between plasma plume and laser irradiation represents a typical feature of the PLD process. It leads to an acceleration of the plasma vapor species and results in high energy deposition on the substrate with increased surface mobility [173]. The process equilibrium of the plasma is maintained by the increased light absorption of a high-energetic plasma, leading to a decrease in vapor generation [170].

For deposition of thin films, often background gases such as oxygen and nitrogen are applied, which reduce the plasma energy by collisions with the surrounding gas (*thermalization of the plasma*). This improves incorporation of light elements into the layer or may even be necessary to allow the deposition of oxides from metal targets in reactive PLD. Sub-process 4 (deposition on the substrate) is discussed in the following chapter.

2.4.2. Growth kinetics and morphology control in PLD

For PL-deposited thin films, the growth model established by Thornton in 1974 for sputter-deposited films is also generally valid [174, 175]. In this model, different growth zones are introduced depending on the substrate temperature T. They are referred to as a value T_r relative to the melting temperature T_m ($T_\mathrm{r} = T/T_\mathrm{m}$), see illustration in Figure 2.10:

- **Zone 1:** Shadowing: At very low $T_\mathrm{r}= T/T_\mathrm{m} < 0.3$, the crystallites are columnar with domed tops. The crystallites show a high number of voids and defects. This is due to low thermal energy of the reactants, thus inducing low surface diffusion [174, 176].
- **Zone 2:** $0.3 < T_\mathrm{r} < 0.5$, surface diffusion: leads to dense, columnar polycrystalline structure, and a smooth surface. Defects appear mainly in the boundary regions between the grains.
- **Zone 3:** $T_\mathrm{r} > 0.5$, bulk diffusion: Columnar growth of larger grains, with grain diameter increasing with the temperature. Crystalline quality is enhanced with a small number of defects.

Thornton [175] found that, in addition to the substrate temperature, the ambient pressure is of importance, as it decreases the kinetic energy of the species and their mobility. Elevated gas pressure results in a more porous microstructure of films [176]. Thornton also introduced an additional transition zone *T* between zone 1 and 2, see Figure 2.11. Here, fibrous grains are created and no voids are formed between them. This is due to decreased energy of the particles

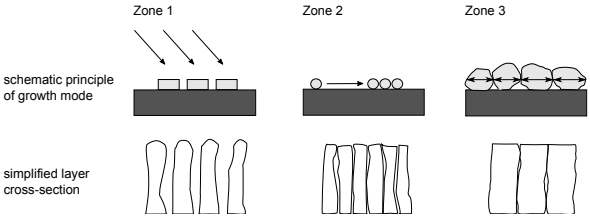

Figure 2.10. Illustration of the dominant effects on thin-film growth according to the models of Thornton and Movchan-Demchishin. For annotation, see text.

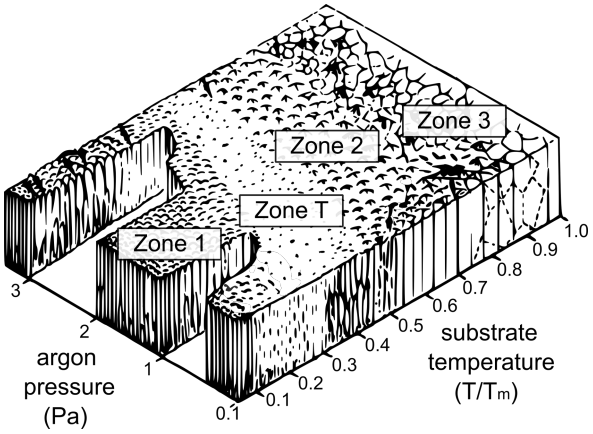

Figure 2.11. Thornton: Zone model for growth of sputtered films [175].

when their interaction with the surrounding gas is enhanced. The actual values of the zone borders are strongly depending on the deposited material.

The morphology of PL-deposited films follows this model. In the medium pressure range at higher temperature, films of good crystalline quality can be prepared by PLD. More generally, one can assume that the same growth regimes are found in the case of PLD. The difference is in higher pressures compared to sputtering in comparable zones, because the kinetic energy of the PL-ablated species is higher. However, for very low-pressure and high-pressure growth, this model has to be extended, as PLD can be conducted in a quasi-vacuum and at high pressures such as 50 Pa. Figure 2.12 illustrates the extended growth regimes for PLD. The high pressure regime, with values higher than that of

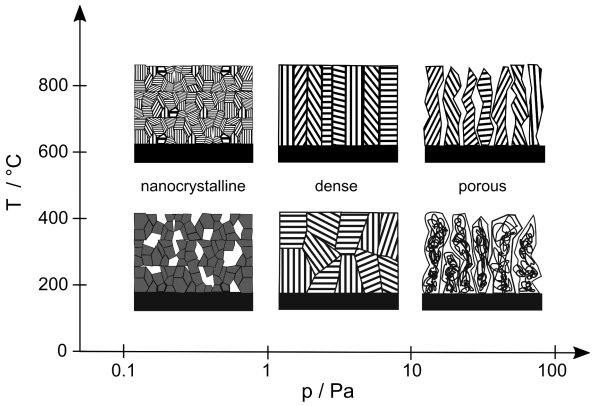

Figure 2.12. Schematics of PLD morphology dependent on growth temperature and pressure, after Infortuna *et al.* [174]. Here the growth regime of porous films due to nanocluster formation in the plasma is also illustrated in the right part of the graph.

most other physical vapor deposition processes, can be accessed, as plasma discharge is realized without electrodes [173]. If high deposition pressures are employed, nanoclusters are already formed in the plasma plume and subsequently deposited on the substrate [160, 174]. These clusters, with typical sizes in the range of 1–50 nm, are formed due to more frequent collisions in the gas phase, while at very low pressures, the ions are not scattered. Particle nucleation occurs due to supersaturation of the plasma. The ambient gas limits its expansion and increases the probability of collisions between the ablated particles. Droplets and particles that are directly ejected from the target are a lot larger ($0.1-10\ \mu m$) than clusters. Being more an agglomeration of particles than a dense film, the highly porous films formed by these clusters have rather poor adhesion to the substrate. The adhesion can be increased by increased deposition temperatures [174]. At higher temperatures, the particles dissolve into columnar grains, building a highly porous columnar structure.

2.4.3. PLD of tin oxide

The first studies on SnO_2 films found in the literature were aimed at creating compact films of good quality at low temperature. In 1990, Dai *et al.* [177] reported on transparent conducting tin oxide films by PLD using ceramic oxide targets and a Nd:glass laser at 1.06 μm. The layers showed a good orientation along the (200)-plane despite their deposition at room temperature. This was

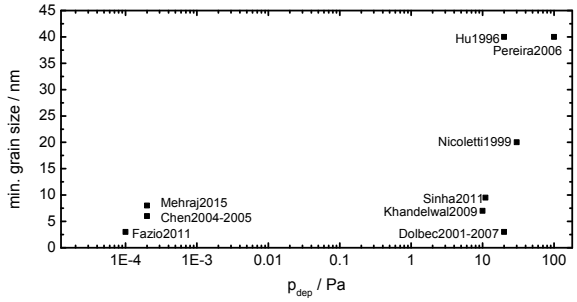

Figure 2.13. Literature overview showing the resulting grain size as a function of deposition pressure for nanocrystalline SnO_2 thin films prepared by PLD. References: Hu1996 [178], Nicoletti1999 [179], Dolbec2001-2007 [92, 93, 166, 183, 187], Chen2004-2005 [167, 186, 188], Pereira2006 [168], Khandelwal2009 [181], Fazio2011 [185], Sinha2011 [189], Mehraj2015 [190]

explained by the high energy in the plasma plume. In later studies, it was investigated, how the film properties are influenced by the deposition conditions. In most cases, KrF excimer lasers were used, see Table 2.9. Hu *et al.* [178] found that the grain size increased with higher deposition temperature for post-annealed films prepared from either metallic or ceramic targets. Different research groups prepared nanocrystalline tin oxide films by PLD. Using a KrF laser, films were prepared by a ceramic target at an oxygen pressure of 30 Pa [179]. A XeCl excimer laser was used to prepare films reactively using a metallic target and a background oxygen pressure of 0.21 Pa [180]. PLD was later used to deposit films for transparent conductors [181] or thin film gas sensing. It was seen that nanocrystalline SnO_2 could be prepared by deposition at higher pressure in the range of more than 10 Pa [92, 166, 168, 182–185]. However, as already stated in the previous chapter, the nanocrystalline grain growth is also possible in PLD in the low-pressure range of quasi-vacuum, as seen for SnO_2 [167, 185, 186]. The deposition conditions are illustrated in Figure 2.13.

SnO_2 can be deposited almost stoichiometrically and with larger grain sizes [185, 191] in the medium pressure range. This is consistent with the film growth dynamics presented in the preceding chapter. Details of deposition pressures and temperature are summarized in Table 2.9. In most cases, the deposition pressure is either higher than 300° C [184] or the film was annealed after deposition to reach a high degree of crystallinity [167].

Table 2.9. Overview of SnO_2 thin films prepared by PLD reported in literature, n.s. stands for *not specified*.

Year	Gas sensor	Laser	Max. fluence/ (J/cm^2)	Max. dep.temp./ °C	Min. dep.press./ Pa	Max. dep.press./ Pa	Ref.
1990	No	Nd:glass	150	25	$5 \cdot 10^{-5}$	$5 \cdot 10^{-5}$	[177]
1991	Yes	KrF	2	500	20	20	[192]
1996	Yes	KrF	2.5	500	20	20	[178]
1999	Yes	XeCl	10.8	25	0.2	10	[180]
1999	Yes	KrF	0.9	550	30	30	[179]
2001	Yes	KrF	6	600	10^{-4}	15	[93]
2001	Yes	Nd:YAG	0.25	375	0.02	0.02	[163]
2002	No	KrF	4.6	600	10^{-4}	15	[183]
2003	Yes	KrF	6	300	0.1	20	[92]
2003	No	KrF	6	600	15	15	[187]
2003	No	KrF	n.s.	900	1	1	[193]
2003	Yes	Nd:YAG	3.8	500	10	10	[77]
2004	No	KrF	5	25	$2 \cdot 10^{-4}$	$2 \cdot 10^{-4}$	[186]
2005	No	KrF	1.6	25	$2 \cdot 10^{-4}$	$2 \cdot 10^{-4}$	[167]
2005	No	XeCl	12	25	10^{-5}	100	[182]
2006	No	XeCl	10	25	0.01	100	[168]
2007	Yes	KrF	4.6	300	10	10	[166]
2008	No	KrF	3	800	50	50	[184]
2009	No	XeCl	10	400	10	10	[181]
2010	Yes	Nd:YAG	n.s.	700	1000	1000	[164]
2010	No	KrF	1	500	$2 \cdot 10^{-4}$	67	[191]
2011	No	KrF	1	127	10^{-4}	67	[185]
2011	No	KrF	n.s.	600	11	11	[189]
2013	No	KrF	n.s.	800	5	5	[194]
2015	No	KrF	n.s.	25	$2 \cdot 10^{-4}$	$2 \cdot 10^{-4}$	[190]
2016	No	KrF	2.2	700	0.1	30	[195]

2.4.4. PLD of tin oxide for gas sensing

PLD was used in earlier publications to prepare SnO_2 for gas sensing [164, 180]. Deposition conditions are summarized in Table 2.10. It was also shown to be compatible with micromachined hotplates [163, 179]. Noble metals were introduced into the PLD layers by subsequent ablation of a metal target [179] or by ablating a Pt wire positioned on the target [92]. It was found that these layers have a good response to 50 ppm CO in dry air with a relative resistance change of up to a factor of four [92]. DC sputtering of Pd after the PLD process led to an increased response to H_2 [77]. In more recent studies, highly porous vanadium oxide was prepared by PLD for gas-sensing applications [196, 197].

Table 2.10. Examples for PLD SnO_2 thin films for gas sensing reported in the literature; n.s. stands for *not specified*.

Year	Additive	Thick. range/ nm	Gas	Gas conc./ ppm	Relative signal	Oper. temp./ °C	Other inves. gases	Ref.
1999	Au, Pt, Pd	380	benzene	1	3	400	CO	[179]
1999	-	-	ethanol	60	7	450	-	[180]
2001	Pt	250	CO	50	2.7	200	-	[93]
2001	-	1000	H_2	1000	0.1	n.s.	-	[163]
2003	Pt	450–600	CO	50	4.5	250	-	[92]
2003	Pd	500	H_2	3100	16	500	-	[77]
2007	Pt	10–1200	CO	50	10	200	-	[166]
2010	-	40–400	NO_2	1000	65	350	H_2	[164]

2.4.5. Concepts of commercial and large area PLD

In order to apply PLD to commercial production, two drawbacks have to be overcome—limited deposition homogeneity and droplet formation. To reach a high surface homogeneity, various concepts have been presented, including target and substrate rotation, lateral movements, and scanning of the laser over the target.

For droplet formation or *splashing*, several reasons are reported in the literature. One is the so-called subsurface boiling. The time to convert laser energy into heat is shorter than the time to evaporate the surface layer. Thus, the temperature of the subsurface rises fast and particles are expelled from the target. This phenomenon most likely occurs at high fluences in metal targets with low melting points [170]. More relevant for ceramic targets are the recoil ejection and the exfoliation [198]. In the former process, the droplet is ejected by the recoil of the plasma shock wave expanding into the bulk. In the latter process, arbitrarily shaped particles appear if the target surface is repeatedly molten by the laser pulses and particles are generated by the exfoliation of surface structures [170]. To avoid having deposits on the substrate, various routes are followed: A decrease in laser power at least reduces the importance of the first two phenomena. The target can be pre-treated, smoothing the surface, to avoid the droplet generation by exfoliation. Another concept is the use of a second laser, resulting in an additional momentum to the particles [199]. Mechanical principles such as a velocity filter to reduce the rate of the particle deposits on the surface are used in commercial PLD systems.

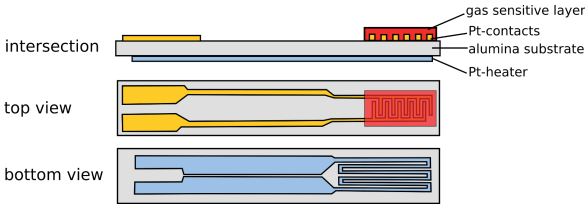

Figure 2.14. Schematic setup of a thick film sensor on a ceramic substrate.

2.5. Micromachined Hotplates for Gas Sensing

The heater provides an operation temperature for the sensor in a good range for adsorption/desorption, cf. Section 2.1.5. The screen-printed sensor's substrate has to be thermally conductive as the heater and the gas sensitive layer are printed on opposite sides of the substrate, see Figure 2.14. The most common substrate material is alumina. A meander-shaped heater is used to make sure a homogeneous heating of the active area where the heat is additionally spread by the substrate. The material of choice is usually platinum due to its high thermal stability [200] and high temperature coefficient of resistance (TCR) [201]. The linear temperature-resistance behavior gives a good possibility to control the heating without additional temperature-sensing devices. Platinum is conventionally also used for the front-side electrodes, which are printed as interdigitated electrode (IDE) structures to reduce the overall resistance of the device. These electrodes provide contact to the chemical-sensing material. The screen-printed MOX layer is structured in the active area of the sensor, determined by the heater and the IDE. It consists of metal oxides and additives. Two contacts are foreseen to apply the heater voltage and two for the resistance measurement.

With the introduction of silicon micromachining for physical sensors in the 1980s, such as pressure sensors and later accelerometers the idea of integrated resistive gas sensors was born [202, 203]. The miniaturization was not only promising to reduce the footprint, but, more importantly, it gave the possibility to reduce the high power consumption of conventional sensors, which is in the range of several Watts and makes battery operation impractical. A good thermal insulation of the heated sensitive layer on a hotplate structure as well as a minimized heated area dramatically reduces power consumption[2]. Additionally, the low thermal mass of the devices ensures a fast heat-up and cool-down time. The resistive principle of the MOX gas sensor—in contrast to e.g. electrochemical cells or optical principles—has the advantage of no correlation between size

[2]Hotplate-type structures are also used in miniaturized mass flow sensors.

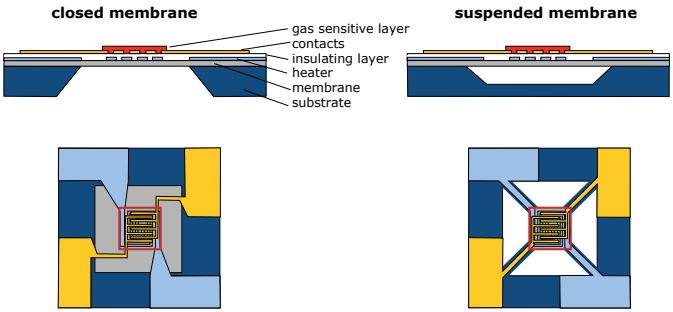

Figure 2.15. Schema of hotplate-type gas sensors membrane-type (left) and suspended (right). Upper images show cross-cut side views, lower images top views.

and sensitivity. However, the first devices with thin films showed the general drawbacks of sensitivity and stability. Micromachined substrates for MOX gas sensors gained increasing popularity after they were shown to be compatible with thick film metal oxide processes [204]. The topic of miniaturized resistive gas sensors was reviewed by researchers such as Sberveglieri *et al.* in 1997 [205], Simon *et al.* in 2001 [115], and Bhattacharyya in 2014 [206]. A number of PhD theses starting in the 2000's also discussed this topic, e.g. Refs. [100, 207–209].

2.5.1. Design of miniaturized hotplates

There exist two popular designs for hotplate-type gas sensors, namely membrane-type and suspended, both possible to fabricate with micro-machining, as illustrated in Figure 2.15. In the first case, the membrane is solid without voids, which leads to good mechanical stability on the one hand and quite important heat conduction over the membrane, on the other. For the suspended-type hotplate, the thermal insulation is improved as heat conduction can take place only over the supporting stripe-structures; however, structures like that are less mechanically stable.

To estimate the important heat-loss paths, an analytical model can be used. We have a closer look at the membrane-type hotplate design for which the relevant heat fluxes are illustrated in Figure 2.16. The first path is heat conduction through the membrane, the second path the conduction through the surrounding air; one part on the upper side of the membrane, the other part on the downside of the membrane toward the package. Third, there exists a thermal conduction path also through the cavity back to the substrate which is not considered in the

analytical model. Additionally, heat is dissipated by natural and forced convection as well as radiation.

The membrane is usually rectangular in shape due to crystallographic reasons. For an estimation of the heat-loss through thermal conduction over the membrane Q_{membrane} with the thermal conductivity λ_{m}, it can be approximated as a round membrane, so the problem can be easily solved in cylindrical coordinates [115]:

$$Q_{\text{membrane}} = \frac{2\pi\lambda_{\text{m}} d(T_{\text{hot}} - T_{\text{amb}})}{\ln(r_{\text{membrane}}/r_{\text{heater}})}, \tag{2.41}$$

where r_{heater} and r_{membrane} are the radii of the heated and the membrane areas respectively, T_{hot} the heater temperature and T_{amb} the ambient temperature. The dependence of the heat loss on the radius of the membrane and heater is logarithmic. This means that there is a saturation behavior of the heat loss over the membrane if a certain aspect ratio between the heater and membrane size of around $r_{\text{membrane}}/r_{\text{heater}} \approx 3$ is reached [115].

Another important heat-loss mechanism is the one through the air via heat conduction and convection. Previous studies showed that, due to the small dimensions of the chip design, convection can be neglected [205]. For a simplified analytical model, heat conduction through the air $Q_{\text{conduction}}$ (thermal conductivity λ_{air}) is modeled by concentric spheres of radii r_{heater} and r_{a} (atmospheric) [205]:

$$Q_{\text{conduction}} = \frac{4\pi\lambda_{\text{air}}(T_{\text{hot}} - T_{\text{amb}})}{1/r_{\text{heater}} - 1/r_{\text{a}}} \approx 4\pi r_{\text{heater}}\lambda_{\text{air}}(T_{\text{hot}} - T_{\text{amb}}). \tag{2.42}$$

In this consideration, the main difficulty to obtain realistic values for both parameters r_{heater} and r_{a}. For r_{heater}, the hot area, we can use a characteristic length of the heater dimension; for r_{a} this is more complex. For an estimation, the distance between the hot area and the cold housing can be utilized.

As for MOX, the operation temperature is in the range of approx. $300\,^{\circ}\text{C}$; heat loss due to radiation $Q_{\text{radiation}}$ is less relevant. The following equation describes the strong temperature dependence of radiation losses:

$$Q_{\text{radiation}} = \pi r_{\text{heater}}^2 \sigma\epsilon T_{\text{hot}}^4, \tag{2.43}$$

where σ is the Stefan-Boltzmann constant and ϵ is the emissivity.

For the realization of a resistive sensor, the thermal distribution in the active area is crucial to ensure that the MOX material is heated homogeneously. Here, the design of the meander and the width of the conductive path can be adjusted.

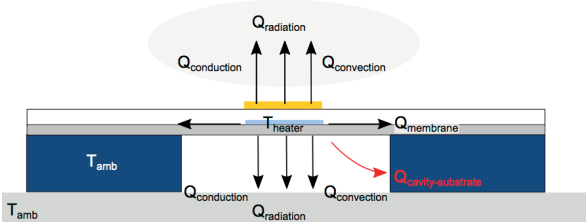

Figure 2.16. Schematic of the heat fluxes Q of a membrane-type gas sensor. The heat conduction path through the cavity to the substrate is not included in the analytic model.

Different meander-shaped heaters have been reported, with both heater and IDE being on the same level (heater around the active area) [210, 211] or with the heater underneath the active area [107, 203, 204, 212–215]. The first possibility is easier regarding processing because only one metallization is needed. However, to have a homogeneous heat distribution, the membrane should be thermally conductive at least in the active area, which has negative impact on the overall heat dissipation of the sensor. If both heater and IDE are stacked, the design of the heater for homogeneous heating is easier. Two metal layers have to be deposited and structured separately, as they are separated by a thin electric insulating layer, though. For this separating layer, good thermal conduction properties are less important, as the thickness of the layer is typically three orders of magnitudes lower than the lateral dimensions of the membrane. Possible designs are summarized in [206]. The design of the heater and hotplate dimensions can be further optimized by using electro-thermal simulations of FEM tools such as *COMSOL* or *ANSYS*.

2.5.2. Materials and processes

Hotplate structures are usually manufactured by etching of the silicon substrate itself (bulk-micro-machining) to realize large cavities. For membrane-type sensors, the membrane can be released by etching from the backside in a dry or wet etching process. For wet etching, potassium hydroxide (KOH) or tetramethylammonium hydroxide (TMAH) etchants are suitable, which etch silicon anisotropically, stopping at the {111}-planes [202–204, 216, 217]. Here, the resulting slope of the membrane results in larger spare areas. With anisotropic dry etching processes, by the deep reactive ion etching (DRIE) such as the Bosch process [218, 219], nearly 90-degree edges are possible. The main drawbacks of the process are the costs and the difficulties of through-wafer etching. For suspended membrane-type sensors, the membrane can be also released from

the front side by either KOH or isotropic wet etching. Else, a sacrificial layer technology can be utilized [207].

For the membrane, silicon oxide, silicon nitride [207], or a stress optimized stack of both can be used [100]. Both materials provide good thermal insulation, with nitride being the better thermal conductor (λ_{th}=1–30 W/mK) [206]. However, it should be kept in mind that the thermal conductivity of the materials is both process and temperature dependent [200]. The heater material should be of good conductivity, thermally stable, show low tendency to electromigration, and be compatible with the other MEMS processes in production. Polysilicon [217] has the benefit of being resilient to hot spots because of its negative temperature coefficient of resistance, but it shows limited long-term stability at elevated temperatures. Metals such as gold [202, 203] and tungsten [219] have been used. For process compatibility, aluminum is interesting because it is the standard integrated circuit (IC) metallization [100] and shows good compatibility with back-end silicon processes. Platinum is used in most studies due to its high temperature stability and high TCR, which supports the temperature control of the hotplate [100, 204, 207, 209].

3. Experimental

3.1. Process Technology

In this work, a process technology for resistive thin film gas sensors based on pulsed-laser deposited (PLD) metal oxide was developed. The focus was on the electrode contact structure and the gas sensitive films. Membranes for thermal isolation were not coated with sensitive material, but investigated for their thermal properties. Resistive platinum contact structures were prepared using thin film processes in a clean room. Metal oxides were deposited through a shadow mask by means of large area PLD on silicon chips with the Pt contact structures. After deposition, the structures were thermally annealed in an oven to stabilize the films. Then, the resulting chemiresistors were either directly measured by placing them on a heated chuck or mounted on a ceramic heater. Finally the contacted and structured thin films were characterized by measuring the resistance and resistance change in a constant flow of test gases.

3.1.1. Metal electrode structuring by lift-off

Design of interdigitated electrodes

Platinum as a noble metal has the advantage of being highly stable for thermally and chemically harsh environments [220]. It was used to prepare the contacts of the thin film gas sensors with a thin titanium film used as an adhesion promoter. Platinum can be etched by wet-chemistries in some hot acids such as aqua regia [221], by physical processes such as sputter etching and ion beam etching [222], or by combined physical-chemical dry etching processes such as reactive ion etching [223]. In this work, a lift-off process for pattering of the platinum films was used so as to avoid problems of physical etching such as the formation of fences. Structures with very smooth edge profiles could be achieved, which are beneficial for the formation of good contacts to the deposited thin film [224]. Hence, cracks close to the steps could be avoided [225]. These smooth edges result from shadowing effects during deposition of the metal films on top of the structured resists. Besides applications in gas sensing [226], layers with defined smooth edge structures are reported for realization of microlenses [227] and optical waveguides [228].

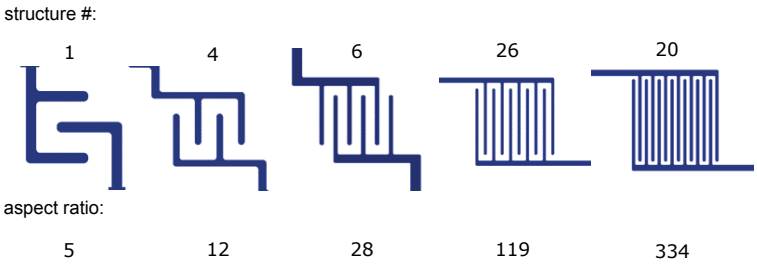

Figure 3.1. Examples of interdigitated electrode layouts with structure numbers and aspect ratio of the IDEs.

As the electric properties of metal oxides are strongly dependent on the preparation conditions, see Section 2.1.4, interdigitated electrode structures were designed with various aspect ratios (length overlap / gap width) ranging from 5 to 334. Additionally, the lateral dimensions of the IDEs were varied to identify size influences with respective size range from 100 to 300 µm. Examples of these are provided in Figure 3.1. A table with the aspect ratio of all platinum test structures can be found in Appendix A. The width of the finger structures was chosen to be 10 µm in most cases, for some smaller structures 5 µm. The lift-off process limits the minimum feature size of Pt structures to 5 µm in the mask layout.

Preparation of bi-layer lift-off resist structures

Lift-off processes are usually conducted using either a negative resist or a double-layer resist. This should avoid deposition of the metal on the edges of the resist as a compact layer, which would hinder the lift-off developer to come into contact with the resist for dissolving it and thus need additional care. As sputter processes are less directional compared to evaporation processes [224], this step is more critical. In the case of negative resist, negative sidewall shapes can be achieved due to the light absorption in the resist, resulting in a higher dissolution rate in the bottom part of the resist. This effect is dependent on the resist thickness. Alternatively, an image reversal resist can be used [119, 229, 230]. In this case, the positive flanks of the positive resist are inversed by a subsequent flood exposure step. This approach has been selected for this work. To improve the undercut and to optimize the profile of the structured metal layer, a non-photosensitive lift-off resist is spun additionally below the photoresist, in order to get a stacked structure for bi-layer resist lift-off, as

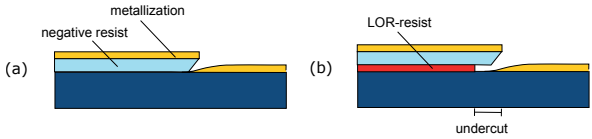

Figure 3.2. Schema of the lift-off process using (a) negative and (b) double resist. After Ref. [234].

depicted schematically in Figure 3.2. The non-photostructurable lift-off resist is dissolved during development and results in a defined undercut. Lift-off resists (LOR, Microchem) were chosen which are based on a polymethylglutarimide platform [231] and were reported to be able to produce high-resolution [231] and high-aspect ratio structures [232]. The double-resist structures were fabricated on 150 mm p-type silicon wafers for lift-off tests and on oxidized 150 mm p-type wafers for the gas-sensing structures. The process flow of the lift-off process using LOR and AZ5214E image reversal resist is illustrated in Figure 3.3. A hexamethyldisilazane (HMDS) coating in an oven was applied in order to improve resist adhesion. To test the resulting lift-off profiles, LOR were prepared in various thicknesses (300 nm, 500 nm, 900 nm, and 1500 nm [233]). The prebake temperature was kept at 190° C for 3 min. The exposure dose for the image reversal resist was optimized by a first exposure series. Five different first exposure doses were used (7.5–37.5 $\mathrm{mJ/cm^2}$). The intensity of the mask aligner was 15 $\mathrm{mW/cm^2}$ and the development time 40 s. The upper images of Figure 3.3 show optical micrographs of the lithographic results after exposure and development. The geometric dimensions of the mask are indicated in the first image. Interference effects at the corners increase with exposure doses. The lower images show the corresponding profiles of the resist edges in a cross-cut (wafer was cleaved) at the respective exposure doses. The profile is very stable for doses higher than 22.5 $\mathrm{mJ/cm^2}$. A first exposure of 7.5 $\mathrm{mJ/cm^2}$ is not sufficient to stabilize the image reversal resist. It results in ripples as can be seen in the top view as well as in the profile of the structured resist. Consequently, a dose of 22.5 $\mathrm{mJ/cm^2}$ was found to be suitable for an accurate geometric transfer of the mask structure to the resist, and this exposure dose was kept constant for all samples. After the first exposure, a reversal bake was performed at 120 °C and a flood exposure of 300 $\mathrm{mJ/cm^2}$ followed.

The development was done using AZ726 MIF developer (TMAH 2.38%, AZ Electronic Materials Corp.) under manual agitation until the windows in the resist were optically clear. An over-development phase followed; the time was varied to achieve different undercut lengths of the LOR. The dependence of the undercut on the dissolution time of the double layer resist was investigated. It was found that the dissolution time of the LOR, which is seen by the

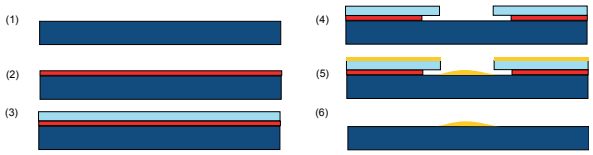

Figure 3.3. Process flow of lift-off structuring: (1) Applying HMDS as an adhesion promoter (2) Spin-on LOR resist + bake (3) Spin-on photostructurable resist + bake (4) UV exposure + reversal bake + flood exposure + development (5) Ti-Pt sputtering (6) Resist lift-off in ultrasonic bath. After Ref. [234].

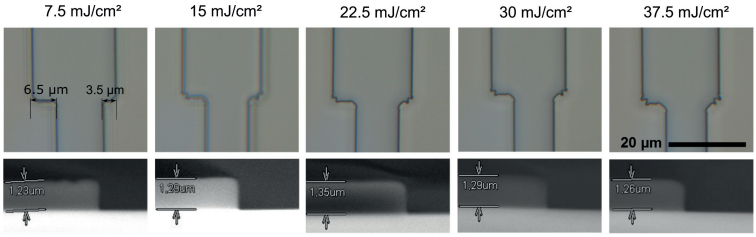

Figure 3.4. Exposure dose test results for AZ5214E image reversal resist variation of the first exposure. Five different first exposure doses were used as specified in the images. For details, see text.

undercut length that can be determined by optical microscopy, is independent of the resist thickness, as seen in Figure 3.4. A constant dissolution rate of approx. 190 nm/min was found, which is partly contradictory to studies using thinner resists [231, 235]. In these studies, an influence of the LOR film thickness on the lateral dissolution rate was seen. The lift-off was done after metal deposition (see next section) by first soaking the sputtered wafers in dimethyl sulfoxide at 40 °C for one hour, followed by an ultrasonic bath at the same temperature for an interval between five minutes and one hour, until the metal layer was lifted off. Due to the high undercut of the bi-layer process, good lift-off results could be achieved.

Sputtering of metal thin films

Platinum thin films with titanium adhesion promoter were deposited using sputter deposition. A schema of the sputtering tool is depicted in Figure 3.6. Sputtering is a physical vapor deposition process that enables large-scale deposition of metals and insulators [236]. Metal deposition sputtering tools are usually operated in direct current (DC). A discharge plasma is formed between the target

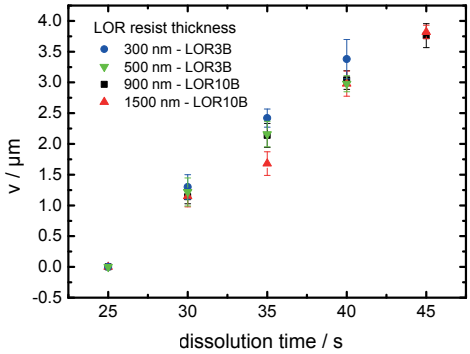

Figure 3.5. Undercut length v and its dependency on the dissolution time for different LOR resist thicknesses (type 3B & 10B) determined by optical microscopy. The width of the line structure was 12 µm, the exposure dose was $22.5\,\mathrm{mJ/cm^2}$. After Ref. [234].

and the substrate. Species of the background gas in the sputtering chamber, usually argon as noble gas, are ionized and accelerated to the target. They vaporize atoms from the target. Subsequently, the atoms are deposited on the substrate. The deposition rate can be increased by installation of permanent magnets (magnetron sputtering), which force the electrons to describe a cycloid course and thus increase the ionization rate of argon [237]. For insulating materials, a radio frequency (RF) discharge plasma can be applied to avoid the electrical charging of the target. Reactive sputtering in an atmosphere containing e.g. oxygen or nitrogen, can also be applied for deposition of oxides and nitrides. In this work, for the deposition of titanium (Ti) and platinum (Pt), DC magnetron sputtering is applied (Leybold Z590 sputtering tool), and the substrate carousel is rotated under the target during deposition. Thus, four wafers can be deposited simultaneously with a good thickness homogeneity. The sputtering time was adjusted to control the thickness of the titanium layer to 30 nm and the platinum layer to 160 nm, with a standard deviation of the thickness of about 12% over the wafer.

The target-to-substrate distance was set to 60 mm. When the distance was extended to 90 mm, a decrease in the deposition rate of about 10% was seen. For the sputtering process, the duration was 17 min during which substrate cooling was applied. For larger undercuts, the upper part of the resist bent down due to heating during the sputtering process, see Figure 3.7. Consequently, the lift-off result was not ideal. For larger undercuts, four breaks of 5 min each were introduced into the deposition process to counteract the resist bending.

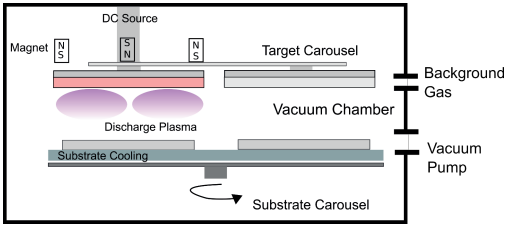

Figure 3.6. Schematics of working principle of the sputtering tool.

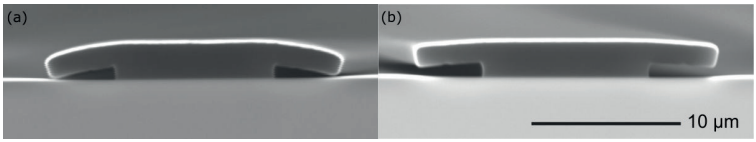

Figure 3.7. SEM images of sputtered samples coated with Ti-Pt (a) sputtering without pauses and bending of the photoresist layers and (b) after introducing pauses.

Thin nickel, platinum, and palladium films as metal additives were deposited on the MOX layers by DC magnetron sputtering using a Von Ardenne CS730S tool. Here, the silicon pieces with several chips—the so-called *reticles*—were put into the sputtering chamber and the substrate holders were rotated at constant speed in order to deposit very thin films homogeneously onto the substrates.

3.1.2. Deposition of metal oxide films by pulsed laser deposition

For deposition of MOX thin films with specific properties, PLD was used. The Piezoflare 800 from Solmates B.V. enables large-area deposition on 150 mm and 200 mm substrates [238, 239]. A picture of the tool is depicted in Figure 3.8. The wafers can be introduced by a load-lock in the tool and up to four targets can be mounted in the target carousel, providing the possibility to deposit layered films of different materials without breaking the vacuum. Figure 3.9 illustrates the schematic set-up of the tool. Here, the substrate is placed on top and in parallel to the target, the distance between target and substrate being several centimeters. The silicon wafer is installed upside down on a quartz chuck, which is rotated during deposition. The deposition is conducted using the automated software of the Piezoflare tool, which controls all deposition parameters such as process times, temperature, deposition pressure, heater voltage, rotations and

Figure 3.8. Picture of the Piezoflare 800 tool from Solmates including loadlock.

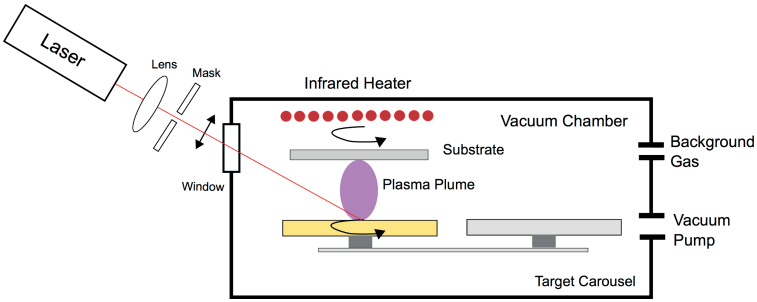

Figure 3.9. Schematic working principle of the PLD-tool.

laser parameters. Prior to deposition, the chamber is evacuated to a base pressure of about 0.05 Pa and the wafer is heated to the desired deposition temperature by an infrared heating source from the backside. The temperature can be controlled from close to room temperature up to 800 °C. Then the process gas, which is in most cases oxygen, is introduced into the deposition chamber and the pressure is controlled to the specified value in the range of p_{O_2}=0.5–20 Pa. It is also possible to conduct the deposition in nitrogen or argon. In order to achieve a homogeneous thickness distribution over the wafer, the target is rotated and the laser beam is scanned over the target at variable speed. A KrF ns excimer laser with a central wavelength of $\lambda = 248$ nm (Coherent Inc., pulse duration approx. 25 ns, power 80 W) is used. Repeated depositions—the so called traces—enable the thickness control, where one trace represents one scan to and from the center of the target. For influencing the deposition rate per trace, the pulse repetition rate can be adjusted in the range of 10–100 Hz, yielding a lower deposition rate for lower repetition rates.

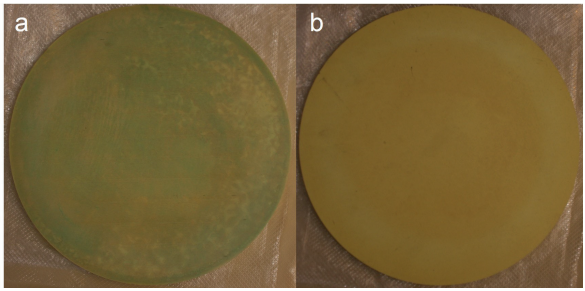

Figure 3.10. Exemplary pictures of as-received PLD targets (a) SnO_2 (b) In_2O_3. The diameter of the targets is 178 mm, the thickness 6 mm.

The target consists out of a sintered disk of the material to be deposited and is introduced into the chamber in a stainless-steel holder to provide a good backside heat sink. Targets and substrates used are roughly of the same size. Commercial targets of 178 mm diameter and 6 mm thickness were purchased; pictures of the tin oxide and indium oxide targets are shown in Figure 3.10. A crucial factor for the quality of PLD targets is their relative density which is calculated from the dimensions and the theoretical crystal density. A relative density of at least 80% is expected to ensure a low deposition of macroscopic particles on the substrates. In Table 3.1, the properties of the targets used in this work are summarized. In some cases, the relative density was lower than 80%. Here ablation tests were conducted to make sure that the PLD tool is not contaminated by particles. Optical micrographs of those tests are shown in Figure 3.11. It is seen that the roughness of the target is increased by application of ten laser pulses and the color is darkened due to a change in stoichiometry on the surface to a metal-rich phase [240]. However, no indication for exfoliation was found, which would lead to droplet formation. Prior to deposition, a preablation step was conducted to reach a steady-state of the target surface morphology, as the surface is altered by each deposition step [240]. An aperture (mask) was used to form a controlled deposition spot on the substrate with an approximate size of $2 \times 4\,\mathrm{mm}^2$.

3.1.3. Post-deposition heat treatment

For stabilization of the MOX films, they were annealed in humid synthetic air prior to the gas measurements, in order to simulate utilization conditions. This heat treatment was done over four hours in a high temperature furnace (Linn High-Term GmbH), where the samples were placed on quartz holders. In this

Table 3.1. Physical properties of the metal oxide targets used in this work. All targets except for ZnO (Praxair) and ITO (Unicore) were ordered by Evochem, first (f.d.) and second delivery (s.d.). The density is the relative density compared to the theoretical density of the bulk materia.

Material	Composition	Diameter/ mm	Thickness/ mm	Density/ %
tin oxide (f.d.)	SnO_2	178	6.1	37.3
tin oxide (s.d.)	SnO_2	178	6.0	83.6
tin oxide-palladium	SnO_2, 5% Pd	178	5.9	84.3
copper oxide	CuO	178	6.1	77.1
tungsten oxide	WO_3	178	6.1	77.6
indium oxide (f.d.)	In_2O_3	178	6.0	73.0
indium oxide (s.d.)	In_2O_3	178	6.2	61.6
zinc oxide	ZnO	178	6.3	98.1

furnace the temperature is controlled by Eurotherm controllers and the temperature measurement is done by two thermocouples which are installed in the oven center and the inner backside of the oven. Thermal treatments in this work were done in the temperature range between $400\,^{\circ}\mathrm{C}$ and $600\,^{\circ}\mathrm{C}$. The ramp-up time to reach $400\,^{\circ}\mathrm{C}$ was about 20 min and the cool-down time to $< 100\,^{\circ}\mathrm{C}$ was about 4 h. A constant flow of synthetic air (400 sccm) was supplied by an attached gas bottle and controlled by a MKS control unit. Humidity could be introduced into the annealing atmosphere by an evaporator (Bronkhorst High-Tech B.V.), applying 1 g/h H_2O. This flow rate was converted to the absolute humidity by the gas equation and converting volume flow of synthetic air F_{volume} to mass flow F_{mass}:

$$F_{\mathrm{mass}} = \rho_{\mathrm{air}} \cdot F_{\mathrm{volume}}, \tag{3.1}$$

$$\rho_{\mathrm{air}} = \frac{p}{R_{\mathrm{s}} \cdot T}, \tag{3.2}$$

where ρ_{air} the gas density, the ambient pressure being $p = 101.3\,\mathrm{kPa}$, the gas constant for air $R_{\mathrm{s}} = 287\,\frac{\mathrm{J}}{\mathrm{kgK}}$ and T the absolute temperature.

3.1.4. MOX structuring using silicon shadow masking

In the following to different shadow mask processes are described for shadow mask deposition 1) the Solmates PLD tool in this section and 2) the PLD tool at the Picodeon company in the following section. For the Solmates PLD tool a special silicon shadow mask process had to be developed.

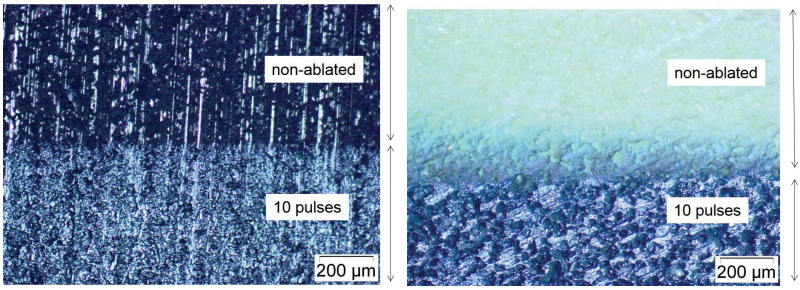

Figure 3.11. Micrographs (optical profiler Zeta-200, Zeta Instruments) of ablation tests on as-ordered CuO (a) and WO_3 (b) low-density PLD targets to determine the ablation behavior.

A shadow mask deposition process was developed in order to get a tool to structure various metal oxides without paying attention to their specific etching properties in e.g. halogen acids, which differ substantially from each other [241]. There were several challenges for the shadow mask processing: 1) the substrate is placed upside down in the chamber 2) the quartz wafer holder has a notch in the range of the wafer thickness and a conical shape 3) the wafer holder containing the substrate is rotated during deposition and 4) the substrate should be reliably and completely separated from the zone with the infrared lamps to avoid deposition of material on the lamps. To account for these issues, a silicon shadow mask was developed, which at the same time holds reticles from the wafer to be coated.

The shadow mask fabrication process flow is depicted in Figure 3.12. As a basis, 375 µm thick double side polished 150 mm wafers were used, which were thermally oxidized in order to get a total oxide thickness of 2.5 µm. Both sides were sequentially processed to obtain a structured silicon dioxide hard mask on both sides. They were coated with a positive photoresist with a thickness of about 7 µm and structured by using standard lithography. In the next step, the oxide was etched using a dry etch process. The photoresist was stripped in an oxygen plasma and the front side was trenched 150 µm deep using the Bosch deep reactive ion etching process [218]. The process wafer was bonded with the trenched side facing down to a carrier wafer of 375 µm thickness using a thin resist and a subsequent baking process on a hotplate. The back side was then trenched to a depth of 225 µm, resulting in through-holes in the shadow mask wafer. The wafer stack was separated, using acetone in an ultrasonic bath. The shadow masks have square cavities of 1.5 cm side length with recesses in

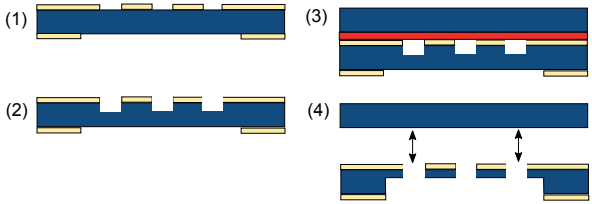

Figure 3.12. Schematics of shadow mask fabrication process: (1) Si-wafer with thermal oxide, dry etching of oxide on both sides. (2) Si-trench front side (approx. 150 µm) (3) Wafer bonded to carrier (4) Si-backside trench (approx. 225 µm) and separation of the two wafers. After Ref. [233].

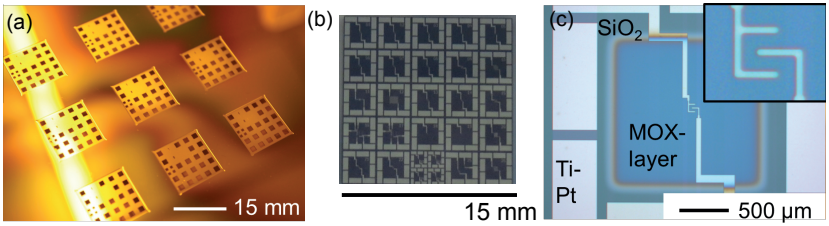

Figure 3.13. (a) Picture of shadow mask (b) picture of reticle (c) optical micrograph of resulting MOX film structured by shadow masking, inset shows magnified view of the central part.

the corners. A typical through-hole to the front of the wafer opening is a square with 1500 µm side length, a picture is shown in Figure 3.13 a.

To deposit structured MOX films by shadow masking, silicon reticles with Pt structures with lateral dimensions $1.5 \times 1.5\,\mathrm{cm}^2$ are inserted into the shadow mask with the Pt structures facing the through-holes and the through-holes fitting the reticle structures, as seen in Figure 3.13 b. The resulting structured MOX layer is larger than the interdigitated electrodes, but smaller than the contact area. This allows for contacting by either needle probes or wire bondings. An optical micrograph of a finished chip is depicted in Figure 3.13 c.

3.1.5. Structuring of Picodeon WO_3 films by shadow masking

The deposition of the WO_3 films took place at Picodeon company (Picodeon Ltd Oy, Finland). A picosecond (ps) laser PLD tool and a different kind of shadow mask setup was used. It comprises a steel shadow mask (thickness 50 µm) which is placed in an aluminum holder. An overview of the setup is shown in Figure 3.14 a and a picture of the holder in part b. The openings are

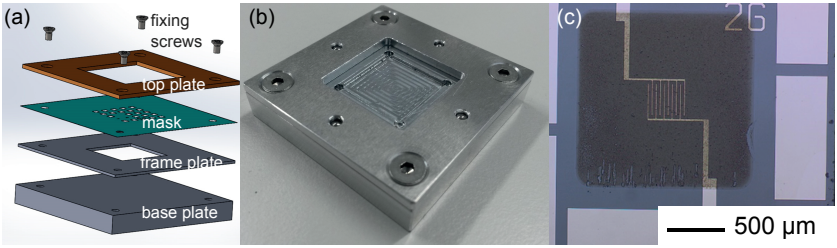

Figure 3.14. (a) Schematic shadow mask assembly. (b) Photo of shadow mask assembly without Si reticle and shadow mask. (c) Optical micrograph of Picodeon PLD WO_3 layer deposited on a silicon chip. After Ref. [242].

$1500 \times 1500\ \mu m^2$ in size. The resulting chip with a WO_3 layer is shown in Figure 3.14 c. The Picodeon WO_3 films deposited at above $p_{O_2} = 5$ Pa were very fragile. In consequence, a stealth dicing process was applied (DISCO Europe).

3.2. Electrical and Gas Characterization Techniques

3.2.1. Electrical measurements

Electrical characterization of the metal oxide thin films was done using electrical measurements on wafer level on the one hand and measurements of contacted structures on the other.

The wafer-level resistance measurements of MOX films were conducted using the four-point method. This method has the advantage of enabling measurements of the sheet resistance without structuring of the film [243]. Here, four probe tips are set with constant spacing on the substrate, as illustrated in Figure 3.15. Between the outer two contacts a constant current is applied and the voltage between the inner two is measured. Due to the separation of feeding and measurement contacts, the contact resistance is not influencing the measurement results. The sheet resistance $R_\square$ can be extracted from the measured voltage U and applied current I by the following equation for samples with large lateral dimensions in comparison to the distance between the probes:

$$R_\square = \frac{\pi}{\ln(2)} \cdot \frac{U}{I} \tag{3.3}$$

The resistivity ρ_r can be calculated from the sheet resistance, if the layer thickness d is known, by using the equation $\rho_r = R_\square \cdot d$. In this work, a Keithley current source and a nanovoltmeter were used for the four-point characterization at room temperature in a controlled environment (20 °C, 50% r.h.) under

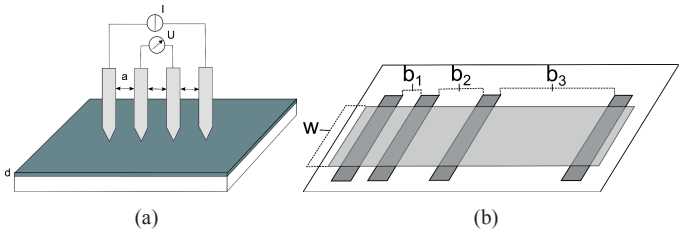

Figure 3.15. Schematics of (a) four-point-probe measurement (b) a linear TLM layout.

clean room conditions. The four-point probe was automatically positioned and scanned by using a custom-built system to measure up to 81 points over the wafer.

Samples with Pt interdigitated electrode structures were characterized by current-voltage (IV) measurements. These were conducted using a Keithley sourcemeter. For pre-characterization of metal oxides prior to gas measurements, the resistance of the MOX films contacted by Pt IDEs was measured at room temperature. The measurement range was set to ± 1 V and steps of 0.1 V were applied. The measurements were repeated five times in order to improve the measurement accuracy and check for drift effects. Interdigitated electrode structures of different aspect ratios were measured for the same MOX films to reveal an influence of the contacts to the resistance.

For investigation of the contact resistance, transmission line measurements (TLMs) can be employed. Typical geometries are either linear or circular TLM structures [244]. In this work, linear TLM structures were used for estimation of the relevance of the contact resistance [245, 246]. They can be fabricated—in contrast to circular TLM structures—without the deposition of contacts on top of the investigated material. However, for those structures the MOX layer has to be patterned to generate a defined geometry. This is illustrated in Figure 3.15 b and was done by shadow masking. The following formula describes the relationship between the total resistance R_{total}, the sheet resistance $R_{\square}$ and the contact resistance R_{contact}:

$$R_{\text{total}} = 2R_{\text{contact}} + \frac{b}{w} \cdot R_{\square}, \tag{3.4}$$

w being the width and b the distance between the stripes. If the resistance values are plotted versus the gap of the contact stripes and a linear fit is applied, the contact resistance can be estimated from the intercept and the sheet resistance from the slope of the resulting straight line.

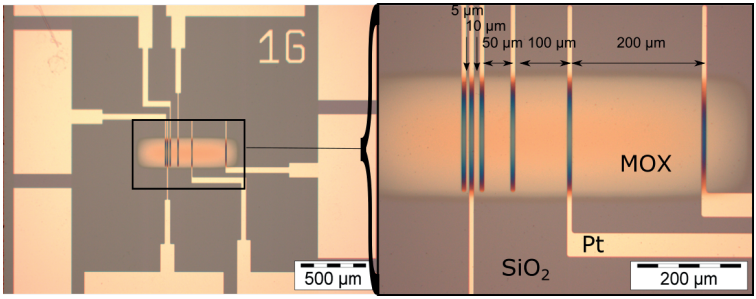

Figure 3.16. Microscope images of a TLM structure patterned by shadow masking. The left part shows an overview of the structure, the right part a detailed view of the Pt contact stripes.

The TLM structures were designed on the same chips as the interdigitated electrode structures, having the same Ti-Pt layers of 190 nm (total thickness) on 2.5 µm thermally grown silicon dioxide as an insulation layer on the silicon substrate. The MOX thin films were structured by slit-like openings in the shadow mask of approximately 200 µm and 400 µm width, see Figure 3.16. The distances between the 10 µm wide platinum contact stripes vary from 5 µm to 10 µm, 50 µm and 100 µm. Here, the sheet resistance cannot be determined precisely due to the shadowing effects of the shadow mask that lead to a transition zone at the edge. This transition zone was found to be about 150 µm; so the maximum thickness was not reached for the test stripes of 200 µm width. However, the results give a good indication about the importance of the contact resistance.

3.2.2. Electrical characterization of miniaturized hotplates

In addition to the thin film gas sensor chips comprising IDEs and sensitive films, miniaturized gas sensor chips featuring heated membranes, but having no gas sensitive layers were characterized. The aim was to investigate further miniaturization and reduction in the power consumption of the chips. Detailed results are provided in Ref. [247]. Test structures were analyzed to investigate the basic properties of the metallization of both heater and contact structure. These structures consisted out of stripes of a known length and width, and were deposited and structured in the same process step as the heaters and contact structures. Hence, they had the same film thickness as the metallization layers of the heater and the contact structure respectively. The chips were bonded to ceramic carriers and the resistance was measured by four-wire-sensing while heated to

temperatures in the range of 20–420 °C in steps of 50 K. The measurement current was of 0.1 mA to avoid self-heating. To characterize the relation between the temperature of the active area and power consumption, four-wire-sensing was applied to the membrane chips. The chips were, therefore, put on a chuck with a controlled temperature of 25 °C. Two needle probes were positioned on each contact of the miniaturized heater. A current of 0.1 mA was applied to determine the RT resistance, avoiding self-heating. In the following, 1 mA was applied and it was raised in steps of 1 mA up to a resulting voltage drop of 1.5 V. This was the case, dependent on the membrane size, between 14 mA and 20 mA. The values of the voltage were recorded for each current step. At higher values of the applied current, the voltage drop increased along with the temperature of the heater due to Joule heating.

3.2.3. Characterization of gas-sensing properties

The gas measurements were conducted using two different gas measurement systems and setups. One was installed at Bosch at location Schillerhöhe and later moved to the new location of research facilities in Renningen, while the other system used was situated at the University of Tübingen.

Bosch gas measurement system

For gas measurements at Bosch, an automatic gas-mixing system was used. A schema of the system is shown in Figure 3.17. The system was controlled by a LabVIEW software. Nitrogen was humidified by a bubbler containing deionized water. Dry nitrogen and oxygen were added to set a defined level of relative humidity in *synthetic air* (20% oxygen, 80% nitrogen). Gas bottles with different test gases such as nitrogen dioxide, carbon monoxide, ammonia, propylene, methane, hydrogen and carbon dioxide dissolved in nitrogen in various concentrations were dosed by mass flow controller (MFC) of the MKS-systems. The concentration range of the system was adjusted to typical test cases in consumer applications. The bottle concentration and the MFC sizes are shown in the schema of the setup. The total flow of the system is set to 1000 sccm. For measurements of two samples at the same time, the flow for each sample was adjusted to 500 sccm by separation valves and an additional mass flow meter (MFM). For carbon monoxide a concentration range of 5–50 ppm was used. For contacting the singulated or reticle chips, a simple setup was used without the need for mounting the substrates on heaters or headers. Therefore, the samples were placed as chips or reticles on an automatically controlled heated chuck of 8 cm in diameter and contacted by a probe head with needles. The gas was

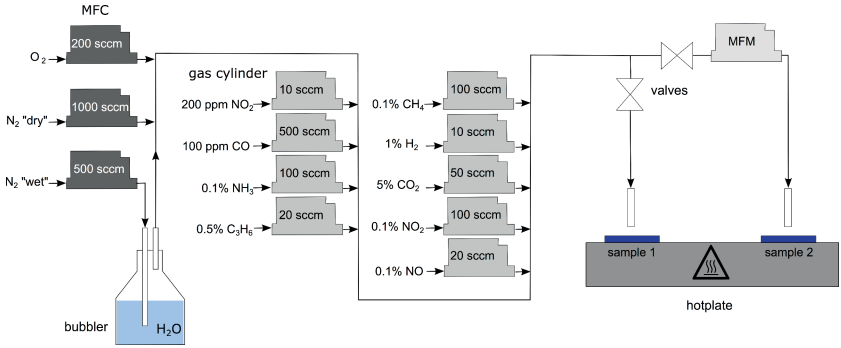

Figure 3.17. Schema of the MKS gas measurement set-up including a MFM. The electrical measurement system is not depicted in this schema.

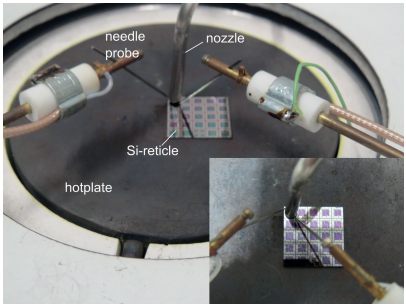

Figure 3.18. Picture of measurement setup using needle probes and gas nozzle to contact to a chip on a silicon reticle placed on a heated chuck. Inset shows top view of the central part.

dosed through a nozzle; a picture of the set-up is shown in Figure 3.17. A constant voltage in the range of 1–5 V was applied and the current was measured using a Keithley sourcemeter.

Sensor mounting

For measurements at the University of Tübingen, the sensor chips were mounted in TO-8 sockets. Commercial ceramic heaters (Pt-6.8, Delta-R GmbH) were bonded to the chips and fixed on heat-insulating elements consisting of structured glass on the sockets. The singulated chips were glued on the heaters and wire bonded. A computer-aided design drawing of the setup is shown in Figure 3.19 a. The dicing of the float glass into heat insulator sockets of $4.2 \times 2\,\mathrm{mm}^2$

footprint was done by WG Dicing GmbH & Co KG. These heat insulator sockets feature six columnar-shaped extensions of $0.5 \times 0.5\,\mathrm{mm}^2$ base area and 1 mm height. The glass socket was bonded to the TO-8 socket using a high-temperature die attach (MCT 136-VHT, MicroCoat Technologies). The same die attach was used to bond the heater to the glass socket and the chip to the heater. Curing was done in an oven for two hours at 150 °C. The silicon chips with the gas sensitive thin film were connected to the sockets by wire bonding (Au wire diameter 50 µm), and soldering was used to realize the electrical connection of the heater to pins of the socket.

For gas measurements, a gas-tight test chamber was constructed [248]. It comprised two pieces of polytetrafluorethylene (PTFE) (trade name *Teflon* by DuPont) and is shown in Figure 3.19 b. This synthetic material is especially suitable for gas measurement applications as it is chemically inert, shows a low permeability, and is stable at elevated temperatures. A disadvantage of the material is its low hardness compared to metals, which is why screw threads might wear out after frequent usage. To solve this problem the plastic parts were placed on a stainless-steel base plate and fixed on top by a stainless-steel cap. In the picture, the test chamber is opened so that the setting of three sensors inside can be seen. The chamber lid is tightly sealed by an O-ring and electrical connections to the outside are done by IC socket pins fitted in the chamber lid. The pins are connected to the voltage supply and measurement instruments by custom-made cables. Up to eight sensors can be placed in the chamber and measured at the same time. The chamber is connected to the gas feedthrough and the exhaust by plastic tubes, which are connected tightly to the chamber by Swagelok connectors.

Gas measurement system at the University of Tübingen

The measurements at the University of Tübingen at the Institute of Physical and Theoretical Chemistry, AG Weimar, were also conducted using a computer-controlled automated gas measurement system. Here test gas bottles of CO and NO_2 in synthetic air were used and mixed with humidified synthetic air. The degree of humidity is controlled by dosing of 100% r.h. synthetic air which was humidified by a bubbler. Automatic valves were installed to prevent gas flow back to the system. Details of the measurement systems can be found in recent publications of the Weimar group, e.g. [249].

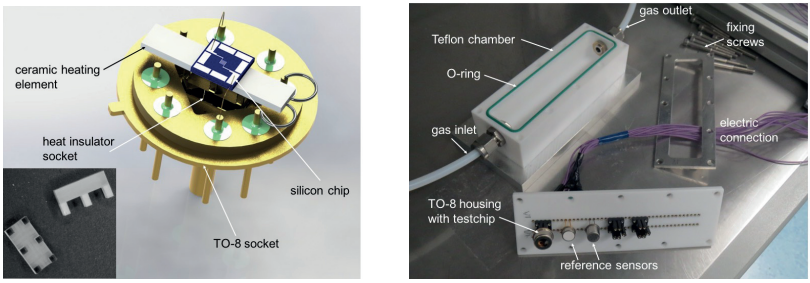

(a) (b)

Figure 3.19. (a) Schematic of the sensor mounting on a TO-8 socket for measurement in a gas-tight chamber, inset shows photo of glass heat insulator elements. (b) Picture of measurement chamber set-up including mounted test chip and reference sensors. The part containing the sensors is placed upside down on the measurement chamber and fixed using screws.

3.3. Physical and Chemical Characterization

Morphological properties of the deposited metal oxide thin films were revealed by structural characterization on as-deposited and heat-treated samples. For this purpose, wafer-level-deposited metal oxide films were characterized. Optical microscopy, a Hitachi tabletop scanning electron microscope and surface profilometry (Tencor and Dektak) were used for process control inside the clean room. For the investigation of the metal-electrode structures and metal oxide films, scanning electron microscopy and optical microscopy were used.

3.3.1. Scanning electron microscopy

Scanning electron microscopy (SEM) is an established characterization technique for topographic investigation of micron- and submicron-sized features. It is based on the deflection of a collimated electron beam that is scanned over the sample placed in an evacuated test chamber. Different signals from backscattered and secondary electrons can be recorded and give insights into the morphology of the samples. Additionally, the characteristic X-rays emitted by the electron excitation can be analyzed in order to get information about the material composition. For the characterization by SEM, the silicon wafers were cleaved to small pieces of maximum $1 \times 1\,\mathrm{cm}^2$ and placed into the sample holders, either horizontally for top view, or vertically for cross-sectional SEMs. In order to minimize the surface charging of the layers, a few nanometer thin Pt-Pd

film was sputtered on top. For most of the measurements, a Leo Gemini 1630 SEM at 3 kV operation voltage in the secondary-electron-mode was used.

3.3.2. Transmission electron microscopy

As the topographic features of the thin film morphology were at the resolution limit of the SEM, transmission electron microscopic (TEM) investigations were conducted additionally at the Technical University of Ilmenau [250]. The samples for TEM investigation were prepared by a focused ion beam using a Zeiss FIB Auriga 60. The TEM analysis was done using a FEI TEM Tecnai 20S-Twin.

3.3.3. X-Ray diffraction

X-ray diffraction (XRD) is a non-destructive technique enabling the determination of material properties such as crystal structure, orientation, microstress and material composition [251]. The measurement principle is based on Bragg's law, which describes the case of constructive interference of radiation reflected in a crystal:

$$2d_{\text{lat}} \sin \theta_{\text{inc}} = n\lambda, \tag{3.5}$$

where d_{lat} is the distance of the crystalline planes, θ_{inc} the angle of incidence of the applied radiation, and n is an integer. If X-ray radiation is applied, the wavelength λ is in the same order of magnitude as d_{lat}.

Both crystallinity and crystal orientation of the metal oxide materials were studied by XRD using a Bruker D8 Advance DAVINCI diffractometer. Cu-Kα-rays were applied and measured using Bragg-Brentano optics. The data were evaluated using the JCPDS database. In this setup, it was not possible to determine the crystallite size due to low signals of the thin films and anisotropic peak broadening. Additionally, the disturbance by the background from the silicon wafer substrate was high. Therefore, the crystalline structure of the metal oxide thin films was studied in more detail by gracing incidence XRD at the Technical University of Ilmenau [250].

3.3.4. X-Ray photoelectron spectroscopy

X-ray Photoelectron Spectroscopy (XPS) is a highly surface-sensitive spectroscopic technique that gives information about e.g. chemical binding states and the composition of materials. It is based on the photoelectric effect: Bound electrons are excited by the incident electromagnetic radiation and the emitted electrons are analyzed energetically. XPS was used in order to get insights

into the surface properties of metal oxide films by means of a Quantera SXN X-ray photoelectrometer from Physical Electronics GmbH. The electron spectroscopy for chemical analysis of this system detects information of the upper 5 nm of the sample. Monochromatic Al K α-rays were used and the diameter of the analyzed area was 200 µm. Furthermore, the samples were electrically connected within the spectrometer to create a defined potential, which enables the determination of the work function of the investigated material [252]. Depth profiles were created by sequential material removal using Ar sputtering in steps of about 8 nm. The XPS method was also used to investigate the diffusion of the Pd surface additive into the SnO_2 sensing layer.

4. Lift-Off of IDEs with Defined Edge Angles

In this chapter, the interdigitated electrode structures for contacting the thin-film MOX are investigated. The resist structure plays a significant role in the resulting geometry of the metal edges. The process is simulated by iterative calculations, and the results are compared with those of the experimental measurements. Large parts of this chapter were published in [234].

4.1. Simulation and Modeling

For bottom contacts with the thin films, the interdigitated electrodes (IDEs), consisting out of platinum with titanium adhesion promoter, were structured by bi-layer lift-off, as described in Section 3.1.1. In order to obtain design rules for the fabrication of IDEs with smoothly tapered edges, a process simulation was conducted. Herein, iterative calculations were performed, following the model reported by Tisone and Bindell [253] for calculation of the step coverage of metallization over structured films. This is based on a simple geometric model and models the sputtering rate by means of the effective solid angle of the aperture, assuming linear trajectories of sputtered particles. This geometric assumption is frequently used for calculating film thicknesses in deposition processes and it was found to be in good agreement with the experimental results [228, 254, 255]. As the mean free path in the applied pressure range is much higher than the resist thickness, collisions of sputtered atoms among each other and within the holes can be neglected. As the substrate is cooled during the deposition, we assume surface diffusion to be negligible in our model, so the sticking coefficient of the surface is set equal to one. For the deposition geometry, we assume a parallel geometry of substrate and target. The source is supposed to have a cosine distribution with the angle with respect to the surface normal. Therefore, the intensity of emission in a given direction is proportional to the projected area of the source in this direction [256–258]. This should be a valid approximation in our case of low pressure sputtering [253]. We additionally assume a homogeneous source without a radial distribution of the emission. The flux from the target at point P is described by the following equation:

$$J(\alpha_1) = \int_{A_S} k \, \frac{\mathbf{r}}{|\mathbf{r}|} \, \cos\alpha_1 / R^2 \mathrm{d}A_S, \tag{4.1}$$

where J is the atomic flux in the direction of $\mathbf{r}$, k is a scaling factor dependent on the sputtering rate, α_1 is the angle of the deposition flux seen by the surface and R is the distance to the source element. For deposition into a resist profile there is an effective source surface seen by the point P named A_S. This surface is determined by the following limits [225, 253]:

1. geometry - limited by the lateral dimensions of the target
2. slope shadowing - limited by the aperture of the resist structure
3. self-shadowing - limited by the growing layer

Cartesian coordinates are used to model the growth of the films, and the edge of the step is set parallel to the y-axis. The resulting surface of the deposited film on the resist structure is expressed by paired coordinates $P_\mathrm{i}(x_\mathrm{i}, z_\mathrm{i})$. The calculated thickness change of the layer t_i (Figure 4.1 a) is expressed as changes of Δx and Δz, which result from the following equations [259]:

$$\Delta x = k^* \int_{A_\mathrm{S}} \frac{D(x - x_i)}{R^4} \mathrm{dx\,dy}, \tag{4.2}$$

$$\Delta z = k^* \int_{A_\mathrm{S}} \frac{D^2}{R^4} \mathrm{dx\,dy}, \tag{4.3}$$

where D is the target-to-substrate distance and $\cos\alpha_1$ is substituted by D/R and k^* is a scaling factor. Δy is not considered as it is not influenced by shadowing. As in the case of micrometer scale features, there is $|x_i| \ll T$, where T is the radius of the target, and as only structures in the center are investigated, P is considered centered. For calculation of Equation 4.2 and 4.3, we set $R^2 = (x - x_i)^2 + y^2 + D^2$ assuming $z \ll D$. The integration limits are calculated iteratively considering the effective surface change of the target, expressed by the limits of the surface angles β as shown in Figure 4.1 b. These angles have values in the range of the geometric limits $\beta_\mathrm{geo1} = \arctan(D/T)$ and $\beta_\mathrm{geo2} = \pi - \arctan(D/T)$. The angular limits of the aperture are then found by numerically calculating the maximum slope to all points to the left and the minimum slope to all points on the right of point P. If these values are smaller than β_geo1 or larger than β_geo2, they are substituted by the geometric limits. For Equations 4.2 and 4.3 the limits are seen as effective target dimensions in x-direction $x_\mathrm{limit} = -D/\tan\beta$ for $\beta < 90°$ and $x_\mathrm{limit} = D\tan(\beta - \pi/2)$ for $\beta > 90°$. The limits in y-direction are found by the target radius T as $y_\mathrm{limit} = \pm\sqrt{T^2 - x^2}$. After adding a certain layer thickness t_i ($x_i' = x_i + \Delta x, z_i' = z_i + \Delta z$) the integration limits are recalculated, considering the changes in the surface inclination γ and the aperture (Figure 4.1 a).

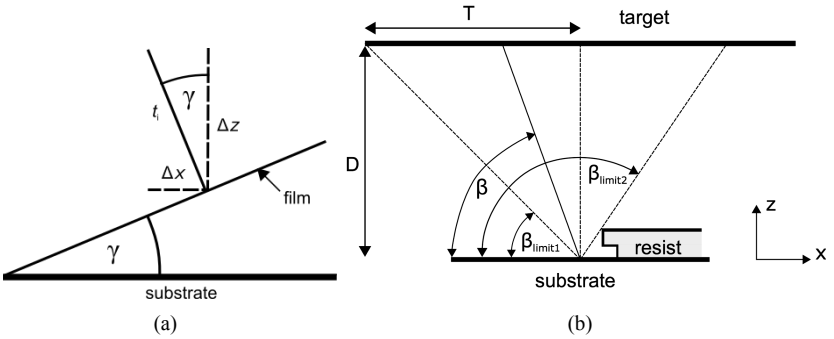

Figure 4.1. Schematic drawing of (a) the inclination of the surface of the growing layer and (b) the substrate and target geometry. The integration limits β_{limit1} and β_{limit2}, and the sputter angle β are marked. The edge of the step in the resist is parallel to the y-axis. After Ref. [234].

Smooth edge structures were found in the case of high resist thicknesses. An exemplary result is shown in Figure 4.2. For all simulations, negative flanks for the LOR are assumed (38° with respect to the perpendicular), which was found as an experimental result from the image reversal negative resist structure. In contrast, the lower LOR flank was set as perpendicular to the surface in the simulations. If we calculate the profile for a substrate without rotation and with the resist opening placed laterally close to the edge of the target, we get a very asymmetric profile result, due to the different effective source areas of the target to the left and to the right side of the profile, see Figure 4.3 a. Additionally, the deposition rate is lower at the edge. Substrates are rotated during the deposition process in the experimental setup to avoid this nonuniformity of the metal thickness. Rotation of the substrate is simulated by changing the x_i value of the points P_i from $-T$ to $+T$, adding $2T/n_I$, if n_I is the number of iterations. The resulting deposition profile is shown in Figure 4.3 b for 100 iteration steps. In the following, the target rotation is not further considered, as the resulting thickness profile of the layer is very similar to the simulation result of a resist structure at the center of a static substrate [259].

4.2. Experimental Results and Discussion

In order to determine the influence of the resist profile on the resulting metallization profile, three parameters of the bi-layer resist structure were varied:

1. the thickness of the LOR h_1

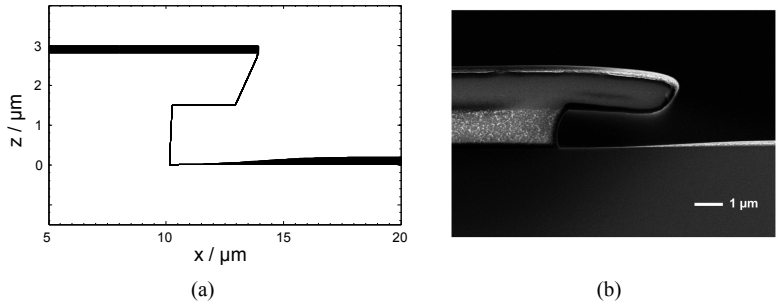

Figure 4.2. (a) Example of a sputtering simulation after 26 iteration steps using a bi-layer resist with LOR thickness of 1.5 µm. (b) resist structure depicted as SEM image. After Ref. [234].

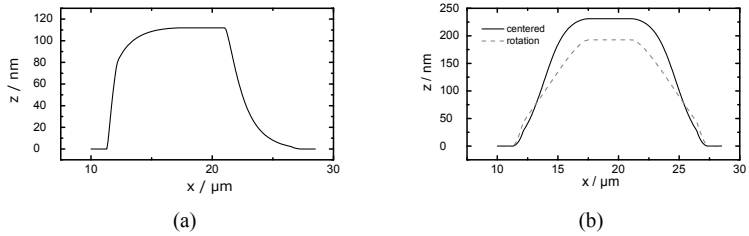

Figure 4.3. (a) Calculation of the deposited layer profile if the resist structure is placed in x-direction close to the edge of the source. The center is on the left side of the graph. (b) Comparison of calculated deposition for a centered position of the resist structure if the substrate is placed centered (solid) or substrate rotation is activated (dashed). After Ref. [234].

2. the undercut length v

3. the target-to-substrate distance D

The thickness of the upper resist layer was designated h_2. To determine the thickness profiles, both the lithography width w_1 and the width of the metal line after lift-off w_2 were measured. The parameter definitions are shown in Figure 4.4. From these figures, the under-sputtering lengths u was calculated as $u = \frac{1}{2} \cdot (w_2 - w_1)$. Here lines with mask-openings of 10 µm, 12 µm, 20 µm were used for the investigation.

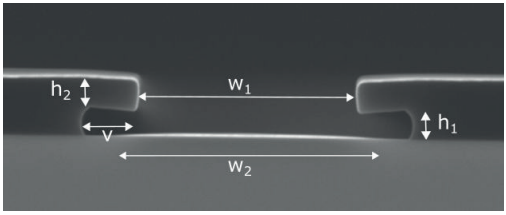

Figure 4.4. Illustration of lithographic parameters of the as-sputtered lift-off structure, SEM image. After Ref. [234].

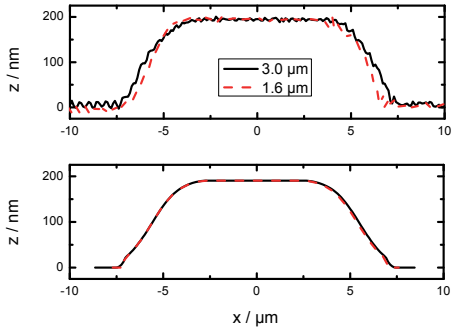

Figure 4.5. Comparison of metal structure thickness profiles for two undercut lengths 1.6 µm and 3.0 µm. A LOR of h_1=500 nm thickness was used. Upper image shows measurement and lower image contains simulation results. After Ref. [234].

4.2.1. Variation of the undercut length

Variation of the development time resulted in different undercut lengths, as discussed in Section 3.1.1. To balance small variations of the sputtering rate over the wafer, the maximum thickness of the metal structure was always normalized to 190 nm, when comparing the metallization profiles. This also allowed for a better comparison of experimental and simulation results. Both profilometer and SEM measurements confirmed that the full layer thickness was reached in the center of the lift-off structures in all investigated cases. Figure 4.5 compares simulations and experiments for two different undercut lengths. Both experimental and simulation results showed that thin LORs with thicknesses below 500 nm do not allow changing the metal deposition profile by a variation of the undercut length for metal lift-off structures.

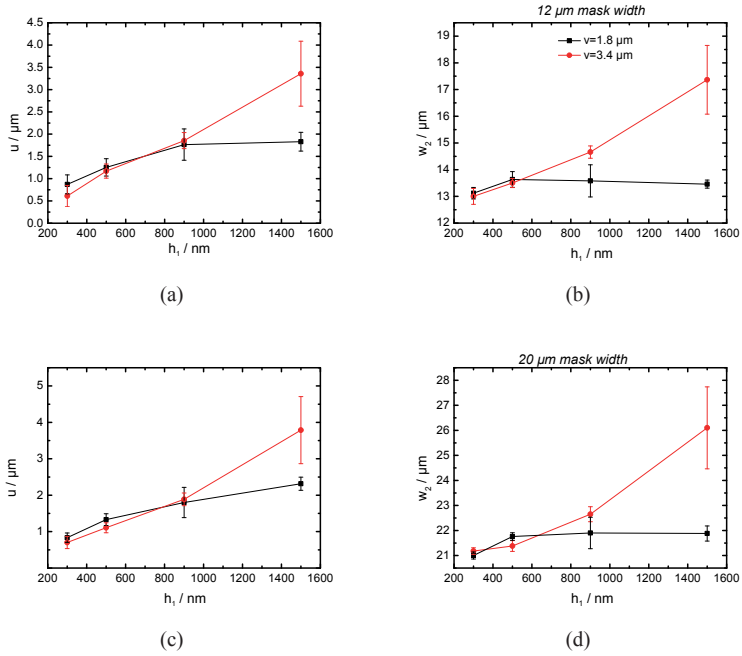

Figure 4.6. (a) Dependence of the under-sputtering length u and the metal line width after lift-off w_2 on the LOR thickness for two different undercut lengths. Two different mask opening were investigated: 12 µm (a and b) and 20 µm (c and d). After Ref. [234].

4.2.2. Variation of the resist thickness

The thickness of the LOR was varied by changing the spin-on speed and by choosing resists with different viscosities, while the thickness of the photostructurable resist was kept constant at 1.3 µm. The effect of the under-sputtering of the upper resist and the tapering of the metal layer was investigated. Two different undercut lengths were chosen for this investigation, namely 1.8 µm and 3.4 µm. Thicker LORs led to higher metal line width because of higher under-sputtering of the resist, see Figure 4.6. If we compare both lines in each graph, it also becomes clear that the metal line widths do not depend on the undercut length for thin LORs, as stated in the previous paragraph. This is due to the limited geometric range of sputtering angles that affect the layer deposition.

The profile of the metal edges was investigated by SEM images after the cleaving of the samples, see Figure 4.7. Different LOR thicknesses were used

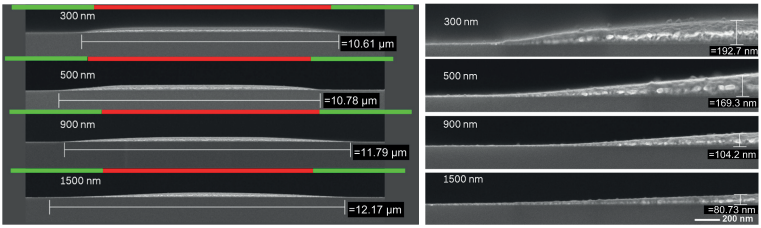

(a) (b)

Figure 4.7. SEM images after wafer cleaving of Ti-Pt structure after lift-off. Different LOR thicknesses were used as indicated in the images, see text. After Ref [234].

(300 nm, 500 nm, 900 nm, 1500 nm), and the undercut length was kept constant at about 3.4 µm. The green and red lines indicate the undercut length v and the lithographic line width w_1, as determined by optical microscopy. (b) Shows a magnified view of the left part of (a). These results reveal that the profile edges are smoother for thicker LORs, so these are more appropriate for applications such as fabrication of thin-film IDEs.

Profilometer measurements of the metal layer thickness showed the same trends and very similar quantitative results. Higher LOR thicknesses were proven to result in higher under-sputtering lengths and smoother profiles. The simulated metal profiles correspond well with the measured profile as can be seen from Figure 4.8. The under-sputtering lengths were calculated and compareded with the values measured by optical microscopy, see Figure 4.9. The undercut lengths were thus determined by optical microscopy and these individual values were used for the simulation of each sample. The under-sputtering length u was extracted for the simulations between the maximum thickness of the metal line and the position where the thickness was 10% of the maximum thickness. A clear trend is seen, showing an increase in u with increased resist thickness in both experimental and simulation results. For the structures with $v \approx 1.8\,\mu\text{m}$ we see the same trend as for $v \approx 3.4\,\mu\text{m}$ for the lower resist thicknesses. In the case of $h_1 \leq 900\,\text{nm}$, under-sputtering is limited by the undercut length and no influence of the resist thickness on the under-sputtering is seen for the lower undercut lengths. We also find some deviation between the measured and the calculated values. The experimental method of determining the under-sputtering length by optical microscopy limits the achievable precision. The visibility of tapered edges depends on illumination and is not clearly defined. This leads to a small variation between measurements, which cannot be easily given or calculated. However, simulation and experiment show the

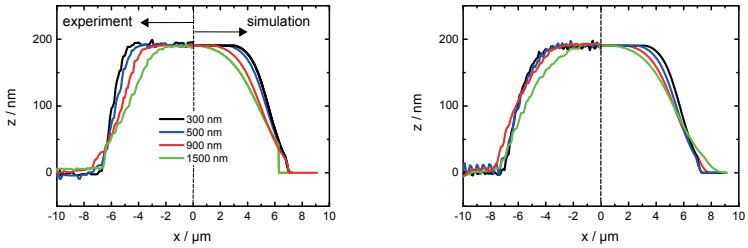

Figure 4.8. Profilometer measurements (left part of both graphs) and simulations (right part of both graphs) of the thickness profile of a structure of 10 µm in resist opening width. Graphs showing the experimental results were subsequently smoothened by Savitzky-Golay algorithm to reduce noise from the profilometer. Two undercut lengths were investigated, which were about 1.8 µm (a) and about 3.4 µm (b). After Ref. [234].

same trends. Within the given deviations in the measurements, the simulations allow a good estimation of the under-sputtering length for a given parameter set.

4.2.3. Variation of the target-to-substrate distance

In order to investigate the influence of the deposition geometry on the result of the metallization profile, the distance between the target and the substrate was varied. Hence, two different distances were used, namely 60 mm and 90 mm. Simulations resulted in a rather large decrease in the deposition rate (25%), if the target-to-substrate distance is increased. The actual deposition rate change measured was of only 10%. This discrepancy is most likely due to the simulation model, which does not consider changes and the resulting effects in the target ablation geometry due to different electrode configuration. The model does only account for geometrical effects of the deposition. Figure 4.10 illustrates the thickness profile according to experimental and simulation results. The simulation values were normalized to a total thickness of 190 nm. An increased target-to-substrate distance decreases the angular range for possible shadowing. The edges for 90 mm distance are not as smoothly tapered as for 60 mm. Compared to the results achieved with different resist profiles, this effect is not very pronounced. Consequently, as a process design rule, if different metal geometries can be reached by the resist profile, there is no necessity to change the deposition geometry.

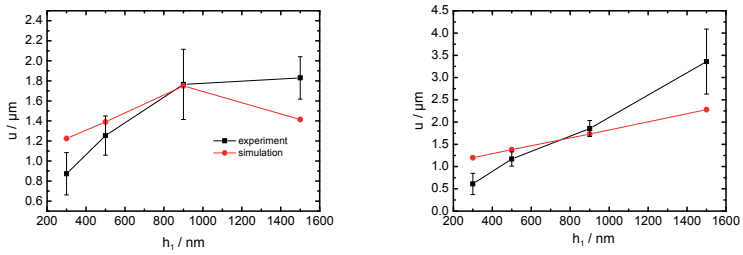

Figure 4.9. Comparison of under-sputtering length u for measurements and simulations. Two different undercut lengths were used, about 1.8 µm (a) and about 3.4 µm (b). After Ref. [234].

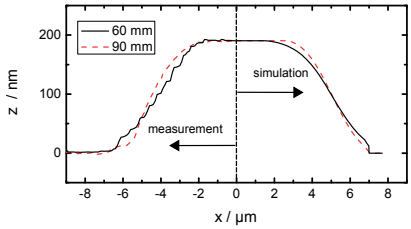

Figure 4.10. Measurement (left) and simulation (right) of the edge profiles for two different target-to-substrate distances (60 mm and 90 mm), lower resist thickness $h_1 = 900$ nm, undercut length $v = 1.8$ µm. After Ref. [234].

The model can be further improved if a radial dependence of the target erosion rate caused by the magnetron sputtering source is considered [255, 260]. In the present case, we could not investigate the *target erosion groove* which appears after prolonged deposition. Additionally the applicability of the cosine distribution should be proven. Different studies found a more complex function $\cos^b \alpha_1$, with the parameter b being determined empirically. These show better consistence with experimental results [255, 257, 259].

4.2.4. Deposition of additional thin films on structured electrodes

As a first proof of concept, SiO_2 was deposited on a substrate with smooth electrode edges. A well-known material was chosen as a reference, deposited by a plasma enhanced chemical vapor deposition (PECVD) process. The layer

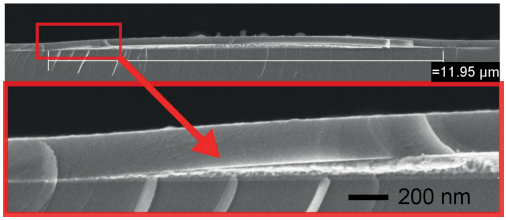

Figure 4.11. SEM images showing a 220 nm thick PECVD oxide deposited on an approx. 190 nm thick metal layer that was structured by lift-off. The lower image is a magnification of the left part of the upper image. After Ref. [234].

showed good adhesion on the metal film at the edges of the metal structures with neither cracks nor film tear-off (see Figure 4.11). In the following 30–300 nm thick metal oxide layers were deposited as sensitive layers. The as-described structured metal electrodes were used as electrical contacts to the semiconducting layers.

4.3. Conclusions

A method to fabricate platinum structures with ultra-smooth edges and a respective simulation tool were demonstrated. The lift-off process uses a bi-layer resist. Parameters of the lift-off resist at the bottom were varied, and the resulting structured Ti-Pt thin films were analyzed. DC magnetron sputtered metal films patterned by this process showed ultra-smooth edges, and were good candidates for creating contacts to thin film metal oxide layers for miniaturized gas sensors. The profiles of the processed structures were investigated by SEM and surface profilometry. The thickness profile and structure width could be adjusted by using different resist thicknesses and undercut lengths. Important parameters such as the line width of the deposited metal layer and inclination of the edges of the metal lines could be modeled using iterative calculations based on a geometric shadowing model. The consistency between experiment and simulation could be shown for a variation of several parameters. The model used for calculation is versatile and can be applied for step coverage or shadow mask deposition process simulations. First experiments for a multi-layer arrangement showed a very high conformity of a PECVD oxide coating. Thin films deposited on the interdigitated electrode structures using this process show good adhesion. Thus, metallization structured by this process seemed applicable as bottom contacts to metal oxide thin films and was further used in this thesis.

5. SnO_2 Films Prepared by PLD

As SnO_2 is the most important MOX in commercial CO sensors, a special focus is set on this material in this work. Here, thin films prepared by PLD are evaluated. WO_3 as an alternative material is discussed in the following chapter. Results of other alternative materials prepared by PLD can be found in Appendix B. First, electrical and morphological properties of SnO_2-based PLD thin films are evaluated. As-deposited and annealed, as well as samples with Pt contacts, are investigated by wafer-level measurements. Moreover, the gas-sensing properties of the chips and mounted samples are discussed. Parts of this chapter were published in [261].

5.1. Electrical Properties

Electrical properties are a good measure for the film quality, as the resistivity depends on both the stoichiometry and the crystallinity of the thin films [233]. Four-point-probe measurements were conducted and additional measurements were done using contacted samples in order to determine the influence of the contact resistance.

5.1.1. Influence of the deposition temperature

PLD films were prepared with a variation of the deposition temperature T_{dep} from room temperature (RT) to 600 °C. All films were deposited at 10 Pa oxygen background pressure for this investigation. The resistance was characterized by four-point-probe measurements under clean room conditions at RT, and I-V-curves of contacted samples were recorded.

In Figure 5.1, the resistivity of the films as a function of deposition temperature is depicted, as calculated from film thickness and sheet resistance measurements. Mean values of 81 measurement points are shown. The error bars represent the standard deviations over the 150 mm wafer. The resistivity clearly decreases with increasing substrate temperatures up to 300 °C. This tendency can most likely be explained by an increasing crystallinity of the films [181] due to higher surface mobility at higher temperatures. For even higher temperatures above 300 °C, a decrease in sheet resistance can be observed. Here, we expect that this effect bis due to a better stoichiometry because of increased

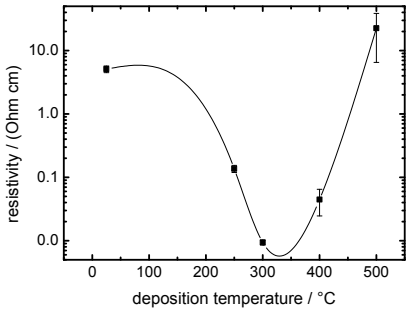

Figure 5.1. Resistivity versus temperature, determined by four-point-probe measurements at RT. The deposition pressure was kept constant at 10 Pa. The line serves as a guide to the eyes only. After Ref. [261].

oxygen incorporation in the layer. As oxygen vacancies represent donors in tin dioxide [21, 27, 28, 91], this results in n-type conduction as the main conduction mechanism in the medium temperature range below 400 °C [21]. Thus, the resistivity of SnO_2 is highly influenced by the oxygen content in the layer. Changes in resistivity over several orders of magnitude are reported [28]. However, temperature-induced stress resulting in defects might also contribute to the higher resistance of the films for the high-temperature deposition. In the following, 300 °C was chosen as deposition temperature in order to get SnO_2 films of a good quality.

5.1.2. Influence of the deposition pressure

For studying the influence of the deposition oxygen pressure to the electrical properties, PLD films deposited at 300 °C were investigated. Therefore, the deposition pressure was varied in the range of 1–20 Pa, and the resistance was characterized by four-point-probe measurements under clean room conditions and *I–V*-curves of contacted samples. The resistivity was calculated from the sheet resistance and thickness of the layers.

Results from the wafer-level electrical characterization of depositions conducted at 300 °C are depicted in Figure 5.2 a. Here, the wafer-level results of 81 measurement points are summarized. The error bars indicate the standard deviation over a single wafer. From the results, a clear tendency was seen that the resistivity increases with increasing deposition pressure. This can be explained by increased oxygen incorporation in the layer. Higher background

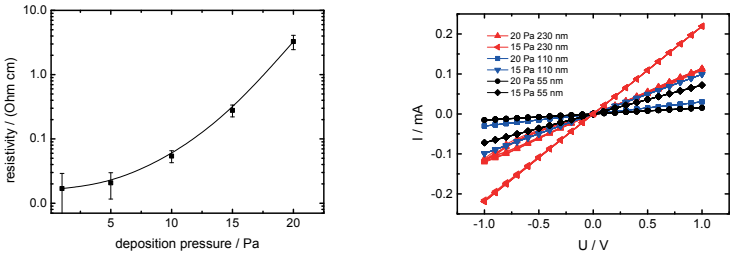

Figure 5.2. (a) Resistivity determined by four-point-probe measurements versus deposition pressure, all depositions were conducted at 300 °C. Measurements took place at RT. (b) *I–V*-curves measured at RT are shown for different thicknesses of the PLD layers and two different deposition pressures. After Ref. [261].

pressure also leads to a larger interaction of the ambient gas with the plasma plume, which can result in a change in the layer morphology. This morphological change, which is discussed in the following section, might also introduce changes in the electrical properties.

Additionally, *I–V*-curves of samples deposited at 15 Pa and 20 Pa with Pt-contacts were investigated. The *I–V*-plots exhibit linear characteristics in the range of ±1 V, indicating ohmic contacts. This measurement range was chosen as the measurement voltage was not set above 1 V in the application. The same tendency is seen here, showing a higher resistance of the samples prepared at higher pressure (15 Pa vs. 20 Pa), see Figure 5.2 b. Furthermore the investigation of films with different thicknesses (55 nm, 110 nm, 230 nm) shows that the resistance directly increases for thinner films, which is another indication for ohmic contacts.

5.1.3. Conclusions

It has been demonstrated that SnO_2 thin films can be prepared with good wafer-level homogeneity regarding the resistance measured at RT. The room temperature resistivity increases with increasing deposition pressure. This is most likely due to a better stoichiometry of the layers due to increased oxygen input during deposition and an increase in grain-grain contact barriers. To distinguish between those two effects, physical and chemical investigations of the materials are helpful. Hall measurements would also help to better distinguish between

influence of the stoichiometry and morphology [262]. However, Hall measurements were prepared, but could not be conducted in the frame of this thesis.

5.2. Morphological Properties

The gas-sensing behavior of MOX films does not only depend on the kind of material used. The design of the morphology is a key parameter for high response [263] as it affects the importance of the depletion-dominated region at the grain boundaries that is accessible to gases, as discussed in Section 2.1.11. For compact films, where the gas interaction takes place only on the surface, a lower response is expected than for porous films with gas-accessible grain-grain contacts. In contrast to wet chemically processed MOX films, thin films usually show a rather dense morphology. In the following section, the morphological properties of PL-deposited SnO_2 films are investigated.

5.2.1. Influence of the deposition temperature

To investigate the influence of the deposition temperature on the morphological properties, SEM images of cross-cut wafers with PLD thin films were investigated. All of them were deposited at 10 Pa oxygen background pressure and without post-deposition heat treatment. In addition, GIXRD was done on the samples at TU Ilmenau to determine the crystallite size.

For preparations at a deposition temperature of 250 °C, the microstructure is fibrous and no crystallites can be distinguished in the SEM, see Figure 5.3 on the very left. Possibly the layer is not fully crystalline but partly amorphous. For the deposition at 300 °C, a denser morphology is achieved, showing first indications of columnar growth. For the deposition at 400 °C, the columnar structure becomes clearer from the SEM image. The lateral size of the grains is in the range of 10 nm. A dense structure is finally formed for the case of the 500 °C-deposition with columnar grains of lateral sizes in the range of 10–20 nm. The grains do not extend through the whole thickness of the layer. Considering the crystallite size determined by GIXRD (see Table 5.1), it is seen that the as-deposited films are nanocrystalline for the deposition temperature range of 250–500 °C. There is a tendency to larger grain sizes for the higher deposition temperatures. At 500 °C, a crystallite size of 20 nm is found, whereas for the deposition at 250 °C, the crystallite size is 12 nm. Annealed films deposited at RT have a grain size of 9 nm.

The growth behavior is partly explained by the Thornton model, which was introduced in Section 2.4.2. In Figure 5.3, an illustration of this model has been added. As the melting temperature of SnO_2 is $T_m = 1630\,°C = 1903\,K$, we find

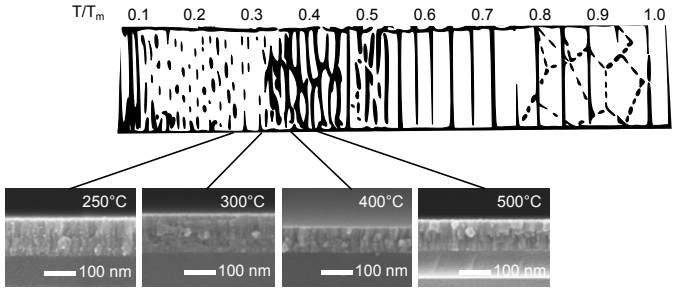

Figure 5.3. Application of the Thornton model on SnO_2 PLD layers. All depositions took place at 10 Pa oxygen pressure, deposition temperature as indicated in the image.

Table 5.1. Crystallite size determined by GIXRD at TU Ilmenau. Deposition took place at 10 Pa oxygen pressure. Annealing was done at 400 °C for four hours in humid air.

Deposition T/ °C	Anneal	Crystallite size/ nm
RT	yes	8.5
250	no	11.6
300	yes	7.2
400	no	11.6
400	yes	13.8
500	no	20.4

the boundary line between zone 1 and zone 2 at $0.3\,T_\mathrm{m} = 300\,°\mathrm{C}$. In this range, the microstructure changes from highly defective to columnar and dense. When we compare the SEM images with the illustration, it becomes clear that the pressure-dependent morphology is obviously close to the one of sputtered films with an equivalent pressure of 0.13 Pa. The high energy of the PLD process leads to a deposition of dense films at higher pressures than expected for sputter deposition in argon background, according to the Thornton model. This is in line with the results of previous studies, e.g. [92], compare Section 2.4.3.

5.2.2. Influence of the deposition pressure

For the investigation of the influence of the deposition pressure to the morphological properties of the PLD thin films, films with thicknesses in the range of

about 120 nm were prepared at various pressures in the range of 1–20 Pa. The morphological investigation was conducted by SEM, TEM, and XRD.

As demonstrated in Figure 5.4 a the morphological appearance of the thin films clearly changes with the applied oxygen pressure during deposition. For the deposition at the lowest possible pressure of our tool, being 1 Pa, the film appears dense and no crystallites can be defined. For the deposition at 5 Pa the film appears compact and dense. A brittle structure with apparent crystallites is found for the case of the deposition at 10 Pa. For even higher deposition pressures, namely 15 Pa and 20 Pa, the morphology appears fibrous. SEM images of the annealed films are depicted in Figure 5.4 b. Here, a clear change is seen for all investigated deposition pressures, although the temperature treatment was conducted at only 100 K above the deposition temperature. The films in the deposition range of 1–10 Pa show a dense, brittle structure. For 15 Pa and 20 Pa, the layers seem to be consisting out of nanocrystallites in a porous structure. The XRD results are depicted in Figure 5.5. As a Bragg-Brentano setup was used, part of the signal represents the background of the amorphous oxide layer and the crystalline peaks of the silicon substrate. Nearly no crystalline peaks for the as-deposited films are seen. After annealing, broad crystalline peaks of rutile SnO_2 appear in the XRD results. It becomes clear that the crystallinity of the layers is enhanced by the anneal and that the structure is nanocrystalline in all cases, with arbitrary distribution of crystallites. Due to strong anisotropic peak broadening, the crystallite size could not be determined using the Rietveld refinement method. However, peaks broaden with deposition pressure, indicating smaller crystallite size for higher deposition pressure. Similar sizes are found for the deposition at 15 Pa and 20 Pa in line with the SEM results. An exception is found for the case of the deposition at 5 Pa. Here, the XRD results show a tendency of textured growth. The SEM results suggest a columnar growth in (200)-direction.

TEM investigations were conducted in order to have a closer look at the crystalline structure. The results of the annealed samples are shown in Figure 5.6. In the upper images, cross-sectional TEMs are depicted. For a deposition at 10 Pa, it can clearly be seen that the PLD layer comprises multiple sub-layers, as the laser is scanned over the target during the deposition process. At the boundary of the traces, boundary layers are visible, consisting out of non-crystalline amorphous or porous material. In the case of the deposition at higher pressures, such layers cannot be seen so clearly. The as-deposited SnO_2 under these conditions was most likely amorphous, cf. Section 5.2.1, and subsequently crystallized during the annealing step. The grain size was determined by high resolution TEMs (HRTEMs), which are depicted in the middle images. For 10 Pa, a grain size of 10–20 nm was found. For the depositions at 15 Pa

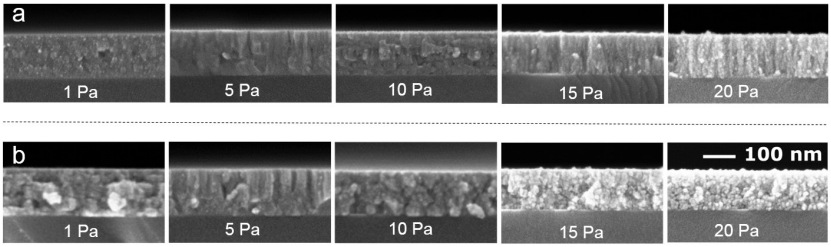

Figure 5.4. Cross-cut SEM micrographs of as-deposited (a) and post-annealed (b) tin dioxide layers deposited at different oxygen background pressures as indicated in the images. After Ref. [261].

and 20 Pa, the grain size is in the range of 3–10 nm. The distance of the lattice planes was determined by fast Fourier transformation (FFT), as the lower images show. The material composition can be determined from FFTs. The film consists mostly of (101) and (110)-oriented SnO_2. As a result, the material was found to be crystalline SnO_2. The layer deposited at the lowest pressure appears to have a dense structure. For the layers deposited at 15 Pa and 20 Pa, porous parts can be seen between the crystallites.

The morphology of the PL-deposited tin dioxide layers is strongly influenced by the deposition pressure. It was seen that the layers deposited at 10 Pa or lower appear to be completely dense with a layered structure from the deposition process. For the deposition at 15 Pa and 20 Pa a nanocrystalline porous structure is found. In addition, the grain size is slightly decreasing with increasing deposition pressure.

5.2.3. Conclusions

Both deposition temperature and pressure were seen to impact the morphology of the SnO_2 thin films. Porous, nanocrystalline material can be prepared at oxygen pressures at or above 15 Pa and subsequent temperature treatment. This material is expected to have appropriate properties for applications in resistive gas sensing.

5.3. CO-Sensing Properties

In this section, the influence of the deposition conditions on the CO sensing properties is investigated. To this end, samples of SnO_2 thin films were prepared on Ti-Pt IDEs. Deposition temperature, deposition pressure, and film thickness of the SnO_2 films were varied. Temperature treatment was conducted

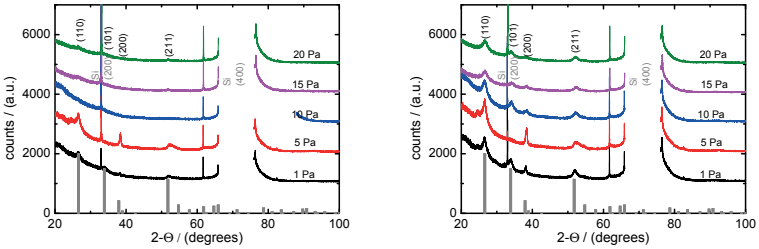

Figure 5.5. Bragg-Brentano XRD graphs of as-deposited (a) and post-annealed (b) tin dioxide thin films. Bar charts represent rutile SnO_2 powder diffractograms [264]. As-deposited films show crystalline peaks only for low deposition pressures. Post-annealed films show broad peaks indicating nanocrystalline structure. After Ref. [261].

in humid synthetic air for 4 h under constant flow at 400 °C. The gas response was detected via a measurement of the resistance change, in which a constant voltage is applied and the current is measured, as described in the experimental part in Section 3.2.3. As SnO_2 is a n-conducting MOX, the resistance decreases under exposure to reducing gases. The normalized sensor signal when exposed to CO is defined as in Equation 2.37.

5.3.1. Influence of the deposition pressure

As the deposition pressure has a high impact on the morphological properties of the PL-deposited films (cf. Section 5.2), the influence of the deposition pressure on the gas signal was investigated in detail. The dynamic sensor response to CO concentrations in the range of 5–50 ppm is depicted in Figure 5.7 a. The operation temperature of the sensor was 300° C. This temperature was chosen as it represented a medium temperature in the standard operation range for MOX CO sensors, which is 200–400 °C. [3]. Here, oxygen species are expected to be present on the surface as O^- or O^{2-} and represent possible reaction partners for carbon monoxide. The baseline resistance under operation conditions strongly increases with increasing deposition pressure, similar to the results found at room temperature in Section 5.1. For 1 Pa, the baseline resistance is approx. 1 kOhm, for 10 Pa, 7 kOhm, and 6 MOhm for the depositions at 15 Pa and 20 Pa. The initial dip of the resistance of the sensor with the deposition at 10 Pa deposition is due to the heat-up of the layer during the measurement and under gas flow. The sensor response to CO exposure also increased significantly with

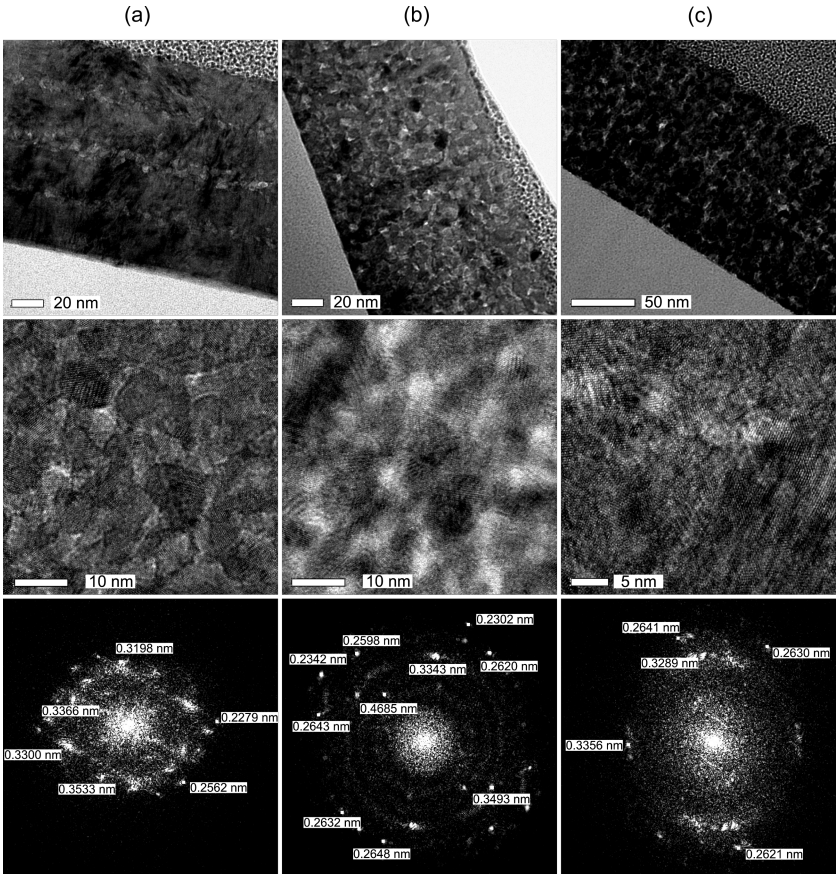

Figure 5.6. Upper row shows transmission electron micrographs, middle row HRTEMs and lower row FFTs of HRTEMs of post-annealed tin dioxide layers prepared at (a) 10 Pa (b) 15 Pa and (c) 20 Pa oxygen pressure. In the TEMs an overview of the complete PLD-layer cross-section is seen. In the HRTEM, single grains can clearly be distinguished. The lattice-plane distances are indicated in the FFTs.

increasing oxygen deposition pressure. Therefore, the relative sensor signal was calculated from Equation 2.37 and plotted in Figure 5.7 b. It is seen that S_{red} increases by several orders of magnitude for depositions above 10 Pa. The double-logarithmic plot shows a power-law relation without saturation, which is described by the following equation:

$$S_{\text{red}} = A \cdot c^{\kappa}, \tag{5.1}$$

where A is a constant, specific for the sensor signal (absolute response), c is the gas concentration (here: CO), and κ a parameter specific for the sensor sensitivity (relative change). Here, we find $\kappa \approx 0.35$ for $p_{\text{O}_2} = 1\,\text{Pa}$ and $\kappa \approx 0.6$ for $p_{\text{O}_2} \geq 10\,\text{Pa}$. This behavior is typical for depletion-dominated n-type metal oxides under exposure to reducing gases. Considering the different values of κ we can expect a difference in the gas-accessible grain structure, due to changed morphology, according to Barsan *et al.* [42]. The varied grain structure leads to a differing importance of the Schottky barriers at the grain contacts and thus a changed sensitivity. A relatively low value of κ, such as 0.35, indicates a compact film structure, whereas high values such as 0.6 are an indicator for porous layers.

In summary, there is a clear coherence between gas signal and deposition pressure. An increase in deposition pressure up to 15 Pa leads to higher response to CO [92]. This is most likely due to the increased porosity of the material resulting in a higher number of grain-grain contacts, thus increasing the relative resistance change.

5.3.2. Influence of the deposition temperature

Starting from results found in the literature (e.g. Ref. [166]), a temperature of 300 °C was chosen for standard depositions. At this value, a stable baseline and good CO response can be achieved. For comparison, a PL deposition at room temperature without backside heating was also tested. The results are summarized in Figure 5.8. The response S_{red} to CO in dry air is higher for deposition at room temperature, especially in the low concentration range below 20 ppm CO. Different slopes are observed in the double-logarithmic plot, leading to different exponents κ [29, 42]. This is most likely due to a slightly differing morphology, cf. Appendix C.1. During gas test, it was seen that the resistance baseline was a lot more stable in the case of the deposition at 300 °C. Therefore, such layers were taken as standard material for real applications.

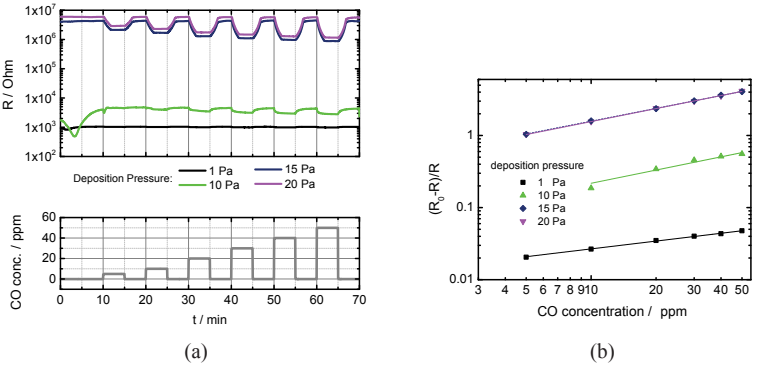

Figure 5.7. (a) Dynamic response of SnO_2 thin films prepared at different oxygen pressures. The lower graph shows the levels of exposed CO concentrations. (b) Normalized sensor signal of SnO_2 thin films prepared at different oxygen pressures, extracted from the signals shown in (a). Measurements were conducted at 300 °C in dry synthetic air. The solid lines represent power-law fits, with S_{red} being almost identical for the case of 15 Pa and 20 Pa. After Ref. [261].

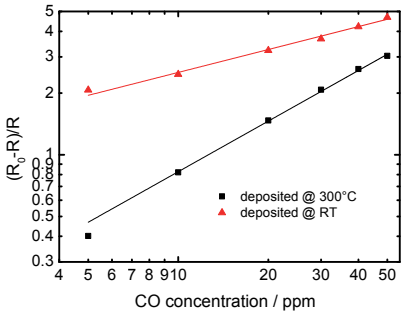

Figure 5.8. Normalized sensor signal of CO response in dry air for deposition at room temperature and at 300°C. Both layers were deposited at $p_{O_2} = 20$ Pa.

5.3.3. Influence of the film thickness

Film thickness is one of the major influence factors reported in the literature with respect to the gas sensing properties in the case of thin film sensors, see e.g. [41, 112, 166]. Within the scope of this work, the influence of the film thickness on the gas response was thus investigated in two cases: 1) in $p_{O_2} = 10$ Pa, where we expect a dense film and 2) in $p_{O_2} = 20$ Pa, where we expect a porous film, according to the previous sections. Therefore, films of different thicknesses were prepared.

For the deposition at relatively low oxygen pressure ($p_{O_2} = 10$ Pa), the film thickness was reduced to half the standard thickness of 140 nm by using only one trace of PL deposition. The sensor response to CO in dry air was then compared to the film of standard thickness, where the operation temperature was kept at 300 °C. The results presented in Figure 5.9 a show, that the sensor signal is in the same order of magnitude in both cases. However, for the thinner film, the baseline resistance is higher (see Table 5.2) and the sensor signal also has a slightly higher value. This behavior is explained by the model of the semiconducting MOX gas sensor, compare Figure 2.6 in Section 2.1.11. Here, the depletion zone is only established on the surface of the film. The reaction with the gas takes place on the surface of the compact film. In consequence, the gas signal is dependent on the film thickness, with increasing response for thinner films. It is well known, that this effect is especially pronounced if the thickness of the film and the extent of the depletion zone are of comparable size [42, 112].

At a deposition pressure of $p_{O_2} = 20$ Pa, the extracted gas signal is shown in Figure 5.9 b, for four different film thicknesses. The results show that the sensor signal is higher than for the case of the deposition at $p_{O_2} = 10$ Pa, but also comparable for all film thicknesses. In addition, the baseline resistance summarized in Table 5.2 is also similar in all cases. As the morphology of the annealed films deposited at $p_{O_2} = 20$ Pa is nanocrystalline and porous, we expect here the conduction to be dominated by the grain-grain contacts. In consequence, in a first approximation, the sensor signal is expected to be independent of the film thickness. However and in contrast to the results obtained for $p_{O_2} = 10$ Pa, we do see a somewhat higher response for the thicker films. This result is also supported by additional samples with a thickness of less than 100 nm which are not shown here. This behavior might be either due to a higher stability of the morphology of the material if the film thickness is increased or a reduced influence of the contact resistance which may also contribute significantly to the resistance and resistance change under gas exposure for non-ideal samples [3].

Table 5.2. Basic parameters of SnO_2 samples for investigation of thickness influence on gas signal.

p_{O_2} / Pa	Traces/ #	Thickness/ nm	Baseline resistance/ Ohm
10	1	70	$1.7 \cdot 10^4$
10	2	140	$4.3 \cdot 10^3$
20	1	55	$7.6 \cdot 10^6$
20	2	110	$3.7 \cdot 10^6$
20	4	230	$4.2 \cdot 10^6$

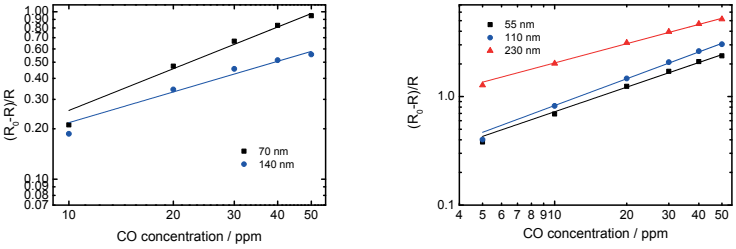

(a) (b)

Figure 5.9. (a) Normalized sensor signal of SnO_2 thin films deposited at $p_{O_2} = 10$ Pa for two different thicknesses, obtained with one trace or with two traces. Data extracted from Figure C.3. (b) Normalized sensor signal of SnO_2 thin films ($p_{O_2} = 20$ Pa), data extracted from Figure C.4. Thickness as indicated in the legend. Solid lines represent power-law fit. After Ref. [261].

The investigation of film thickness gave an insight into the working principle of the PLD SnO_2 thin film gas sensors. In the case of the low-pressure deposition, the layer most likely consists out of a compact film structure with gas interaction only on the surface. In consequence, the gas signal increases with decreasing film thickness. In the case of deposition oxygen pressure higher than 10 Pa, the film has a porous morphology leading to gas-accessible grain contacts. In consequence, the CO gas signal does not increase with decreasing film thickness. As a design rule, the SnO_2 films should be prepared with a minimum thickness of 100 nm to ensure a stable operation.

5.4. Metal Additives

Metal additives are often reported in the literature to enhance the gas-sensing properties [39, 70, 73, 75]. In most cases, noble metals such as Au, Pt, and Pd are used. Ni is a transition (non-noble) metal that is known to increase the resistance of SnO_2 [265, 266]. It is also widely accepted that not only the material but also the preparation technique highly influences the effect of the additive [74, 266, 267]. In this work, various kinds of metal additives and preparation techniques were investigated to enhance the CO-sensing properties.

5.4.1. Impact of metal additives on electrical and gas-sensing properties

Pd, Pt, and Ni were investigated as additives and added to the base material by thin film deposition after the MOX deposition and prior to anneal. Here, the film thickness variation was controlled to reach a value below 5 nm over the wafer. In the case of Pd also direct deposition from a composite target out of base material SnO_2 and Pd particles was conducted. In all cases, the aim was to reach a dopant concentration of about 5%. A temperature treatment was conducted at 400–800 °C in humid air. The features of the films with noble metal addition are summarized in Table 5.3. For Pt and Pd added by sputtering, the sensor response to CO increased, whereas the addition of Ni resulted in a very high baseline resistance but not in an increase in the CO response. In the case of AL-deposited Pt, the resistance only slightly increased due to metal addition and temperature treatment. However, the addition had a negative impact on the CO response.

The increase in resistance for the metal additives may be due to two different effects [74, 265, 266]:

1. If the metal is atomically distributed in the material it occupies acceptor levels.

Table 5.3. Effect of metal additives investigated in this work and qualitative results. R represents the baseline resistance.

Material	**Deposition**	**Impact on the CO-response**		**Impact on R**
		dry air	humid air	
Pt	sputtering	unchanged	increase	increase
Pt	ALD	decrease	decrease	increase
Pd	sputtering	unchanged	increase	slight increase
Pd	PLD	unchanged	increase	slight increase
Ni	sputtering	unchanged	not investigated	strong increase

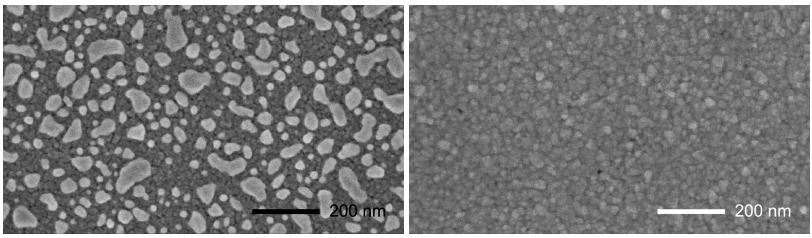

(a) (b)

Figure 5.10. Top-view SEM of SnO_2 thin films with noble metal additives (a) ALD-Pt and (b) sputtered Pd (T_{dep} =300° C, p_{O_2} = 10 Pa).

2. If the metal is present as small clusters, it increases the extent of the depletion zone (Fermi-level control).

Within the frame of this work, the root mechanism of additives to gas-sensing properties could not be investigated in detail. However, in the case of AL-deposited Pt, Pt clusters could be detected on the surface in SEM (see Figure 5.10 a). In consequence, the reduction in the response might be due to a rejection process on the surface, followed by a lower concentration of reacting CO at the SnO_2 surface. This was not the case for the sputter deposited and annealed, as well as the films deposited using a Pd-SnO_2 composite target (see Figure 5.10 b). Therefore, in those cases we expected the surface reaction to be small. Among the additives under investigation, Pd was chosen as the most promising additive for the application in CO sensing, as samples with Pd additive showed the best stability of baseline resistance and gas response under realistic operation conditions. In this context, the influence of humidity is an important parameter, as discussed in the Section 5.5.

Table 5.4. Overview of SnO_2 samples analyzed using XPS. p_{O_2} is the background deposition pressure.

Additive	p_{O_2} / Pa	Anneal	Position
Pd-sputtering	15	no	center
-	15	no	center
-	10	yes	center
Pd-sputtering	15	yes	center
-	20	yes	center
Pd-PLD	10	no	center
Pd-PLD	10	no	edge

5.4.2. Chemical investigation of Pd-doped SnO_2

XPS investigations were performed to determine, on the one hand, the basic composition of the thin films and the Pd distribution throughout the layer thickness on the other. In particular the influence of the preparation technique of the Pd-*doped* layer was investigated. Binding energies were analyzed using the O1s and the Sn3d5 peaks.

For this investigation, different samples were prepared, the properties of which are summarized in Table 5.4. A notable similarity of the binding energies was found for all samples, with the O1s peak maximum at 531 eV and the Sn3d5 peak maximum at 487 eV, typical for n-conducting SnO_2. The position of the Fermi level was determined by electrical contact to the layers. It was found that the Fermi level position was ≥ 3.5 eV above the valence band maximum. With a band gap of 3.5 eV, the Fermi level was at the edge or inside the conduction band. The latter case would refer to a degenerate semiconductor. However, water adsorbed on the surface might also influence the Fermi level position, as it is only determined at the surface and without cleaning. The fact that samples annealed in humid air feature a higher Fermi level position (3.8 eV compared to 3.5 eV for non-annealed) supports this assumption.

The composition of elements found on the surface of the SnO_2 thin films were quantified in an in-depth profile via XPS and sequential layer abrasion using argon sputtering. The results are shown in Figure 5.11 in the case of the non-annealed sample. It is seen that Pd is mostly present on the surface of the thin film. However, it can be detected throughout half of the film thickness, due to the porosity of the material. Quantitatively, the Pd concentration detected was around 0.3–0.45 at.%, which is one order of magnitude lower than the expected 5 at.%, as can be estimated by the sputtering rate. The reason for

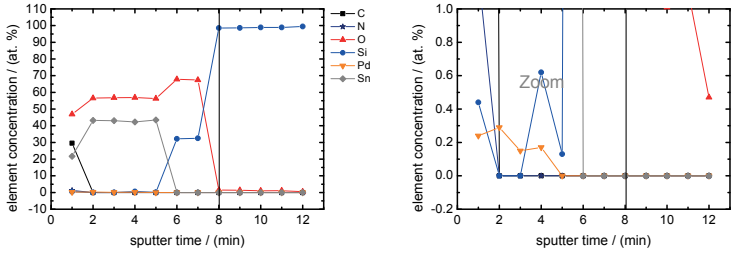

Figure 5.11. Element concentration determined by XPS of a Pd surface-doped SnO_2 film before annealing (a); (b) zoom of (a) to better visualize the Pd distribution.

this might be a lateral non-homogeneity in the case of the sputtering of such a thin film, so that the real sputtering rate on the investigated wafer was lower than the mean sputtering rate. For the annealed film with sputtered Pd, the additive was found to be distributed through the whole layer thickness. Accordingly, the detected Pd concentration was in the range of 0.1–0.2 at.%, see Figure 5.12. For the case of the deposition using the composite PLD target, the additive is also homogeneously distributed in the layer as seen from Figure 5.13. The Pd concentration is higher here, being about 0.5 at.%. However, it is lower than expected from the target concentration of 5 at.%. The reason for this could be the non-homogeneous distribution of the Pd additive in the commercially ordered Pd-SnO_2 target. Pd precipitation could be distinguished on the surface of the target. Both effects might be due to insufficient mixing of Pd and SnO_2 powders or a non-optimized sintering process. The Pd precipitates are not ablated in the PLD process due to the relatively low applied laser fluence. Consequently, the Pd content in the layer is lower than in the target.

In summary, there was an elemental analysis of the Pd-doped thin films. As expected, it was found that, for doping via thin film sputtering, the Pd was concentrated mainly on the surface for non-annealed samples. After heat treatment, Pd was equally distributed throughout the whole layer thickness. When the Pd-SnO_2 composite target was used, the metal was equally distributed in the layer from the beginning. The Pd-content was in the range of 0.2% for the sputtered Pd, which was considerably lower than expected from the layer thickness. In the case of the composite target, the Pd content was in the range of 0.5%, again much lower than the concentration in the target. This was primarily due

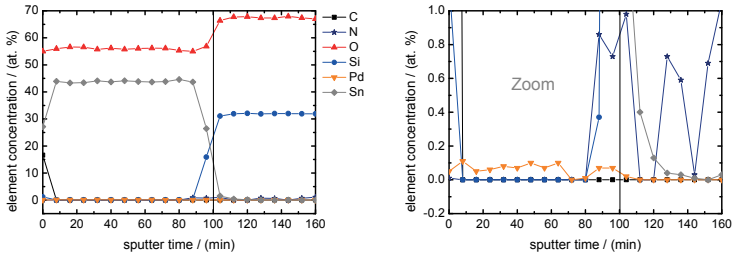

Figure 5.12. Element concentration determined by XPS of a Pd surface-doped SnO_2 film after annealing (a); (b) zoom of (a) to better visualize the Pd distribution. After Ref. [261].

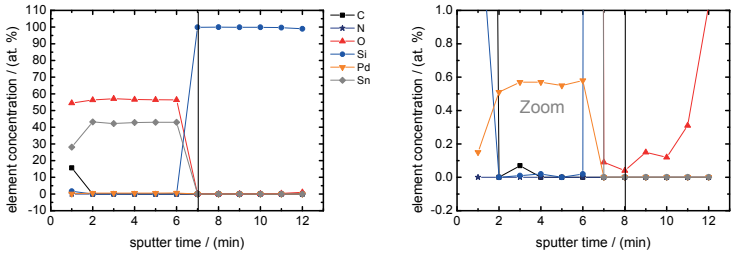

Figure 5.13. Element concentration determined by XPS of a Pd-SnO_2 film deposited using a Pd-SnO_2 composite target (a); (b) zoom of (a) to better see the Pd distribution.

to a non-homogeneous target composition. Pd was most likely present in the oxidized form as PdO.

5.4.3. Conclusions

Palladium was found to be the most promising metal additive to SnO_2 for improving the CO-sensing properties, particularly with respect to stability. XPS investigations showed that the metal was equally distributed throughout the whole layer thickness even if the metal was applied as a thin film after MOX deposition. However, the sample-to-sample variation of sputtered thin films was high. For application, a direct deposition of Pd-SnO_2 films using a composited target is expected to be most promising.

5.5. Influence of Humidity

The influence of ambient humidity on the gas sensor's baseline resistance and response to test gases is one of the most important issues concerning MOX sensors. Humidity is always present under realistic operation conditions in relatively high concentrations, 50% r.h. at 20 °C is equal to an absolute concentration of 1.15% or 11 500 ppm. This topic is discussed in the following.

Three different levels of humidity were chosen for investigating its influence on the CO response: 0% r.h. (*dry air*), 20% r.h., and 40% r.h. Figure 5.14 a shows the calculated response for a SnO_2 PLD thin-film-based sensor [261]. The graph shows that the sensor response has diminished in humid air, as reported similarly for pure tin dioxide [72]. It was also seen that the baseline resistance strongly decreased with an increasing level of humidity. This decrease is in the same order of magnitude as the response to 50 ppm CO in dry air. In Figure 5.15 a, a measurement of the dynamic response in humid air (20% r.h.) is shown. The resistance baseline tends to drift to lower values over time. SnO_2 thin films with Pd additive show a different behavior in their response to CO at different levels of humidity, as seen in Figure 5.14 b. The sensor with Pd (by sputtering) has a similar response to CO in dry synthetic air compared to the sensor without Pd-additive. It also shows a gas reaction that is comparable to the signal of SnO_2 in dry air. The dynamic response of the Pd-SnO_2 film, has a behavior similar to the pure SnO_2 thin film. However, the response to gases in humid air and the baseline stability is improved by the Pd addition, as shown in Figure 5.15 b.

The different gas-sensing behavior of both sensor types can be explained by the different surface chemistry. Under humid conditions, the signal of the tin dioxide material is reduced due to the competition between CO and OH

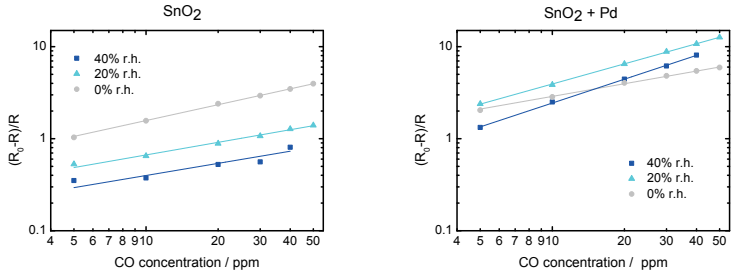

Figure 5.14. Normalized sensor signal for CO exposure at different levels of humidity as indicated in the legend. (a) pure SnO_2 and (b) Pd-doped SnO_2 obtained by sputtering. Operation temperature $T_{op} = 300\,°C$, deposition background $p_{O_2} = 20\,Pa$. After Ref. [261].

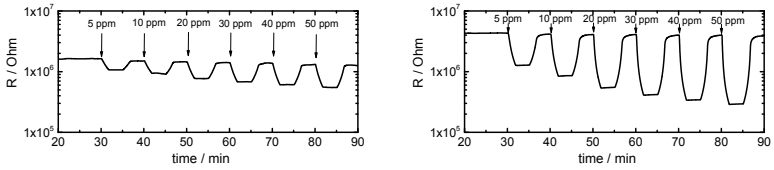

Figure 5.15. Dynamic response to CO at 20% r.h. for the case of (a) pure SnO_2 and (b) Pd-doped SnO_2 by sputtering. $T_{op} = 300\,°C$, deposition background $p_{O_2} = 20\,Pa$, film thickness $d_{film} = 110\,nm$. After Ref. [261].

on adsorption sites. For Pd-doped materials, the situation is changed and the competition is reduced. Now either a direct reaction of CO with OH-groups is possible if Pd is present [268] or fewer surface hydroxyl groups are formed [42, 269]; a recent study shows that the latter theory is more likely [74]. Here, the oxidation state of Pd also plays a certain role. Disperse Pd is likely to be present as PdO. The effect of Pd or PdO is not a direct chemical catalytic effect as it was found for Au, but an electronic effect by forming a strongly depleted surface layer that results in a shift of the Fermi level [39, 267, 270]. In dry conditions, the signals of Pd-doped and non-doped layers were found to be similar, which is in agreement with the results of Koziej *et al.* [269].

5.5.1. Conclusions

The strong impact of the humidity sensitivity and the high impact of the humid background on the CO response for the pure SnO_2 films are major drawbacks for gas sensors. However, if Pd is introduced into the thin film, the sensor response to CO in humid air is enhanced, the baseline stability is improved, and the impact of humidity on the baseline resistance is also reduced. The use of an additional humidity sensor might not compensate for the remaining effects due to its slow response. Further optimized Pd content or additional additives might improve the situation here in the future.

5.6. Cross-Sensitivity to NO_2 and Other Interfering Gases

In this section, the cross-sensitivity to interfering gases is discussed. In general, MOX sensors have the drawback of being rather non-selective. Therefore, the sensor response to sub-ppm concentrations of nitrogen dioxide (NO_2) was investigated. NO_2 is an oxidizing gas and an indicator for outdoor air pollution. In addition, the response to several other reducing gases was measured and compared.

5.6.1. Cross-sensitivity to NO_2

The sensing properties of Pd-SnO_2 (by sputtering) thin films with respect to CO and NO_2 were investigated at different operation temperatures (200–375 °C) and at different levels of relative humidity (0% r.h., 20% r.h., 40% r.h.). The films were exposed to five concentrations of CO (5–50 ppm) and two concentrations of NO_2 (0.5 ppm and 1 ppm). Dynamic responses were measured, an example can be found in Ref. [261]. The sensor resistance under NO_2 exposure is increased because NO_2 is an oxidizing gas. Hence, the normalized sensor signal is defined as in Equation 2.38. The responses at different temperatures are evaluated and are plotted in Figure 5.16. It clearly shows that the CO response increased in humid synthetic air with increasing temperature. For dry air, there is a peak in the response around 300 °C, and the sensor signal is lower than under humid conditions. In general, the response to CO (20 ppm) is in the range of S_{red} =2–3. However, for NO_2 very high responses (S_{oxid}>100 for 0.5 ppm NO_2) were obtained in relatively dry air at low temperatures. At 40% r.h. and at higher temperatures, the sensor signal was found to decrease. The differences in the temperature-dependent behavior of the sensor signal are most likely due to the reaction with the surface adsorbates. While CO reacts with pre-adsorbed oxygen species, NO_2 is expected to be ionosorbed as a reactive oxidizing gas at

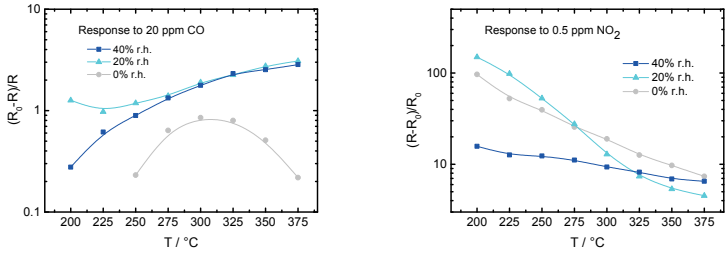

Figure 5.16. Temperature-dependent sensor signal for 20 ppm CO (a) and 0.5 ppm NO_2 (b) at different levels of humidity of Pd-SnO_2 films. Lines serve as guides to the eyes only. After Ref. [261].

the tin dioxide surface. This reaction takes place at lower temperatures all the way down to room temperature. The settling time for NO_2 was comparable with the time for CO, but the recovery time was very long with more than 10 min at temperatures below 300 °C.

5.6.2. Cross-sensitivity to other interfering gases

The resistive response was investigated for H_2, CH_4, C_3H_6, and NH_3 for the SnO_2 and Pd-SnO_2 (by sputtering) sensitive layers in dry conditions and at 30% r.h., see Figure 5.17. It was seen that the sensor has high cross-sensitivity to most of the investigated reducing gases.

When exposed to 5 ppm H_2, the sensor signal was higher than the one of 20 ppm CO, which is explained by a larger number of possible surface reaction partners in the case of hydrogen interaction [271] and by a higher reduction potential of hydrogen [267]. However, in the case of humid air, the response to hydrogen was lower for both sensor types. The response to 10 ppm methane is lower than the response to CO for both the doped and the undoped sensor. Especially under humid conditions, the response to methane was negligible. For propylene a high response in dry conditions was seen for both sensors along with a long recovery time. Also, here the signal is significantly reduced in humid air. The response for the doped sensor is significantly larger than for the non-doped one. There was also a high response to ammonia in humid air, which is similar for both sensors and higher than in dry air. Response and recovery times for the different gases are similar for both sensors. In humid air the baseline for the

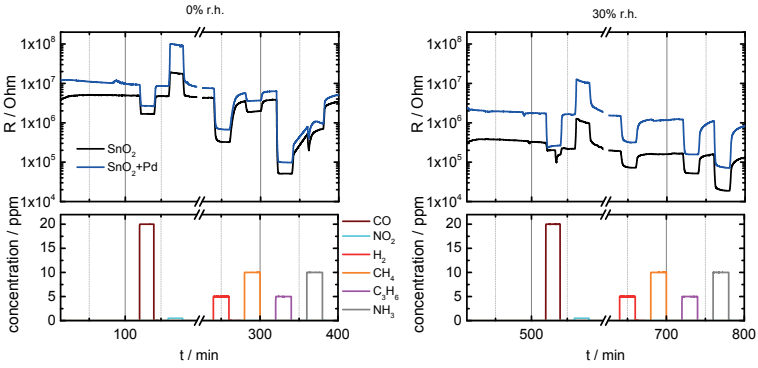

(a) (b)

Figure 5.17. Dynamic response of SnO_2 and Pd-SnO_2 films exposed to various concentrations of oxidizing and reducing gases (carbon monoxide, nitrogen dioxide, carbon dioxide, hydrogen, methane, propylene, ammonia) at $T_{op} = 300\,^{\circ}C$. The concentration of NO_2 was 0.5 ppm. After Ref. [261].

doped sensor was more stable, whereas in dry air the undoped sensor was more stable.

In summary, sensor response when exposed to various reducing gases in low concentrations was investigated. It was seen that SnO_2 shows high cross-sensitivity especially to propylene in dry synthetic air and ammonia in humid air. Although the cross-sensitivity to humidity was greatly reduced due to the Pd additive, the cross-sensitivity remained mainly unchanged. To deal with this issue, filters can be applied. Furthermore, the use of other MOX as alternative materials might enhance the selectivity of a gas sensor. WO_3 as an example is discussed in the following chapter.

5.7. Stability

In order to investigate stability and baseline drift, the chips were mounted on TO-8 sockets. The long-term measurements took place at the University of Tübingen. The CO measurements were repeated and showed good reproducibility (230 nm thick film with $p_{O_2} = 20$ Pa). Here CO concentrations in the range of 5–200 ppm were applied repeatedly at four different levels of relative humidity (0%, 10%, 20%, 50%). The full cycle was again repeated four times. In Figure 5.18, the determination of R_0 and R_{gas} is illustrated. The values of R_0 are

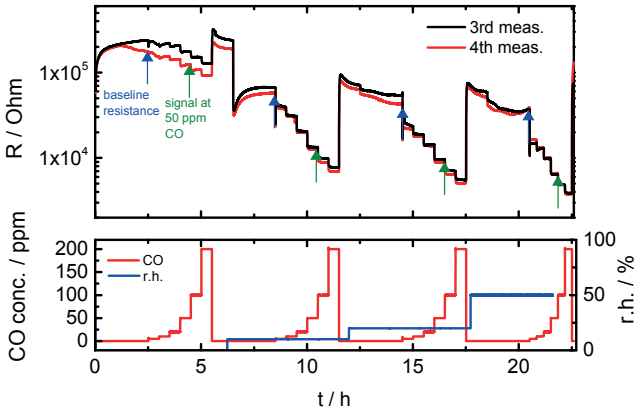

Figure 5.18. Baseline measurement with repeated CO- and humidity-exposure of a mounted sensor. Shown is the 3rd and the 4th measurement cycle. The relevant measurement points are highlighted by arrows. The time offset from the beginning of the first measurement is 38 h.

picked prior to the gas change. The signals extracted from cycle 3 and 4 can be found in the Appendix C.3. The 24h-baseline drift was defined as $R_n/R_{n+1}-1$, where n is the number of measurements. This value for the third and the fourth measurements was in the range of 0.05–0.15 in humid conditions. When we compare this value to the response to 50 ppm CO ($R_0/R_{\text{gas}}-1$), which is in the range of 3.6–4.8 in the investigated case, we find that this sensor signal is approx. a factor of 10 higher than the 24h-baseline drift in humid atmosphere.

5.8. Conclusions

In this chapter, the influence of the deposition parameters and additives to the properties of SnO_2 thin films prepared by large area PLD were discussed. Special attention was paid to the gas-sensing properties with respect to CO. It was seen that sensors based on SnO_2 thin films prepared at $p_{O_2} \geq 15$ Pa show promising response in the relevant concentration range for consumer electronic applications. Cross-sensitivity to humidity can be reduced by introducing Pd in the layer by sputtering or direct deposition of a composite target. The Pd content in the layer has to be further optimized in order to reduce the cross-sensitivity to other reducing gases, and for dedicated applications filters might be necessary.

6. Tungsten Oxide for Gas Sensing

In this chapter, the gas-sensing properties of WO_3 as an alternative material to SnO_2 were investigated. Besides SnO_2 it is the only metal oxide that is successfully used in commercial thick film gas sensors. WO_3 was reported to detect various reducing gases such as ethanol [272] and was found to be promising in sensing nitrogen oxides [273, 274]. Thin-film PLD WO_3 was found to be suitable for the detection of NO_x [275–277]. The investigated PLD films were not prepared with the Solmates tool—they were prepared using a specific ps-PLD tool at the Finnish company Picodeon Ltd Oy [242], the details of which can be found in. Ref. [278]. The infrared wavelength for the ablation laser was 1030 nm and the deposition pressure p_{O_2} was in the range of 5–20 Pa. The deposition took place in a pure oxygen atmosphere. All depositions were conducted without substrate heating. The thickness of the samples was controlled by the deposition time. It was in the range of 1.4–5.4 µm; thickness measurements were done by SEM. For each deposition pressure, layers of two different thicknesses were prepared. The process parameters are summarized in Table 6.1. After the deposition a heat treatment of two hours at $450\,^{\circ}C$ was applied for subsequent stabilization of the thin films. As can be seen from this table, the deposition rate depends on p_{O_2}. Higher deposition rates correspond with higher porosities of the layers and, thus, to higher thicknesses for the same deposition time. Large parts of this chapter were published in Ref. [242].

Table 6.1. Overview of Picodeon process parameters. Sample 9 has an additional dense bottom layer. After Ref. [242].

Sample #	$\mathbf{p_{O_2}}$ / Pa	**Dep. time /** min	**Thickness/** µm
1	5	5	3.6
2	5	2	1.4
3	7	3	4
4	7	1.3	1.9
5	10	2	4.7
6	10	0.8	2
7	20	1	4.8
8	20	0.5	2.1
9*	10	2	5.4

6.1. Morphological Properties

The morphological properties of the WO_3 films were characterized by Picodeon using SEM. The results are shown in Figure 6.1. The porosity increases with increasing oxygen deposition pressure [278, 279]. The soft and brittle structure of the deposited samples makes them very difficult to handle as the adhesion to the substrate is limited. Good adhesion was only found for the $p_{O_2} = 5$ Pa deposition and the dense bottom layer (see Figure 6.2). The film adhesion is better for the deposition at lower pressures, where the particles show a higher energy when impinging on the substrate surface. The as-deposited layers are generally amorphous and turn crystalline during heat treatment, as seen from both XRD and Raman results [278]. After temperature treatment the layers were found to comprise crystalline WO_3 with mainly γ-phase as analyzed by XRD [278, 279]. The columnar growth process leads to tree-like structures with branches [278]. With higher pressures the films show a highly-porous sponge-like structure. The high resolution SEM images allow for an estimation of the size of the nanoparticles, which are about 15–30 nm in diameter, see Figure 6.1 b. In the lower pressure range, the particles are more densely packed. This is illustrated in Figure 6.3, which shows schematic layer cross sections. The nanoparticles are formed in the plasma plume and are then deposited on the substrate. This regime is stated by Infortuna *et al.* [174] as having *no coherence* with direct deposition of clusters. In the case of the Picodeon tool, a porous microstructure appears already at very low pressures such as $p_{O_2} = 5$ Pa. This behavior is due to the specific non-equilibrium process of ps-PLD. Other PL deposition methods (ns deposition) [279] and depositions at higher temperatures [261] with the Solmates tool do not show a comparable effect. Another property that possibly plays a role is the different ablation process of the target. In the picosecond ablation the wavelength used is in the infrared. Consequently, the energy is lower than the band gap of WO_3. Generally, a denser microstructure at comparable deposition pressures can be achieved by applying substrate heating during deposition [174].

6.2. Electrical Properties

I-V-curves were measured at RT in order to characterize the electrical properties of the WO_3 films. Figure 6.4 shows exemplary results of three different interdigitated electrode structures for sample 1. Each measurement was repeated five times. The linear characteristic proves the ohmic behavior of the contacts. The contact resistance was estimated from transmission-line measurements (TLM)

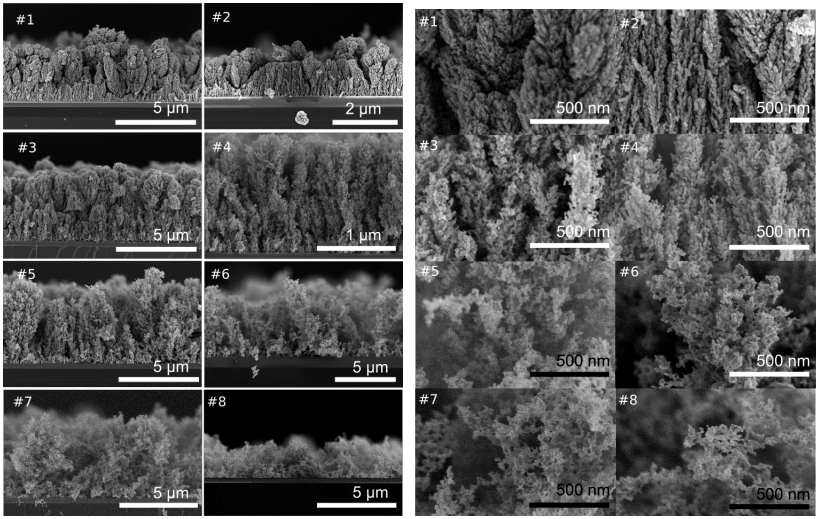

(a) (b)

Figure 6.1. Cross-sectional SEM micrographs of Picodeon WO_3 layers deposited in parallel to samples 1–8. From the upper to the lower images, p_{O_2} is increased. The films shown on the right have lower film thickness. Part (b) shows higher magnification of layers shown in (a). After Ref. [242].

at RT, see Figure 6.5. The linear fit included in the diagram is described by the following equation:

$$R_{\text{total}} = R_{\text{contact}} + R(b) \cdot b = 7.9 \cdot 10^4\,\text{Ohm} + 1.8 \cdot 10^4\,\text{Ohm}/\mu\text{m} \cdot b, \quad (6.1)$$

with R being the resistance and b the distance between the contacts in µm. The contact resistance is thus found negligible in the case of sample 1.

In Figure 6.6 the resistance values for the different depositions are summarized. The resistance increases for increasing p_{O_2} during deposition, with very high values of resistance at pressures above 7 Pa. It is expected that this increased resistance is due to the increased porosity of the layer, resulting in a reduction of contacts between the grains and reduced percolation paths. It was observed that the film thickness has only minor influence on the resistance. The upper layers do not seem to contribute to the electrical conduction. The measured resistance can be reduced using higher aspect-ratio structures. The IDE designs S01/S02 have an aspect ratio of 5, S20 has an aspect ratio of 333, and S26 of 119.

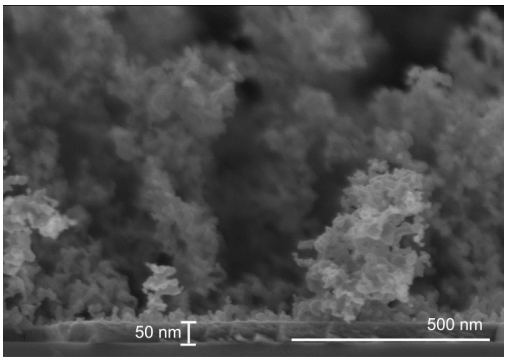

Figure 6.2. SEM-micrograph deposition in parallel to sample 9 showing the dense bottom layer and porous surface. After Ref. [242].

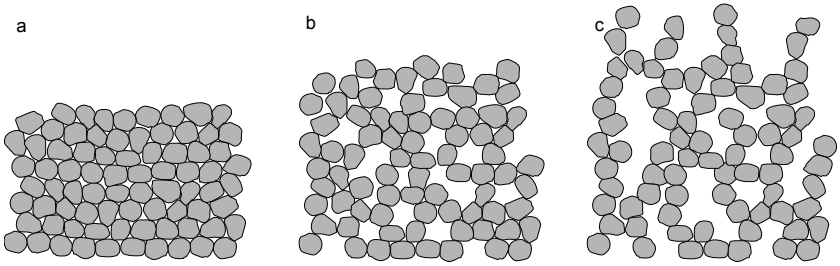

Figure 6.3. Schematic of layers consisting of equally-sized grains from dense (a) to porous (c). After Ref. [242].

As evident from the previous section, the resistive properties of the layers with higher porosity obtained with increasing deposition pressure are limited by a reduced number of grain-grain contacts with increasing deposition pressure. The different oxygen pressure during deposition can also influence the stoichiometry of the layers. This is expected to be of rather minor relevance for the electrical resistance in this study, as the strong effect of deposition pressure on the porosity is obvious.

6.3. CO Sensing Properties

WO_3 is not known as a standard material for sensing of CO. Nevertheless, in this work a CO sensitivity in dry synthetic air was found. The sensing mechanism of the resistive response of WO_3 to CO was investigated by Huebner *et al.*

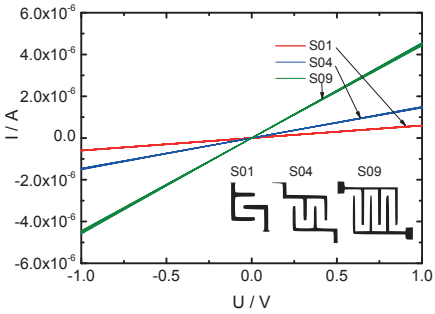

Figure 6.4. Exemplary *I-V*-curves measured at RT for three different interdigitated electrode structures for sample 1. Insets shows the geometry of the IDE contacts; the aspect ratios are 5 (S01), 12 (S04) and 28 (S09). After Ref. [242].

[60]. The results of the spectroscopic study using operando diffuse reflectance infrared Fourier transform spectroscopy (DRIFTS) indicated that the surface reactions for WO_3 differ from those of SnO_2 [60, 280]. The CO gas is expected to directly reduce the surface of WO_3. In consequence a response to CO is seen, even if it is dosed in pure nitrogen. This can be described by the following equation [60]:

$$CO(gas) + O_O \rightarrow CO_2(gas) + V_O^{\bullet\bullet} + 2e^-, \tag{6.2}$$

where O_O stands for an oxygen atom at an oxygen lattice place and $V_O^{\bullet\bullet}$ represents an oxygen vacancy. The resistive gas response on samples 1–9 was measured. Exemplary time-dependent response of the gas characterization in synthetic air is presented in Appendix D, which shows the resistive response to 10–200 ppm CO. The measurement took place at about 320° C sensor temperature, and IDE structures with an aspect ratio of 12 were used as substrates. The stabilization time of the sensors is quite short, and a stable baseline is reached already after 30 min for the first operation. The baseline resistance is higher for sample 2 , which has a lower film thickness than sample 1. Sample 3 also shows an increased resistance compared to sample 1. It is assumed that this is due to the higher porosity of the layer deposited at higher pressures as already seen for the RT resistance discussed in Section 6.2. In dry synthetic air, a direct and fast response to CO is seen, with the resistance decreasing with increasing CO concentration. The sensor signal to the reducing gas CO S_{red} is calculated as for SnO_2 in Equation 2.37, Section 2.1.11.

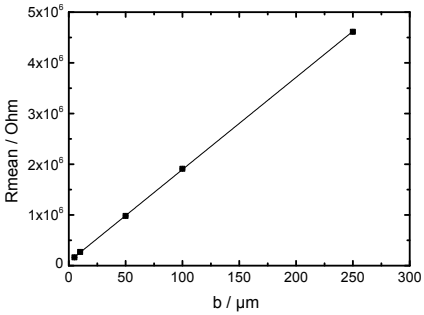

Figure 6.5. Transmission line measurement results for sample 1, which was used to determine the contact resistance. After Ref. [242].

The response can be described by a power-law function. A linear behavior in the double-logarithmic plot is seen in Figure 6.7. The power-law fit is described by Equation 5.1 in Section 5.3. Here, for all three sensors it is found that $\kappa \approx 0.4$ in dry air and $\kappa \approx 0.5$ in the case of 50% r.h., which is typical for porous grain-grain barrier controlled sensor response to reducing gases [42]. The response of the two films deposited at 5 Pa is similar. Thus, the influence of the film thickness is low. The response is not increased for the more porous layer deposited at 7 Pa. Measurement under humid conditions show a slower gas response but still a clear response to CO. If the sensor drift is subtracted using an exponential decay function, it is seen that the response to CO is not reduced in humid air, but on the contrary, it is clearly enhanced. This is also clearly seen in Figure 6.8 where the response to 200 ppm CO of different samples is summarized. This result is in line with a recent spectroscopic study [280] that shows that water has an oxidizing effect when adsorbed on the surface of tungsten trioxide.

6.4. NO_2-Sensing Properties

Previous studies showed a high response of PL-deposited WO_3 to nitrogen monoxide [278, 279, 281]. However, nitrogen dioxide was not investigated. In order to find the reaction mechanism of the actual materials and to compare gas reaction to different gases, the NO_2 sensing properties of these materials were also investigated.

A recent operando DRIFTS study by Staerz *et al.* hypothesizes that oxygen vacancies play a dominant role for WO_3 also in the interaction with oxidizing

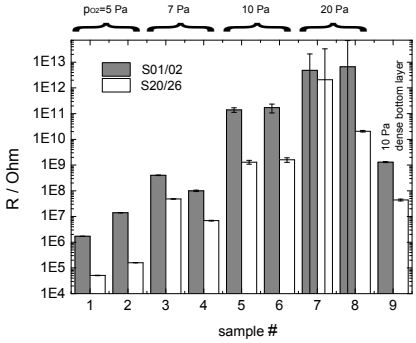

Figure 6.6. Overview of RT resistance for the different depositions. Mean values as determined by *I-V*-curves are shown. Error bars indicate standard deviations of five *I-V* measurements. Measurement errors are mostly due to a slight deviation from linear contact behavior. For layers deposited above 7 Pa, the resistance was difficult to measure. After Ref. [242].

gases and that in consequence mechanism (1) in Section 2.1.10 is best describing the interaction with NO_2, which can be expressed by the following equation:

$$NO_2(gas) + V_O^{\bullet\bullet} + 2e^- \rightarrow O_O + NO(gas). \tag{6.3}$$

Nitrogen monoxide gas (NO) is a reaction product in this process. For humidity, a similar mechanism was found, with water filling the oxygen vacancies [280]. On the surface of WO_3, nitrogen oxide and oxygen compete for adsorption places in humid air. Exemplary dynamic response to NO_2 is shown in the Appendix D. All sensors show a strong response to low ppb concentrations of NO_2 in dry air at 300 °C. It is seen that the response to NO_2 is slower than the response to CO with t_{90} up to 30 min. However, the recovery time is quite fast with t_{90} of only about 10 min. In Figure 6.9, the sensor signal to NO_2 S_{oxid} for samples 1–3 is shown, which is calculated according to Equation 2.38, Chapter 2.1.11. A saturation behavior can be observed for the concentrations above 1000 ppb. The reason for this effect is still unclear. In the case of humid air, the sensor signal to NO_2 is reduced due to a concurrence of reaction partners between water and nitrogen dioxide. This is also clearly seen in Figure 6.10, where the sensor response to 300 ppb NO_2 is summarized for various deposition pressures for 0%, 20% and 50% of relative humidity. The samples were prepared at various deposition pressures, as indicated in the diagram. While samples 1–6 show a relatively high NO_2 response, this response becomes much smaller for samples deposited at a background pressure of 20 Pa. In the case of sample 9 with a dense bottom layer, it is seen that the sensor resistance is

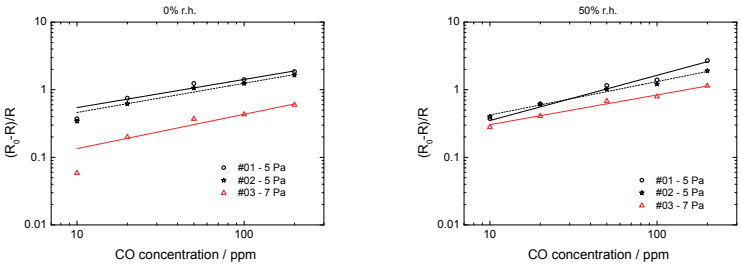

Figure 6.7. Sensor signal S_{red} for samples 1–3, part (a) shows relative sensor signal to CO in dry synthetic air and (b) at 50% r.h. Lines indicate a power-law fit. After Ref. [242].

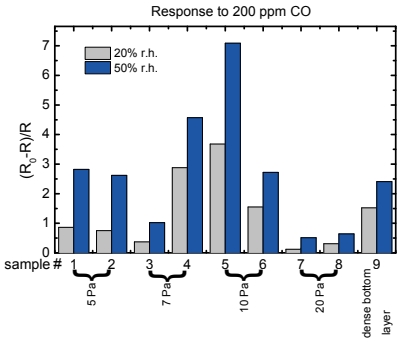

Figure 6.8. Resistive response to 200 ppm CO at different levels of humidity. After Ref. [242].

controlled by the low resistance of the bottom layer, strongly diminishing the response to CO and NO_2.

Gas response - cross sensitivity to other interfering gases

Cross-sensitivity to other gases (500 ppm CO_2, 5 ppm H_2, 5 ppm propylene, 10 ppm ammonia) was investigated at 300 °C, for two levels of relative humidity, namely dry synthetic air and 30% r.h. on a hotplate-based gas measurement system. The results are presented in Figure 6.11. It is seen that for prolonged exposure to humid air, a stable baseline is reached and the influence of the humidity on the baseline resistance is low. Exemplary sensors 1 and 2 deposited at $p_{O_2} = 5$ Pa were chosen for this study. Both sensors tested (same material,

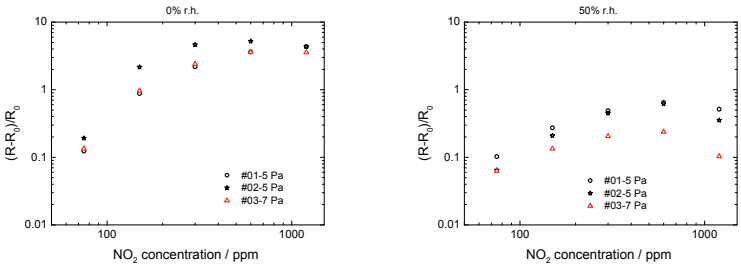

Figure 6.9. Sensor signal S_{oxid} for samples 1–3, part (a) shows relative sensor signal to NO_2 in dry synthetic air and (b) at 50% r.h. After Ref. [242].

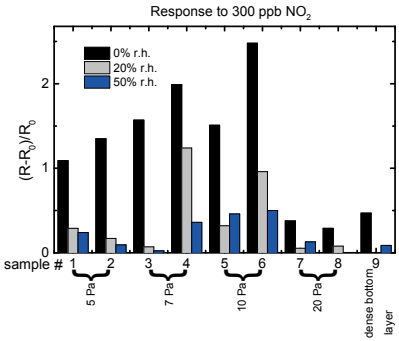

Figure 6.10. Resistive response to 300 ppb NO_2 at different levels of humidity.

different thickness) show a similar behavior with no response to 500 ppm CO_2. The response for hydrogen was moderate with a sensor signal of $S_{\text{red}} = 2$ in dry air and $S_{\text{red}} = 0.8$ in humid air. The response of the sensors to the reducing gases C_3H_6 and NH_3 is high in both dry and humid air. A sensor signal of $S_{\text{red}} = 41$ for 5 ppm propylene and $S_{\text{red}} = 6$ for 10 ppm ammonia in dry air is found. However, in the case of humid air, it is a bit reduced with S_{red}= 36 at 30% r.h. in the case of propylene, and $S_{\text{red}} = 4$ for ammonia. In summary, there is a certain cross-sensitivity to other reducing gases that should be addressed in future studies on this material.

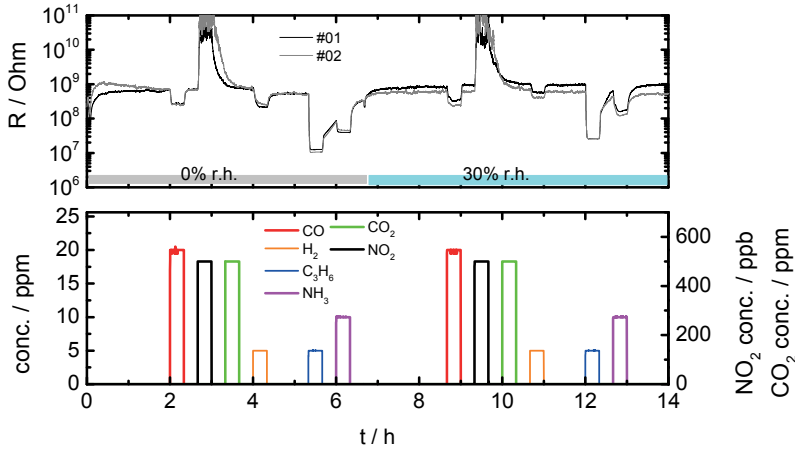

Figure 6.11. Cross-sensitivity investigation at 300 °C, at two levels of relative humidity. After Ref. [242].

6.5. Conclusions

It was found that highly porous gas-sensitive WO_3 thin films can be prepared by ps-PLD. The porosity of the layers is controlled by the deposition parameters. Porosity strongly increases with increasing oxygen pressure during deposition while the adhesion of the films decreases with increasing deposition pressure. The high porosity at rather low deposition pressure obtained with the ps deposition tool is attributed to its infrared laser ablation regime and its ultrashort pulses. The resistance of the layers both at room temperature and under operation conditions increases with deposition pressure. Good sensor signals to CO and NO_2 are already achieved at deposition pressures of 5 Pa. For very porous samples and very dense layers, the response to CO and NO_2 becomes smaller.

7. Miniaturization Strategies

Besides choosing the appropriate gas sensitive material, the layout of the whole sensor chip provides further potential for optimization. The main goal is the reduction in power consumption for future battery-powered applications. In this chapter, a parameter study of the hotplate design is carried out in order to investigate its influence on the power consumption. On the one hand, electrical characterization was carried out via four-terminal sensing. On the other hand, finite element method (FEM) simulations were conducted and the results were compared with reality, thus gaining insights into relevant heat-loss paths. Previous calculations showed clear deviations to measurements on initial membranes of a standard size. It is thus clear that a dedicated study is necessary to reveal these open points. Measurements and FEM simulations of this chapter were performed within the frame of a master's thesis by Ramona Zeisluft [247].

7.1. Overview of Miniaturization Study

This section gives a brief description of the strategy of the parameter study. Micromachined hotplate gas sensor chips fabricated in the Bosch Wafer Fab in Reutlingen were investigated in detail. A systematic variation of the membrane size was done. The aim was to find effects of the geometric design of the chip on the power consumption of the sensor. The chips investigated were not coated with any gas-sensitive film. They comprised a Pt-based heater and contacts on a stress-optimized silicon oxide-silicon nitride membrane. This membrane ensures a thermal insulation of the meander-shaped heater that is optimized to reach a target temperature homogeneously in the central part of the chip by Joule heating. In order to reduce the power consumption, the relation between the size of the meander and the membrane has to be optimized. The size of the membrane—not the size of the heating meander—was varied due to higher simplicity and easier processing.

Based on previous studies, it was expected that for minimizing power consumption the most decisive parameter would not be the total membrane size but rather the ratio between the heated area or meander area A_{M} and the reduced membrane area A_{reduced}, see Figure 7.1. With the membrane edge length a, we get the following relation for the reduced membrane size:

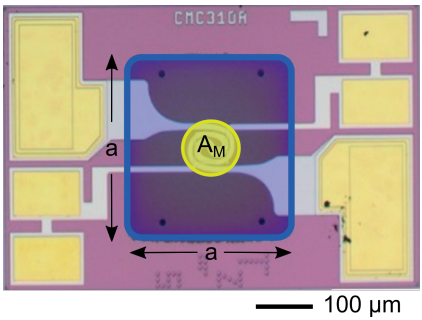

Figure 7.1. Optical micrograph of a test chip. a is the edge length of the membrane that is highlighted in blue; A_M is the meander area being equal to the active area of the MOX sensor. Adopted from Ref. [247].

$$A_{\text{reduced}} = a^2 - A_{\text{M}}. \tag{7.1}$$

For the parameter variation, in this work nine different square membrane sizes were chosen, ranging from $100 \times 100\,\mu\text{m}^2$ to $450 \times 450\,\mu\text{m}^2$ in side length. The initial and standard membrane size was $300 \times 300\,\mu\text{m}^2$. Optical micrographs of exemplary chips are shown in Figure 7.2.

7.2. Electrical Characterization of Miniaturized Hotplates

The electrical characterization of the miniaturized hotplates was done by four-terminal measurements. Thus, two needle probes were placed on each contact pad. A current in the range of 1–20 mA was applied and the voltage drop was measured. The correlation between resistance R and temperature T is given by:

$$R(T) = R_0 \cdot (1 + \alpha_T \cdot T), \tag{7.2}$$

where R_0 represents the resistance at a temperature of T_0=25 °C and α_{T} is the temperature coefficient. For platinum thin films, this coefficient was determined by test structures to be $\alpha_{\text{heater}} = 0.00297\,\text{K}^{-1}$ for the resistive heater and $\alpha_{\text{IDE}} = 0.00218\,\text{K}^{-1}$ for the interdigitated electrode (IDE) which represents the contact structure to the sensitive layer [247]. Using α_{heater}, the temperature T_x can be determined from the measured resistance R_x by the following relation:

$$T_x(R_x) = T_0 + \frac{R_x - R_0}{\alpha_T R_0}. \tag{7.3}$$

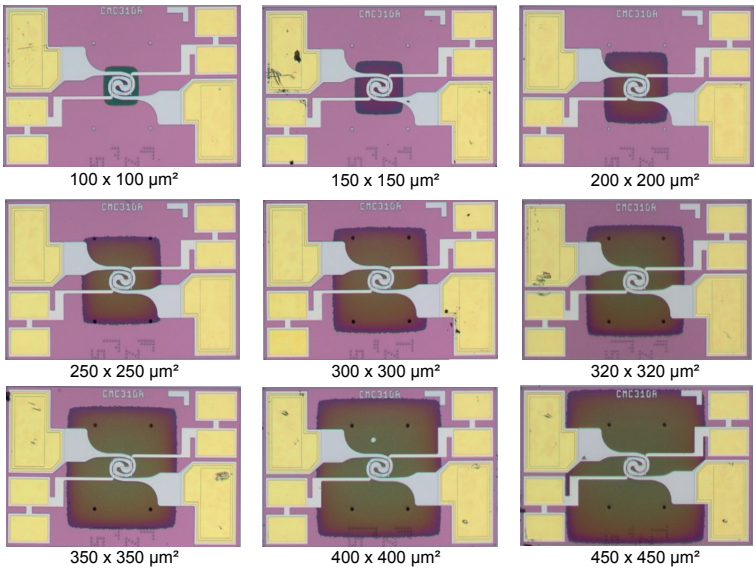

Figure 7.2. Optical micrographs of nine square membranes. Membrane side lengths are indicated in the images. Adopted from Ref. [247].

For the determination of the relation between power consumption and temperature of the active area, the temperature of the meander is set to 320 °C target operation temperature and the one of the electrical connections to 25 °C .

Figure 7.3 shows that for the membrane areas below 0.07 mm^2 there is a strong increase in power consumption equal to the relation of A_{reduced} to A_{M} of 5:1 or below. This can be understood by a simple geometrical consideration, presented in the work of Simon *et al.* [100, 115]. If we consider the heat which is transferred by heat conduction, Equation 2.42 in Section 2.5.1, and make the approximation of a round membrane with the radius r_{membrane}, we find that the heat conduction through the membrane is proportional to $1/\ln(r_{\text{membrane}}/r_{\text{heater}})$, with r_{heater} being the radius of the meander area. As a result, there is a saturation behavior of the heat loss through thermal conduction through the membrane, for larger membrane radii. From the analytical model, it is expected that there should be no significant reduction of the power consumption if a ratio of $r_{\text{membrane}}/r_{\text{heater}}$ in the range of 3–5 is reached [115]. In reality, however, further important heat-loss paths occur, as presented in Section 2.5.1, e.g. heat conduction through the air to the chip and to the mounting substrate and heat conduction through the air to the surroundings. Moreover, heat conduction takes place in

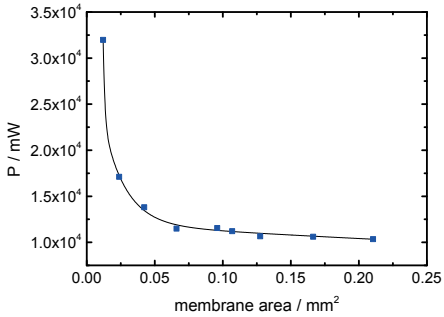

Figure 7.3. Required heating power needed for reaching the target temperature of 320 °C as a function of membrane area. Results are obtained from four-terminal resistance measurements. The standard deviation of the power consumption was found to be below 1% and the standard deviation of the membrane size was below 5% for all membrane variants.

the membrane through the metal connections. The analytical model can hardly predict other heat-loss paths, as presented in Section 2.5.1, without additional information, for example heat loss through thermal conduction of the air. Here, we need as boundary condition the temperature distribution over the heater and the range of air that is relevant for heat conduction. These conditions are not known from the beginning. Therefore, FEM simulations help to better understand the connection between heat loss and chip design.

7.3. FEM Simulation of Thermal Characteristics

FEM simulations were carried out in order to get a better understanding of the heat-loss mechanisms in the miniaturized gas sensor chips. The simulation software tool *ANSYS* was used and the simulation was conducted using a three dimensional model in a steady-state [247]. Thus, only heat loss by heat conduction is taken into account. By an analytical estimate, the heat loss by radiation and convection was found to be insignificant in the considered temperature range up to 320 °C [247]. The convective heat loss is small due to the low dimensions of the device, which do not allow for significant fluid motion [282]. It was estimated to be of 0.3 mW for the standard membrane and 0.6 mW for the largest membrane [247]. The heat loss by radiation $Q_{\text{radiation}}$ is strongly correlated to the temperature as described in the Stefan-Boltzmann law ($Q_{\text{radiation}} \propto T^4$), see Equation 2.43 in Section 2.5.1, so heat loss becomes only significant at temperatures higher than 400 °C [282]. At lower temperatures its

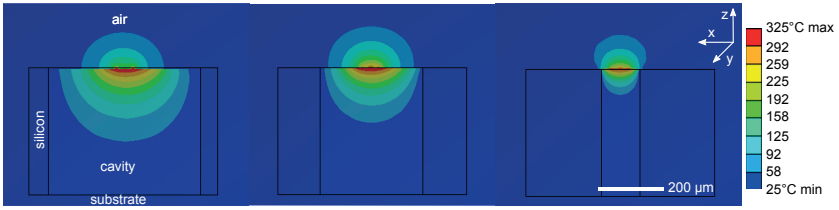

Figure 7.4. Temperature distribution in cross-section of the micro-hotplate for membranes with dimensions of $450 \times 450\ \mu m^2$, $300 \times 300\ \mu m^2$ and $100 \times 100\ \mu m^2$ (from left to right). The outer boarders of the cavity and chip are framed in black.

contribution to the total heat loss is a few percent or less as has been shown both analytically and experimentally in previous studies [205, 206]. A value of 0.1 mW of heat loss by radiation for both the standard membrane size and the largest membrane size was found [247]. In Figure 7.4, the temperature distribution in the x-z-plane of the chips due to FEM simulation is illustrated. In addition, the heat loss paths by thermal conduction are illustrated in Figure 7.5 for clarity. In Figure 7.4 exemplary three sample geometries were chosen, a large (lateral dimensions $450 \times 450\ \mu m^2$), a standard ($300 \times 300\ \mu m^2$), and a small membrane ($100 \times 100\ \mu m^2$). More precisely, mainly the heat conduction through air is depicted. The heat source being the heated meander, it can hardly be distinguished in the image due to its low thickness of a few hundred nanometers compared to the thickness of the chip, which is 375 µm. Figure 7.4 shows that the heat distribution is not symmetrical in z-direction orthogonal to the virtual plane presented by the membrane[1]. This is due to the low thermal resistance of the cavity compared to the open space in air. The small gap between the membrane and the substrate/cavity edge increases the thermal heat flow in the case of the smaller membrane. The hemisphere of heated air on the surface has a lower volume for the two larger membrane variants. This is due to lower thermal resistances in the cavity in these geometries. Although the thermal conductivity λ_{th} of the air is significantly lower than that of the membrane due to its low density (exemplary $\lambda_{th,SiO_2} = 1.51\ \frac{W}{mK}$ and $\lambda_{th,air} = 0.037\ \frac{W}{mK}$), there is a significant heat loss through the air due to the small dimensions of the device and respective scaling factors.

In Figure 7.6 the results of electrical measurements and the results of the FEM simulations are compared. The same trend is seen for both the simulation

[1] The slight asymmetry in x-direction is explained by the plane cut of the image. The heat conduction represented by the Pt connections is non-symmetrical in every cutting plane, cf. optical micrographs (top view) in Figure 7.2.

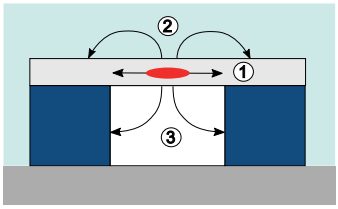

Figure 7.5. Illustration of the distribution of the heat loss through heat conduction to the silicon chip, (1) through the membrane, (2) through the air (top side), and (3) through the air in the cavity. The heater presenting a thermal source is highlighted in red.

and the measurements concerning the power consumption. It is reduced for increasing membrane areas approaching a value of about 10 mW for the larger membrane variants. Measured results and simulations are in very good agreement. However, for the smallest membrane a quite large discrepancy between the electrical and simulation results was found. Two kinds of simplifications are assumed to be responsible for this discrepancy: In FEM simulation, the root cause for errors is the meshing of the finite elements, which are of limited size. For the electrical measurements the assumption is that, the temperature of the meander is homogeneous and equal to 320 °C, and that the temperature of the chip is equal to room temperature. This assumption works better for the larger membranes. For the smallest membrane, simulation results of the lateral heat distribution of the membrane show, that only a part of the meander reaches the target temperature of 320 °C. Thus, for the smaller membranes, this results in an underestimation of the power consumption by the simulation. If the whole meander should reach at least the target temperature, this would lead to a higher power consumption. Consequently, for the smaller membranes a larger divergence between measurement results and simulation is found, as seen from the left part of Figure 7.6.

For a better understanding of the heat losses of the chip, stationary-thermal simulations were conducted in the FEM model. Thus, the heat conduction to the chip which is illustrated in Figure 7.5 represents the largest part of the heat loss for all membrane variants, with 85% for the standard membrane [247]. The heat loss to the surrounding air and directly to the sensor mounting substrate below the cavity is less significant. In Table 7.1 the results of the FEM simulations of different heat-loss paths through heat conduction to the chip are summarized for a large, a medium, and a small membrane. This more differentiated consideration was reached by turning on and off of parts of the heat loss through the air in the simulation model and recalculation. It is seen that different dominant heat-loss paths exist for different membrane geometries. For all membrane types,

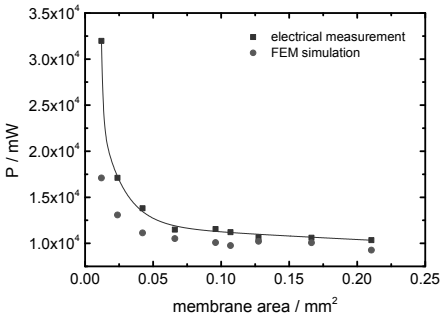

Figure 7.6. Comparison of thermoelectrical FEM simulation and four-terminal resistance measurements. Power consumption is shown for a target temperature of 320 °C in relation to the membrane area. Line serves as a guide to the eyes only.

Table 7.1. Heat-loss paths for three different membrane sizes as parts of total heat loss.

heat loss path	$450 \times 450\ \mu m^2$ $0.2\ mm^2$	$300 \times 300\ \mu m^2$ $0.09\ mm^2$	$100 \times 100\ \mu m^2$ $0.01\ mm^2$
1) membrane to chip	49%	55%	87%
2) air (top side) to chip	≈0%	3%	6%
3) air in the cavity to chip	29%	26%	≈0%

the part of the heat that is transferred through the air on the top side to the chip is significantly smaller than the other parts. It is seen that this part approaches zero for increasing membrane size. In the case of the smallest membrane, most of the heat (87%) is transferred through the membrane directly into the solid chip. This is due to the small thermal resistance of the membrane, as the meander (heater) edge is placed very close to the edge of the membrane. More precisely, the part of the membrane that is not covered by the meander is only 3% of the total membrane area. For the larger membranes the thermal shielding is significantly better. The fraction of heat, that is transferred through the cavity air to the chip increases with increasing membrane size. The transducer with the standard membrane shows the largest fraction of heat loss through the membrane but also an important part is represented by the loss through the air in the cavity to the chip (26%). Similar results are found for the case of the largest membrane, whereas for the smallest membrane this heat-loss path is insignificant and most heat is transferred through the membrane and the air of the top side.

7.4. Conclusions

In this chapter, the power consumption of micro-hotplates for miniaturized resistive gas sensors was analyzed in order to get a better understanding of the relationship between design and electrical properties. The aim is to find possibilities to further reduce the power consumption. Therefore, the results of four-terminal sensing of the Pt resistances are compared to three-dimensional thermo-electrical FEM simulations for nine different membranes with sizes ranging from $100 \times 100\,\mu m^2$ to $450 \times 450\,\mu m^2$. The overall measurements and simulations are in good agreement. What is most important about the connection between power consumption and temperature is not the total membrane size but the ratio between membrane size and the size of the meander-shaped heater. The required power consumption for an operation temperature of 320 °C approaches 10 mW for increased membrane sizes. If the relation of free membrane area to heater area is 5:1 or above, almost no further reduction in power consumption can be achieved. This result has been verified by both measurements and FEM simulations. In addition, it is seen by FEM simulations, that for different membrane geometries there are different dominant heat-loss paths. To begin with heat is transferred through the solid membrane, with a share of up to 87% for the smallest membrane. The heat loss by thermal conduction through the air in the cavity represents also an important part for larger membranes with a value of 26% for the standard-sized membrane of $300 \times 300\,\mu m^2$. The results of this work can be used as a guideline for future design of miniaturized hotplate geometries and multi-pixel gas sensors.

8. Conclusions and Outlook

In this work, several aspects of miniaturization of a chip-based gas sensor for sensing of the toxic and odorless gas CO were investigated. The main focus was on reducing the power consumption to a value of a few mW and on miniaturizing the chip size, thus opening up the prospect of mass market applications and mass production. With respect to sensitivity, the goal was to ensure a detection of CO in the concentration range of 5–50 ppm, which is relevant to consumer electronics (CE). The gas sensor is based on a metal oxide (MOX) thin film that changes its resistance when heated and exposed to the reducing gas CO. Therefore, novel materials and processes were developed.

8.1. Conclusions

MOX sensors based on thin films require very good (and reliable) contacts to the electrodes that serve as lines to external connections, e.g. bondpads, and as contact to the sensitive material. In the first part of this thesis, Pt contact structures with Ti adhesion promotor were designed in order to fulfill both tasks. A bi-layer lift-off process was established and optimized, and lift-off resists (LOR) of various thicknesses were used. Thus, due to the isotropic sputtering source, shadowing occurred during the deposition, resulting in different edge geometries for different resist geometries. It was seen that, for a certain resist thickness, ideal smoothly tapered edges were formed. The experimental results are in line with the results from iterative calculations. The smoothly tapered edges promote good contact with the thin sensing films of the devices based on MOX layers.

The second step was to improve the gas-sensitive material. In conventional resistive CO sensors, a thick film MOX material is applied. In this work, the aim was to create gas-sensitive thin films, as these do not have principle limitations for further miniaturization. The large-area pulsed laser deposition (PLD) technique was established in order to deposit the MOX films on wafer level. Therefore, a Solmates ns-PLD tool was utilized. Four-point probe measurements gave a good measure of the layer quality as the resistivity is dependent on both the stoichiometry and the morphology of the layers. RT resistivity of the MOX films was found to depend on the oxygen pressure during deposition. Resistivity of the films increases with increasing oxygen pressure for n-type MOX,

which can be explained by a higher oxygen ratio in the layer material, and consequently a lower carrier concentration. As evident from SEM, the deposition conditions also highly impact the morphology of the films. The layers were deposited on Pt interdigitated electrode contact structures with different aspect ratios for applications in gas tests. Specially designed two-side trenched silicon shadow masks were used to pattern the MOX films directly during deposition.

The SnO_2 films were investigated in further detail as they exhibited a good and stable gas response to CO, superior to that obtained with ZnO, CuO, In_2O_3, and WO_3. Depositions were conducted at 300 °C and had a subsequent temperature treatment at 400 °C in humid air. Sufficiently stable materials for the application in gas sensing were found. Depositions in the upper deposition pressure range (>10 Pa) resulted in porous films. TEM and XRD investigations showed that these layers consist out of nanoparticles in the size range of 3–10 nm. The high oxygen content in these layers and high number of grain-grain contacts resulted in a high baseline resistance at both room temperature and under operation conditions (300 °C). Excellent response to CO was found for the porous samples. Denser layers from deposition under lower oxygen pressure showed a weak response.

Various metal additives such as Ni, Pt, and Pd - were introduced into the SnO_2 film to improve the performance in humid air. Both the resistance baseline of the layer and the sensor signal was influenced by humidity for the undoped layers with the sensor signal to CO being diminished in humid air. Pd was found to show the best improvement to the gas-sensing properties. It was introduced by sputtering and a subsequent temperature treatment. Thereafter it was present throughout the whole layer thickness, as seen from XPS investigations. The sensor baseline was more stable for undoped layers and the gas signal was increased in the case of humid air. This is most likely due to a Fermi-level control mechanism in the interaction of the Pd-PdO-SnO_2 three phase boundary. However, for a sensor signal independent of the humid conditions, the Pd content in the layer has to be further optimized. In order to gain information about sensor cross-sensitivities to other gases, the temperature-dependent sensor response to NO_2 was investigated. It was seen that the sensor has a high response to NO_2 at low operation temperatures (200 °C), which stood in contrast to the sensing of CO for which the sensor should be operated at temperatures above 300 °C. In addition, the cross-sensitivity to hydrogen, methane, ammonia and propylene was investigated and it was found quite high for all gases except methane.

Furthermore, ps-PL-deposited WO_3 was investigated, showing less densely packed crystallites than in the case of the ns-PL-deposited SnO_2. The porous samples showed a good response to CO. Despite their even higher porosity, the WO_3 layers deposited in the upper pressure range of the ps-PLD tool did not

show a further improvement in the sensor signal. The layers were highly resistive, very fragile, and difficult to handle. The sensor response to CO was high both for dry and humid air, whereas the response to NO_2 was decreased under humid conditions. As in the case of SnO_2, there was certain cross-sensitivity to the reducing gases, namely hydrogen, ammonia, and propylene in both dry and humid atmosphere.

Finally, a parameter study was conducted on the sensor chip and its heated membrane. The aim of this was to get insights into further miniaturization options. For this purpose the behavior of sensors with nine differently sized membranes was studied. All other dimensions, as well as the heater, were not changed. Experimental studies were carried out using four-terminal measurements of resistance. Hence, the temperature-dependent resistance of the Pt heater was used for the estimation of the temperature of the active area on the chip. When comparing thermo-electric FEM simulations and experimental results, it was seen that there is a strong correlation of membrane size and total power consumption beneath a membrane size of $300 \times 300\,\mu m^2$. For this size, the power consumption for heating the active area to 320 °C was found to be 10 mW. Larger membrane sizes only led to a small further reduction in power consumption. The dominant heat-loss paths of the sensor were different for the different membrane sizes. In all cases, the most important heat transfer was via thermal conduction in the membrane. Another important heat-loss path was—especially for larger membranes—through the heat conduction through the air inside the cavity. The results found in this parameter study can be used as design rules for further miniaturized and design of multi-pixel gas sensor chips.

8.2. Outlook

Interesting paths for further research on miniaturized, low power, and selective CO gas sensor chips are summarized in the following:

- **Hall measurements** should be conducted on the thin films in order to gain a better understanding of the interplay between the layer morphology and electrical properties. The impact of the grain-boundary scattering, which results in a change in electrical mobility, can be separated from the impact of the stoichiometry that leads to a change in carrier density.

- The **Pd content** in the layer should be optimized in order to further reduce the humidity cross-sensitivity. For the Pd-SnO_2 material developed in this work, the response in the presence of humidity is increased. However, both the baseline resistance and the sensor signal are dependent on the

level of relative humidity. Layers of the best properties are expected to be achieved by deposition from a Pd-SnO_2 composite target.

- **Alternative additives and filters** should be introduced in order to further reduce the cross-sensitivity to other reducing gases. Charcoal-based filters are already successfully used against hydrocarbons and other volatile organic compounds [283]. Material combinations of different MOX such as CuO and SnO_2 are under investigation for a more selective response to CO. Despite their improved selectivity, they often show deficits with respect to sensor response and stability. A sensor chip with different sensing materials—a multi-pixel sensor—is expected to substantially improve the selectivity.

- **Structuring** of the thin films by wet or dry etching methods could not sufficiently be addressed within this work. The shadow mask deposition process, results in relatively large patterned areas. A sacrificial layer technique might be a good option to structure multiple MOX thin films on a common sensor chip [284].

- **MOX deposition on miniaturized heated membranes** should be tested in order to obtain complete miniaturized CO gas sensor chips. For this purpose various topics have consequently to be addressed such as the compatibility of the patterning process with the hotplate and stress introduced by the thin film to the membrane.

- **Temperature modulation** can be applied in order to reduce the cross-sensitivity of the gas sensor chip without the need for an additional material. As it was seen that the response to CO and NO_2 is high in different temperature regimes, the use of temperature modulation for the increase in selectivity is expected to be promising.

- **Reliability** testing of the thin-film-based gas sensors should be further extended to gain experience and to define requirements for a CE sensor. So far, only measurements over relatively short periods of time (several days) have been carried out. There should be long-term testing over weeks and months under more realistic working conditions. Ambient air, air with contaminating substances e.g. sulfurous compounds or siloxanes, and air with different pollution levels should be used for such tests.

A. Experimental

Table A.1. Basic parameters and aspect ratio of the used Ti-Pt IDE structures.

Structure number	Finger length / μm	Finger gap / μm	# Finger	Aspect ratio
1	62	25	3	5.44
2	62	25	3	5.44
3	62	25	3	5.44
4	37.5	12.5	4	11.8
5	37.5	12.5	4	11.8
6	75	25	4	11.8
7	75	25	4	11.8
8	75	12.5	6	28.2
14	75	12.5	6	28.2
13	75	12.5	6	28.2
15	150	25	6	28.2
9	150	25	6	28.2
10	300	50	6	28.2
22	75	12.5	6	28.2
21	75	12.5	6	28.2
26	300	25	10	119.2
20	300	12.5	14	333.6

B. Alternative Materials

In this section, various metal oxides that were prepared by PLD are compared. First, the morphological properties, then the electrical and the gas-sensing properties are presented. The morphological properties are investigated by SEM.

B.1. Morphological Properties

Various metal oxides thin films were prepared on the wafer level, and the morphological properties were investigated by SEM. The morphological properties of ZnO, CuO, and WO_3 were compared with SnO_2. The results are shown in Figure B.1 for the pressure regime of 1–10 Pa. It was seen that, in the same pressure regime, different structural properties for different materials appear. All materials showed a rather amorphous structure at 1 Pa deposition pressure. For the deposition at 5 Pa, all layers were quite dense, and for 10 Pa a more open morphology appears for all materials except WO_3, which still appeared quite dense. For the case of ZnO, the material showed a strong columnar growth especially in the low-pressure regime of 1 and 5 Pa. This result was stressed by the XRD results, which showed a preferential growth in (002)-direction. For the case of CuO also a columnar growth structure appeared. In the case of SnO_2, the grains were randomly orientated.

B.2. Electrical properties

The electrical properties of the MOX thin films were investigated by four-point-probe measurements. This was done to pre-characterize the layers prior to gas measurements. The sheet resistance of the MOX layers depends on both its crystallinity and stoichiometry. The carrier concentration is a function of the oxygen content in the layers. ZnO, WO_3 and In_2O_3 are n-type oxides, in consequence oxygen vacancies represent donors, whereas metal ion vacancies represent acceptors in p-type oxides such as CuO. The carrier mobility is a function of the crystallinity and crystal size of the polycrystalline thin film. Thus the measurement of the sheet resistance is a sensitive instrument for the characterization of MOX films on the wafer level. The measurements were conducted at room temperature in a controlled environment (20 °C, 50% r.h.) using an automatic four-point-probe measurement system which measured 81 points over

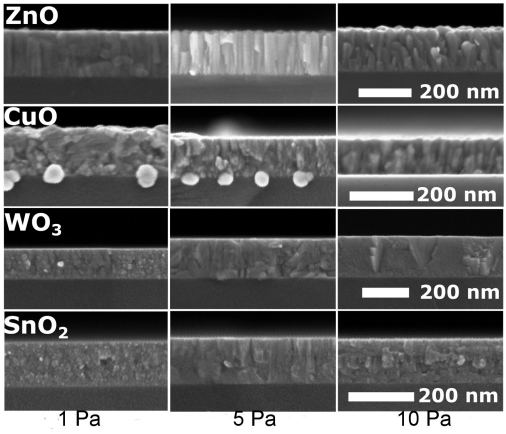

Figure B.1. Cross-sectional SEM micrographs of various MOX thin films

the wafer. From these results the mean values were taken. The results depicted in Figure B.2 show that the conductivity of the various metal oxide layers can be controlled by adjusting the oxygen pressure in the deposition chamber, as already seen for SnO_2 in Chapter 5. ZnO was seen to be especially highly resistive at deposition pressures and had resistances too high to be measurable with the four-point-probe system. The same layers deposited on structures with Ti-Pt-contacts led to an estimation in the range of 10^4 Ohm cm. Additional depositions of ZnO were conducted in an argon atmosphere. They showed a significantly lower resistivity due to less oxygen input during deposition. However, layers grown in argon atmosphere also appeared denser in the SEM images than layers deposited at same pressure in oxygen.

B.3. Gas-sensing properties

Prior to gas measurements, the samples were annealed in humid synthetic air at 400 °C for 4 hours for stabilization. This led to an increase in the sheet resistance most probably due to further oxygen input in the layers. For SnO_2 and CuO the resistance increased less than factor 10, WO_3 showed an increase of less than factor 100 whereas the low resistive ZnO, prepare at 1 Pa oxygen background pressure showed a resistance increase as high as factor 10^4.

Gas measurements were conducted on a heated chuck using a total flow of 1000 sccm of dry synthetic air. Measurement results from ppm concentrations of different PLD-deposited layers are shown in Figure B.3. The normalized

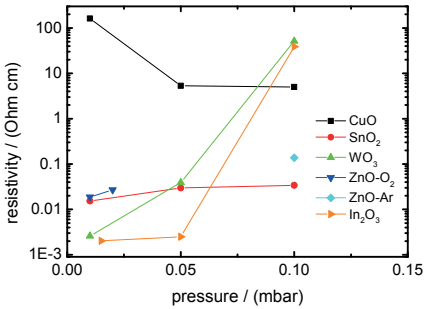

Figure B.2. Resistivity range for different MOX films deposited at various oxygen pressures and 300 °C. For ZnO films both argon and oxygen were used as background gases (see legend).

sensor response is defined as in Equation 2.37 for n-type oxides and for CuO (p-type) as

$$S_{\mathrm{red,p}} = (R_{\mathrm{gas}} - R_0)/R_0. \tag{B.1}$$

Here, the resistance increases under CO-exposure. The PL-deposited WO_3 did not show a measurable response to CO. SnO_2 and In_2O_3 showed the highest response under these conditions, where the SnO_2 baseline was more stable. CuO showed a quite linear response to different concentrations of CO. However, the signal did not reach the equilibrium in a measurement time of 5 min. ZnO films showed high resistance and low response to concentrations higher than 20 ppm, where the sensor signal almost reached saturation.

B.4. Conclusions

The resistance of thin films of different metal oxides prepared by large area PLD on silicon substrates could be controlled by changing the oxygen pressure in the deposition chamber. All oxides except WO_3 prepared with the Solmates deposition tool showed resistive response to 5-50 ppm concentrations of carbon monoxide. The sensor response was compared to SnO_2 which showed the highest and most stable response to CO.

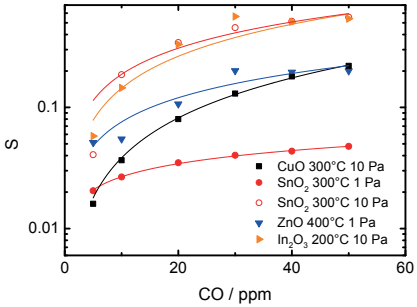

Figure B.3. Measurement temperature and deposition pressure as indicated in legend, sensor signal $S = (R_0 - R_{\text{gas}})/R_{\text{gas}}$ for n-MOX and $S = (R_{\text{gas}} - R_0)/R_0$ for CuO.

C. SnO_2

C.1. SnO_2 morphology of RT deposition

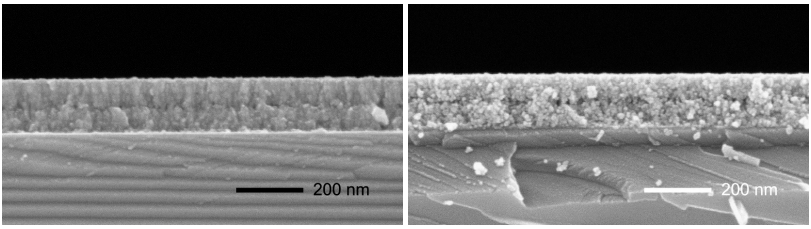

(a) (b)

Figure C.1. SEM results of as-deposited (a) and post-annealed (b) SnO_2 films deposited at room temperature, $p_{O_2} = 10$ Pa.

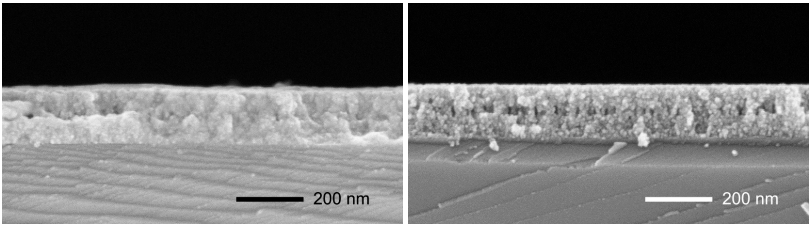

(a) (b)

Figure C.2. SEM results of as-deposited (a) and post-annealed (b) SnO_2 films deposited at room temperature, $p_{O_2} = 15$ Pa.

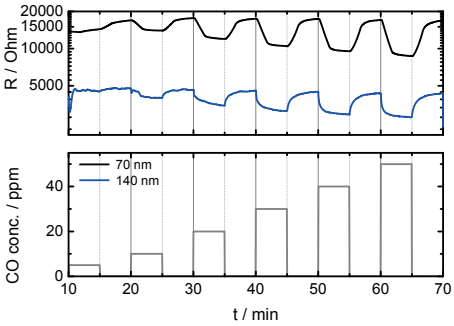

Figure C.3. Dynamic response of SnO_2 thin films ($p_{O_2} = 10$ Pa), different thicknesses were used (one trace and two traces), as indicated in the legend.

C.2. Dynamic response for SnO_2 films of different thickness.

C.3. Stability

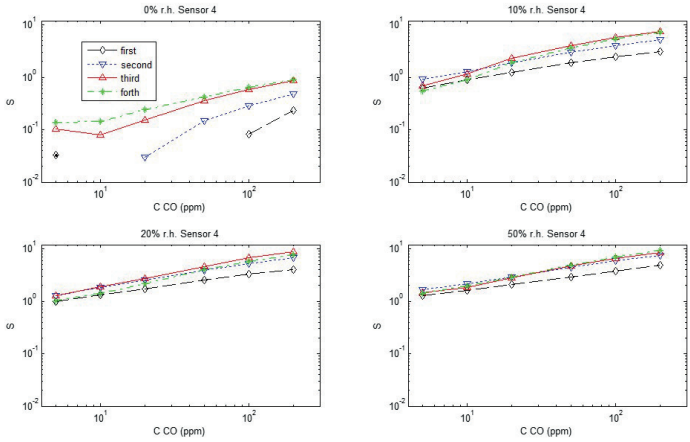

Figure C.5. Extracted CO response for repeated measurements.

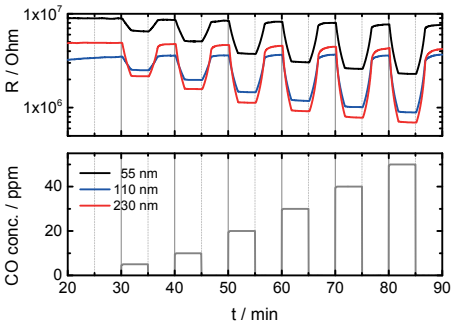

Figure C.4. Dynamic response of SnO_2 thin films ($p_{O_2} = 20\,\text{Pa}$), different thicknesses were used (one trace, two traces, and four traces), as indicated in the legend.

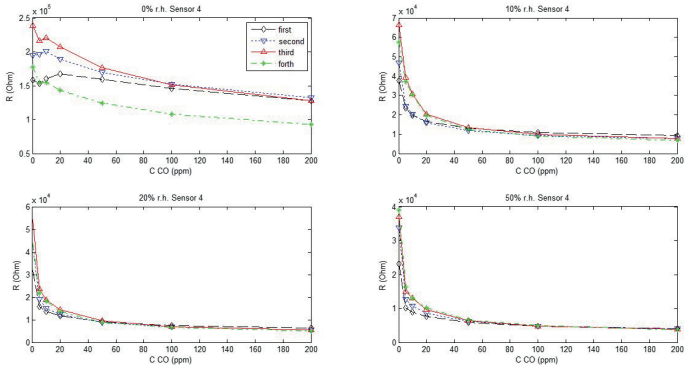

Figure C.6. Extracted sensor baseline for repeated measurements.

Table C.1. Baseline drift after repeated operation (measurement duration: measurement 1: 16 h, measurement 2–4: 23.5 h): $R_n/R_{n+1} - 1$. Operation was conducted at different levels of humidity.

Measurement	0% r.h.	10% r.h.	30% r.h.	50% r.h.
First-Second	-0.19	-0.2	-0.26	-0.32
Second-Third	-0.18	-0.29	-0.2	-0.08
Third-Forth	0.35	0.15	0.24	-0.05

Table C.2. Baseline drift after repeated operation (measurement duration: measurement 1: 16 h, measurement 2–4: 23.5 h): $R_n/R_{n+1} - 1$. Operation was conducted at different levels of humidity.

Measurement	0% r.h.	10% r.h.	30% r.h.	50% r.h.
1	-0.01	1.91	2.51	2.91
2	0.15	2.97	3.88	4.48
3	0.35	3.97	4.62	4.78
4	0.42	3.62	3.98	4.87

D. WO_3

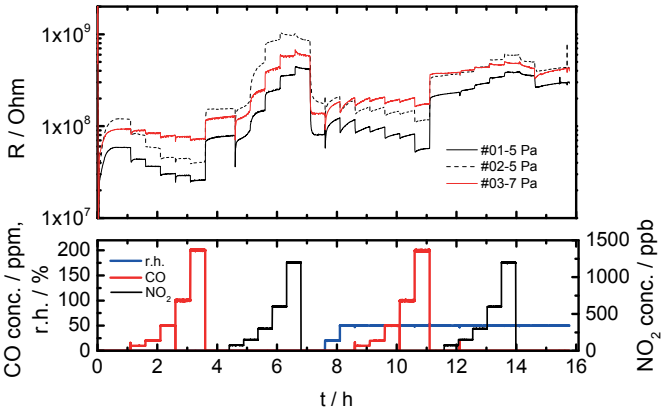

Figure D.1. Resistive gas characterization of WO_3 deposition 1–3. As stated in the legend, the deposition pressure was 5 Pa for sample #01 and #02 and 7 Pa for sample #03. The film thicknesses are 3.6 μm, 1.4 μm and 4 μm respectively.

Publications

Journal publications

[1] E. M. Preiss, A. Krauss, and H. Seidel. “Sputtered Pt electrode structures with smoothly tapered edges by bi-layer resist lift-off”. In: *Thin Solid Films* 597 (2015), pp. 158–164.

[2] E. M. Preiß, T. Rogge, A. Krauß, and H. Seidel. “Tin oxide-based thin films prepared by pulsed laser deposition for gas sensing”. In: *Sensors and Actuators B: Chemical* 236 (2016), pp. 865–873.

[3] E. M. Preiß, A. Krauß, V. Kekkonen, N. Barsan, and H. Seidel. “Characterization of WO_3 thin films prepared by picosecond laser deposition for gas sensing”. In: *Sensors and Actuators B: Chemical* 248 (2017), pp. 153–159.

Conference publications

[1] E. Preiss, A. Krauss, and H. Seidel. “Comparative study of large area pulsed laser deposited metal oxides for gas sensors applications”. In: *Solid-State Sensors, Actuators and Microsystems (TRANSDUCERS), 18th International Conference on*. June 2015, pp. 1499–1502.

[2] E. M. Preiß, T. Rogge, A. Krauß, and H. Seidel. “Large-area pulsed laser deposition oft tin oxide for gas sensor applications”. In: *GSSMO Workshop*. Tübingen, 2015.

[3] E. M. Preiß, T. Rogge, A. Krauß, and H. Seidel. “Gas Sensing by SnO_2 Thin Films Prepared by Large-area Pulsed Laser Deposition”. In: *Procedia Engineering* 120 (2015). Eurosensors 2015, pp. 88–91.

Patent applications

[1] T. Lutz, F. Hernandez-Guillen, F. Heuck, and E. Preiss. “Messvorrichtung, Herstellungsverfahren zum Herstellen einer Messvorrichtung und Verfahren zum Betreiben einer Messvorrichtung”. DE102014206067A. 2015.

[2] A. Krauss and E. Preiss. “Herstellungsverfahren für eine mikromechanische Sensorvorrichtung und entsprechende mikromechanische Sensorvorrichtung”. Patent application *pending*. 2017.

[3] A. Krauss and E. Preiss. “Verfahren zum Herstellen einer nanokristallinen, gassensitiven Schichtstruktur, entsprechende nanokristalline, gassensitive Schichtstruktur, und Gassensor mit einer entsprechenden nanokristallinen, gassensitiven Schichtstruktur”. Patent application *pending*. 2017.

Danksagung

Diese Arbeit entstand in den Jahren 2013 bis 2016 bei der Robert Bosch GmbH in der Zentralen Forschung und Vorausentwicklung an den Standorten Gerlingen-Schillerhöhe und Renningen. An dieser Stelle möchte ich mich bei allen bedanken, die zum Gelingen dieser Arbeit beigetragen haben. Mein besonderer Dank gilt...

- meinem Doktorvater Professor Dr. Helmut Seidel für die Betreuung seitens der Universität des Saarlands sowie die Diskussionen, das Feedback und die Unterstützung während meiner Promotionszeit.

- Professor Dr. Udo Weimar von der Universität Tübingen für das Interesse an meiner Arbeit und die Übernahme des Korreferats.

- meinem fachlichen Betreuer bei der Robert Bosch GmbH Dr. Andreas Krauß, dafür dass er mich die ganze Zeit über fachlich und persönlich unterstützt hat. Er hatte immer ein offenes Ohr und ohne die zahlreichen Diskussionen mit ihm wäre diese Arbeit nicht möglich gewesen.

- meinem Abteilungsleiter Dr. Kilian Bilger, meiner Gruppenleiterin Dr. Silvia Kronmüller und meinem Gruppenleiter Dr. Andreas Burck dafür, dass sie mir die Industriepromotion ermöglicht haben.

- Dr. Tino Fuchs sowie dem gesamten Gassensor-Projekt für die gute Zusammenarbeit, anregende Diskussionen und tatkräftige Unterstützung.

- Tobias Rogge und Ramona Zeisluft für ihr außergewöhnliches Engagement während seines Praktikums bzw. ihrer Masterarbeit. Mit ihrer Unterstützung entstanden wichtige Ergebnisse für meine Doktorarbeit.

- dem gesamten Institut für Physikalische Chemie der Universität Tübingen dafür, dass sie es mir ermöglicht haben, Messungen dort durchzuführen und mich so freundlich aufgenommen haben. Für die Unterstützung bei den Messungen danke ich besonders Dr. Alexandru Oprea und Dr. Nicolae Barsan, für seine Unterstützung und für die vielen Diskussionen über Metalloxid-Gassensorik.

- Dr. Daniel Pantel und Andreas Schatz und sowie der Firma Solmates für die Unterstützung bei den PLD-Abscheidungen. Ville Kekkonen von der Firma Picodeon danke ich für die Abscheidungen an der ps-PLD Anlage.
- Professor Dr. Lothar Spieß und Dr. Thomas Kups von der TU Ilmenau für weitere Materialcharakterisierung mit TEM und GIXRD.
- der Abteilung CR/ARC insbesondere Dr. Philipp Nolte, Philipp Pfander und Dr. Martin Schreivogel für die Unterstützung bei den Gasmessungen und der Diskussion der Ergebnisse.
- meinen Kolleginnen und Kollegen bei CR/ARY, die ein sehr angenehmes Umfeld für die Arbeit geschaffen haben. Für die Unterstützung im Reinraum danke ich noch einmal besonders Sabine Nagel, Volker Becker, Joachim Rudhard, Dr. Johannes Kenntner und Peter Frey.
- meiner Familie, insbesondere meinen Eltern und meiner Schwester, dafür dass sie mich in meinem Wissensdurst bestärkt, mir das Studium ermöglicht und mich in allem unterstützt haben.

List of Figures

List of Tables

Bibliography

[1] J. Choi. *Scent diffusion apparatus and method*. US Patent 6,371,451. Apr. 2002.

[2] accessed 01/2017. url: `http://www.aromyx.com/`.

[3] N. Barsan, D. Koziej, and U. Weimar. "Metal oxide-based gas sensor research: How to?" In: *Sensors and Actuators B: Chemical* 121.1 (2007). Special Issue: 25th Anniversary of Sensors and Actuators B: Chemical, pp. 18–35.

[4] NJHealth. *Hazardous Substance Fact Sheet*. New Jersey Department of Health. Jan. 2010.

[5] BArbBl. *Technische Regeln für Gefahrstoffe - Grenzwerte in der Luft am Arbeitsplatz Luftgrenzwerte.* Bundesminister für Arbeit und Sozialordnung. July 2004.

[6] EPA. *Protect your family and yourself from carbon monoxide poisoning*. United States Environmental Protection Agency. 1996.

[7] Gesundheitsberichterstattung des Bundes. *Sterbefälle nach äußeren Ursachen und ihren Folgen (ab 1998). Gliederungsmerkmale: Jahre, Region, Alter, Geschlecht, Nationalität, ICD-10 (V-Y), ICD-10 (S-T)*. 2014. url: `http://www.gbe-bund.de`.

[8] accessed 01/2017. url: `http://eniac-safesens.eu/`.

[9] W. H. Brattain and J. Bardeen. "Surface Properties of Germanium". In: *Bell System Technical Journal* 32.1 (1953), pp. 1–41.

[10] T. Seiyama and S. Kagawa. "Study on a Detector for Gaseous Components Using Semiconductive Thin Films." In: *Analytical Chemistry* 38.8 (1966), pp. 1069–1073.

[11] N. Taguchi. "Gas detecting element and method of making it". US Patent 3644795A. 1972.

[12] figaro. *TGS 3870 - for the detection of both methane and carbon monoxide*. MOS.

[13] figaro. *TGS 5042 - for the detection of Carbon Monoxide*. EC.

[14] Fraunhofer IPM. *Colorimetric gas sensors*. Tech. rep. Fraunhofer Institute for Physical Measurement Techniques IPM, 2015.

[15] accessed 10/2016. url: http://www.arctic-products.co.uk/products/co-smoke-safety/carbon-monoxide-detector-twin-pack/.

[16] J. Courbat, M. Pascu, D. Gutmacher, D. Briand, J. Woellenstein, U. Hoefer, K. Severin, and N. de Rooij. "A colorimetric CO sensor for fire detection". In: *Procedia Engineering* 25 (2011), pp. 1329–1332.

[17] H. Hartnagel, A. Dawar, A. Jain, and C. Jagadish. *Semiconducting transparent thin films*. Institute of Physics Pub. Bristol, UK, Philadelphia, PA, 1995.

[18] V. Henrich and P. Cox. *The surface science of metal oxides*. Cambridge university press, 1996.

[19] K. Hauffe and S. Morrison. *Adsorption: Eine Einführung in die Probleme der Adsorption*. De Gruyter Studienbuch. De Gruyter, 1974.

[20] S. Morrison. *The chemical physics of surfaces*. 2nd ed. 1977 Plenum Press, New York, 1990.

[21] S. Das and V. Jayaraman. "SnO_2: A comprehensive review on structures and gas sensors". In: *Progress in Materials Science* 66 (2014), pp. 112–255.

[22] O. Madelung, U. Roessler, and M. Schulz. "IV-VI2 compounds, general tables crystal structure, lattice parameters of GeO_2, SnO_2, PbO_2". In: *Non-Tetrahedrally Bonded Elements and Binary Compounds I*. Springer Science + Business Media, 1998, pp. 1–5.

[23] S. Semancik and D. Cox. "Fundamental characterization of clean and gas-dosed tin oxide". In: *Sensors and Actuators* 12.2 (1987), pp. 101–106.

[24] J. Maier and W. Göpel. "Investigations of the bulk defect chemistry of polycrystalline Tin(IV) oxide". In: *Journal of Solid State Chemistry* 72.2 (1988), pp. 293–302.

[25] Z. Jarzebski and J. Marton. "Physical properties of SnO_2 materials I. Preparation and defect structure". In: *Journal of The Electrochemical Society* 123.7 (1976), pp. 199C–205C.

[26] A. K. Singh, A. Janotti, M. Scheffler, and C. G. Van de Walle. "Sources of Electrical Conductivity in SnO_2". In: *Physical Review Letters* 101 (2008), p. 055502.

[27] S. Lany and A. Zunger. "Dopability, intrinsic conductivity, and nonstoichiometry of transparent conducting oxides". In: *Physical Review Letters* 98.4 (2007), p. 045501.

[28] Z. Jarzebski and J. Marton. “Physical properties of SnO_2 materials II. Electrical properties”. In: *Journal of The Electrochemical Society* 123.9 (1976), pp. 299C–310C.

[29] N. Barsan, M. Schweizer-Berberich, and W. Göpel. “Fundamental and practical aspects in the design of nanoscaled SnO_2 gas sensors: a status report”. In: *Fresenius' journal of analytical chemistry* 365.4 (1999), pp. 287–304.

[30] M. Sinner-Hettenbach, M. Göhelid, T. Weiß, N. Barsan, U. Weimar, H. von Schenck, L. Giovanelli, and G. L. Lay. “Electronic structure of SnO_2(110)-4x1 and sputtered SnO_2(110) revealed by resonant photoemission”. In: *Surface Science* 499.1 (2002), pp. 85–93.

[31] T. Vogt, P. M. Woodward, and B. A. Hunter. “The high-temperature phases of WO3”. In: *Journal of Solid State Chemistry* 144.1 (1999), pp. 209–215.

[32] R. L. Petritz. “Theory of Photoconductivity in Semiconductor Films”. In: *Phys. Rev.* 104 (1956), pp. 1508–1516.

[33] T. Yamamoto. “Codoping for the fabrication of p-type ZnO”. In: *Thin Solid Films* 420 (2002), pp. 100–106.

[34] M. J. Madou and S. R. Morrison. *Chemical sensing with solid state devices*. Elsevier, 1989.

[35] M. Henzler and W. Göpel. *Oberflächenphysik des Festkörpers*. Teubner Verlag, 1994.

[36] W. Göpel. “Solid-state chemical sensors: Atomistic models and research trends”. In: *Sensors and Actuators* 16.1–2 (1989), pp. 167–193.

[37] P. B. Weisz. “Effects of Electronic Charge Transfer between Adsorbate and Solid on Chemisorption and Catalysis”. In: *The Journal of Chemical Physics* 21.9 (1953), pp. 1531–1538.

[38] J. W. Orton and M. J. Powell. “The Hall effect in polycrystalline and powdered semiconductors”. In: *Reports on Progress in Physics* 43.11 (1980), p. 1263.

[39] N. Yamazoe. “New approaches for improving semiconductor gas sensors”. In: *Sensors and Actuators B: Chemical* 5.1 (1991), pp. 7–19.

[40] S. Strassler and A. Reis. “Simple models for N-type metal oxide gas sensors”. In: *Sensors and Actuators* 4 (1983), pp. 465–472.

[41] H. Windischmann and P. Mark. “A Model for the Operation of a Thin-Film SnOx Conductance-Modulation Carbon Monoxide Sensor”. In: *Journal of The Electrochemical Society* 126.4 (1979), pp. 627–633.

[42] N. Barsan and U. Weimar. “Conduction Model of Metal Oxide Gas Sensors”. English. In: *Journal of Electroceramics* 7.3 (2001), pp. 143–167.

[43] Y. Mizokawa and S. Nakamura. “ESR and electric conductance studies of the fine-powdered SnO_2”. In: *Japanese Journal of Applied Physics* 14.6 (1975), p. 779.

[44] N. Barsan. “Conduction models in gas-sensing SnO_2 layers: grain-size effects and ambient atmosphere influence”. In: *Sensors and Actuators B: Chemical* 17.3 (1994), pp. 241–246.

[45] J. Rebholz, P. Bonanati, U. Weimar, and N. Barsan. “Grain shape influence on semiconducting metal oxide based gas sensor performance: modeling versus experiment”. In: *Analytical and Bioanalytical Chemistry* 406.16 (2014), pp. 3977–3983.

[46] M. Hübner, C. Simion, A. Tomescu-Stanoiu, S. Pokhrel, N. Barsan, and U. Weimar. “Influence of humidity on CO sensing with p-type CuO thick film gas sensors”. In: *Sensors and Actuators B: Chemical* 153.2 (2011), pp. 347–353.

[47] D. Kohl. “Surface processes in the detection of reducing gases with SnO_2-based devices”. In: *Sensors and actuators* 18.1 (1989), pp. 71–113.

[48] W. Schmid. “Consumption measurement on SnO_2 sensors”. PhD thesis. Eberhard-Karls-Universität Tübingen, 2004.

[49] M. Batzill and U. Diebold. “The surface and materials science of tin oxide”. In: *Progress in Surface Science* 79.2–4 (2005), pp. 47–154.

[50] N. Barsan, C. Simion, T. Heine, S. Pokhrel, and U. Weimar. “Modeling of sensing and transduction for p-type semiconducting metal oxide based gas sensors”. In: *Journal of Electroceramics* 25.1 (2010), pp. 11–19.

[51] N. Barsan, M. Hübner, and U. Weimar. “Conduction mechanisms in SnO_2 based polycrystalline thick film gas sensors exposed to CO and H_2 in different oxygen backgrounds”. In: *Sensors and Actuators B: Chemical* 157.2 (2011), pp. 510–517.

[52] N. Barsan, J. Rebholz, and U. Weimar. “Conduction mechanism switch for SnO_2 based sensors during operation in application relevant conditions; implications for modeling of sensing”. In: *Sensors and Actuators B: Chemical* 207, Part A (2015), pp. 455–459.

[53] A. Gurlo, N. Barsan, A. Oprea, M. Sahm, T. Sahm, and U. Weimar. "An n- to p-type conductivity transition induced by oxygen adsorption on Fe_2O_3". In: *Applied Physics Letters* 85.12 (2004), pp. 2280–2282.

[54] M. Huebner, R. Pavelko, N. Barsan, and U. Weimar. "Influence of oxygen backgrounds on hydrogen sensing with SnO_2 nanomaterials". In: *Sensors and Actuators B: Chemical* 154.2 (2011). EUROSENSORS XXIII, pp. 264–269.

[55] A. Gurlo and R. Riedel. "In-situ- und Operando-Spektroskopie zur Untersuchung von Mechanismen der Gaserkennung". In: *Angewandte Chemie* 119.21 (2007), pp. 3900–3923.

[56] J.-M. Ducéré, A. Hemeryck, A. Estève, M. D. Rouhani, G. Landa, P. Ménini, C. Tropis, A. Maisonnat, P. Fau, and B. Chaudret. "A computational chemist approach to gas sensors: Modeling the response of SnO_2 to CO, O_2, and H_2O Gases". In: *Journal of Computational Chemistry* 33.3 (2012), pp. 247–258.

[57] D. Degler, S. Wicker, U. Weimar, and N. Barsan. "Identifying the Active Oxygen Species in SnO_2 Based Gas Sensing Materials: An Operando IR Spectrsocopy Study". In: *The Journal of Physical Chemistry C* 119.21 (2015), pp. 11792–11799.

[58] X. Wang, H. Qin, Y. Chen, and J. Hu. "Sensing Mechanism of SnO_2 (110) Surface to CO: Density Functional Theory Calculations". In: *The Journal of Physical Chemistry C* 118.49 (2014), pp. 28548–28561.

[59] S. Hahn, N. Barsan, U. Weimar, S. Ejakov, J. Visser, and R. Soltis. "CO sensing with SnO_2 thick film sensors: role of oxygen and water vapour". In: *Thin Solid Films* 436.1 (2003). Papers from the 3rd International Seminar on Semiconductor Gas Sensors, pp. 17–24.

[60] M. Hübner, C. Simion, A. Haensch, N. Barsan, and U. Weimar. "CO sensing mechanism with WO_3 based gas sensors". In: *Sensors and Actuators B: Chemical* 151.1 (2010), pp. 103–106.

[61] G. Heiland and D. Kohl. "Physical and Chemical Aspects of Oxidic Semiconductor Gas Sensors". In: *Chemical Sensor Technology*. Ed. by T. SEIYAMA. Chemical Sensor Technology. Amsterdam: Elsevier, 1988, pp. 15–38.

[62] T. Sahm, A. Gurlo, N. Barsan, U. Weimar, and L. Mädler. "Fundamental studies on SnO_2 by means of simultaneous work function change and conduction measurements". In: *Thin Solid Films* 490.1 (2005). Proceedings of the 4th International Workshop on Semiconductor Gas Sensors (SGS 2004), pp. 43–47.

[63] K. Schierbaum, U. Weimar, W. Göpel, and R. Kowalkowski. “Conductance, work function and catalytic activity of SnO_2-based gas sensors”. In: *Sensors and Actuators B: Chemical* 3.3 (1991), pp. 205–214.

[64] A. Gurlo, N. Barsan, M. Ivanovskaya, U. Weimar, and W. Göpel. “In_2O_3 and MoO_3-In_2O_3 thin film semiconductor sensors: interaction with NO_2 and O_3”. In: *Sensors and Actuators B: Chemical* 47.1–3 (1998), pp. 92–99.

[65] B. Ruhland, T. Becker, and G. Müller. “Gas-kinetic interactions of nitrous oxides with SnO_2 surfaces”. In: *Sensors and Actuators B: Chemical* 50.1 (1998), pp. 85–94.

[66] I. Sayago, J. Gutie, L. Are, J. Robla, M. Horrillo, J. Getino, J. Agapito, et al. “The interaction of different oxidizing agents on doped tin oxide”. In: *Sensors and Actuators B: Chemical* 25.1-3 (1995), pp. 512–515.

[67] E. Leblanc, L. Périer-Camby, G. Thomas, R. Gibert, M. Primet, and P. Gelin. “NOx adsorption onto dehydroxylated or hydroxylated tin dioxide surface. Application to SnO_2-based sensors”. In: *Sensors and Actuators B: Chemical* 62.1 (2000), pp. 67–72.

[68] D. Koziej, M. Hubner, N. Barsan, U. Weimar, M. Sikora, and J.-D. Grunwaldt. “Operando X-ray absorption spectroscopy studies on Pd-SnO_2 based sensors”. In: *Physical Chemistry Chemical Physics* 11 (2009), pp. 8620–8625.

[69] S. Harbeck. “Schwingungspektroskopische Charakterisierung der Funktionsweise von SnO_2-Sensoren”. PhD thesis. Eberhard-Karls-Universität Tübingen, 2005.

[70] J. A. Kemmler, S. Pokhrel, L. Mädler, U. Weimar, and N. Barsan. “Flame spray pyrolysis for sensing at the nanoscale”. In: *Nanotechnology* 24.44 (2013), p. 442001.

[71] R. H. Castro, P. Hidalgo, R. Muccillo, and D. Gouvea. “Microstructure and structure of NiO-SnO_2 and Fe_2O_3-SnO_2 systems”. In: *Applied Surface Science* 214.1–4 (2003), pp. 172–177.

[72] M. Huebner, D. Koziej, J.-D. Grunwaldt, U. Weimar, and N. Barsan. “An Au clusters related spill-over sensitization mechanism in SnO_2-based gas sensors identified by operando HERFD-XAS, work function changes, DC resistance and catalytic conversion studies”. In: *Physical Chemistry Chemical Physics* 14 (2012), pp. 13249–13254.

[73] M. Hübner, D. Koziej, M. Bauer, N. Barsan, K. Kvashnina, M. D. Rossell, U. Weimar, and J.-D. Grunwaldt. "The Structure and Behavior of Platinum in SnO_2-Based Sensors under Working Conditions". In: *Angewandte Chemie International Edition* 50.12 (2011), pp. 2841–2844.

[74] D. Degler, H. W. P. de Carvalho, U. Weimar, N. Barsan, D. Pham, L. Maedler, and J.-D. Grunwaldt. "Structure–function relationships of conventionally and flame made Pd-doped sensors studied by X-ray absorption spectroscopy and DC-resistance". In: *Sensors and Actuators B: Chemical* 219 (2015), pp. 315–323.

[75] A. Cabot, A. Dieguez, A. Romano-Rodriguez, J. Morante, and N. Barsan. "Influence of the catalytic introduction procedure on the nano-SnO_2 gas sensor performances: Where and how stay the catalytic atoms?" In: *Sensors and Actuators B: Chemical* 79.2–3 (2001), pp. 98–106.

[76] G. Advani, Y. Komem, J. Hasenkopf, and A. Jordan. "Improved performance of SnO_2 thin-film gas sensors due to gold diffusion". In: *Sensors and Actuators* 2 (1981), pp. 139–147.

[77] Y. Suda, H. Kawasaki, J. Namba, K. Iwatsuji, K. Doi, and K. Wada. "Properties of palladium doped tin oxide thin films for gas sensors grown by PLD method combined with sputtering process". In: *Surface and Coatings Technology* 174–175 (2003). Proceedings of the Eight International Conference on Plasma Surface Engineering, pp. 1293–1296.

[78] G. Sulz, G. Kuehner, H. Reiter, G. Uptmoor, W. Schweizer, H. Löw, M. Lacher, and K. Steiner. "Ni, In and Sb implanted Pt and V catalysed thin-film SnO_2 gas sensors". In: *Sensors and Actuators B: Chemical* 16 (1993), pp. 390–395.

[79] A. Galdikas, V. Jasutis, S. Kaciulis, G. Mattogno, A. Mironas, V. Olevano, D. Senuliene, and A. Setkus. "Peculiarities of surface doping with Cu in SnO_2 thin film gas sensors". In: *Sensors and Actuators B: Chemical* 43 (1997), pp. 140–146.

[80] W. J. Moon, J. H. Yu, and G. M. Choi. "The CO and H_2 gas selectivity of CuO-doped SnO_2:ZnO composite gas sensor". In: *Sensors and Actuators B: Chemical* 87.3 (2002), pp. 464–470.

[81] J. H. Yu and G. M. Choi. "Selective CO gas detection of CuO- and ZnO-doped SnO_2 gas sensor". In: *Sensors and Actuators B: Chemical* 75 (2001), pp. 56–61.

[82] H. Gong, J. Hu, J. Wang, C. Ong, and F. Zhu. “Nano-crystalline Cu-doped ZnO thin film gas sensor for CO”. In: *Sensors and Actuators B: Chemical* 115.1 (2006), pp. 247–251.

[83] G. Tulzer, S. Baumgartner, E. Brunet, G. C. Mutinati, S. Steinhauer, A. Köck, P. E. Barbano, and C. Heitzinger. “Kinetic parameter estimation and fluctuation analysis of CO at SnO_2 single nanowires”. In: *Nanotechnology* 24.31 (2013), p. 315501.

[84] N. P. Benner. “Präparation und Optimierung von SnO_2-Schichten und deren Reaktivität”. PhD thesis. Justus-Liebig-Universität Giessen, 2004.

[85] T. Wagner, C.-D. Kohl, M. Fröba, and M. Tiemann. “Gas Sensing Properties of Ordered Mesoporous SnO_2”. In: *Sensors* 6.4 (2006), pp. 318–323.

[86] H. Yamaura, J. Tamaki, K. Moriya, N. Miura, and N. Yamazoe. “Highly Selective CO Sensor Using Indium Oxide Doubly Promoted by Cobalt Oxide and Gold”. In: *Journal of The Electrochemical Society* 144.6 (1997), pp. L158–L160.

[87] E. Comini, G. Faglia, G. Sberveglieri, C. Cantalini, M. Passacantando, S. Santucci, Y. Li, W. Wlodarski, and W. Qu. “Carbon monoxide response of molybdenum oxide thin films deposited by different techniques”. In: *Sensors and Actuators B: Chemical* 68.1–3 (2000), pp. 168–174.

[88] J. Wang, X. Sun, H. Huang, Y. Lee, O. Tan, M. Yu, G. Lo, and D. Kwong. “A two-step hydrothermally grown ZnO microtube array for CO gas sensing”. English. In: *Applied Physics A* 88.4 (2007), pp. 611–615.

[89] K.-I. Choi, M. Hübner, A. Haensch, H.-J. Kim, U. Weimar, N. Barsan, and J.-H. Lee. “Ambivalent effect of Ni loading on gas sensing performance in SnO_2 based gas sensor”. In: *Sensors and Actuators B: Chemical* 183 (2013), pp. 401–410.

[90] O. Wurzinger and G. Reinhardt. “CO-sensing properties of doped SnO_2 sensors in H_2-rich gases”. In: *Sensors and Actuators B: Chemical* 103 (2004). The 17th Euopean Conference on Solid-State Transducers, University of Minho, Guimares, Portugal, September 21-24, 2003, pp. 104–110.

[91] N. Barsan and U. Weimar. “Understanding the fundamental principles of metal oxide based gas sensors; the example of CO sensing with SnO_2 sensors in the presence of humidity”. In: *Journal of Physics: Condensed Matter* 15.20 (2003), R813.

[92] R. Dolbec, M. E. Khakani, A. Serventi, and R. Saint-Jacques. “Influence of the nanostructural characteristics on the gas sensing properties of pulsed laser deposited tin oxide thin films”. In: *Sensors and Actuators B: Chemical* 93 (2003). Proceedings of the Ninth International Meeting on Chemical Sensors, pp. 566–571.

[93] M. E. Khakani, R. Dolbec, A. Serventi, M. Horrillo, M. Trudeau, R. Saint-Jacques, D. Rickerby, and I. Sayago. “Pulsed laser deposition of nanostructured tin oxide films for gas sensing applications”. In: *Sensors and Actuators B: Chemical* 77 (2001). Proceeding of the Eighth International Meeting on Chemical Sensors IMCS-8 - Part 2, pp. 383–388.

[94] A. Galdikas, S. Grebinskij, A. Mironas, H. Tvardauskas, et al. “Gas-sensing properties of chemically deposited SnOx films doped with Pt and Sb”. In: *Sensors and Actuators B: Chemical* 17.1 (1993), pp. 27–33.

[95] S. Nicoletti, S. Zampolli, I. Elmi, L. Dori, and M. Severi. “Use of different sensing materials and deposition techniques for thin-film sensors to increase sensitivity and selectivity”. In: *Sensors Journal, IEEE* 3.4 (2003), pp. 454–459.

[96] J. Chang, H. Kuo, I. Leu, and M. Hon. “The effects of thickness and operation temperature on ZnO:Al thin film CO gas sensor”. In: *Sensors and Actuators B: Chemical* 84.2–3 (2002), pp. 258–264.

[97] I. Karkkanen, M. Kodu, T. Avarmaa, J. Kozlova, L. Matisen, H. Mandar, A. Saar, V. Sammelselg, and R. Jaaniso. “Sensitivity of $CoWO_4$ thin films to CO”. In: vol. 5. 2010, pp. 160–163.

[98] K. Kim, Y.-W. Song, S. Chang, I.-H. Kim, S. Kim, and S. Y. Lee. “Fabrication and characterization of Ga-doped ZnO nanowire gas sensor for the detection of CO”. In: *Thin Solid Films* 518.4 (2009). Transparent Conductive Oxides, pp. 1190–1193.

[99] G. Sberveglieri, G. Faglia, S. Groppelli, and P. Nelli. “Methods for the preparation of NO, NO_2 and H_2 sensors based on tin oxide thin films, grown by means of the r.f. magnetron sputtering technique”. In: *Sensors and Actuators B: Chemical* 8.1 (1992), pp. 79–88.

[100] I. Simon. *Thermal Conductivity and Metal Oxide Gas Sensors: Micromachining as an Opportunity to Improve Sensor Performance (Berichte Aus Der Mikromechanik)*. Shaker Verlag GmbH, Germany, 2004.

[101] T. Seiyama and A. Kato. “A new detector for gaseous components using semiconductor thin film”. In: *Anal. Chem* 34.11 (1962), pp. 1502–1503.

[102] K. Schierbaum, S. Vaihinger, W. Göpel, H. van den Vlekkert, B. Kloeck, and N. de Rooij. “Prototype structure for systematic investigations of thin-film gas sensors”. In: *Sensors and Actuators B: Chemical* 1.1–6 (1990), pp. 171–175.

[103] C. Cantalini, M. Pelino, H. Sun, M. Faccio, S. Santucci, L. Lozzi, and M. Passacantando. “Cross sensitivity and stability of NO_2 sensors from WO_3 thin film”. In: *Sensors and Actuators B: Chemical* 35.1–3 (1996). Proceedings of the Sixth International Meeting on Chemical Sensors, pp. 112–118.

[104] M. Schweizer-Berberich, J. Zheng, U. Weimar, W. Göpel, N. Barsan, E. Pentia, and A. Tomescu. “The effect of Pt and Pd surface doping on the response of nanocrystalline tin dioxide gas sensors to CO”. In: *Sensors and Actuators B: Chemical* 31.1–2 (1996). Materials for Sensors: Functional Nanoscaled Structures of the 1995 E-MRS Spring Conference, pp. 71–75.

[105] Y. Shimizu, S. Karino, Y. Takao, T. Hyodo, K. Baba, and M. Egashira. “Improvement of Long-Term Stability of Thin Film Gas Sensors by Ion Beam-Assisted Deposition”. In: *Journal of The Electrochemical Society* 147.11 (2000), pp. 4379–4384.

[106] G. Sberveglieri. “Recent developments in semiconducting thin-film gas sensors”. In: *Sensors and Actuators B: Chemical* 23.2–3 (1995). The workshop on new developments in semiconducting gas sensors, pp. 103–109.

[107] G. Faglia, E. Comini, A. Cristalli, G. Sberveglieri, and L. Dori. “Very low power consumption micromachined CO sensors”. In: *Sensors and Actuators B: Chemical* 55.2–3 (1999), pp. 140–146.

[108] A. Dieguez, A. Romano-Rodriguez, J. Morante, L. Sangaletti, L. Depero, E. Comini, G. Faglia, and G. Sberveglieri. “Influence of the completion of oxidation on the long-term response of RGTO SnO_2 gas sensors”. In: *Sensors and Actuators B: Chemical* 66.1–3 (2000), pp. 40–42.

[109] G. Korotcenkov. “Gas response control through structural and chemical modification of metal oxide films: state of the art and approaches”. In: *Sensors and Actuators B: Chemical* 107.1 (2005). Proceedings of the 7th European Conference on Optical Chemical Sensors and Biosensors EUROPT(R)ODE VII, pp. 209–232.

[110] S. M. George. “Atomic Layer Deposition: An Overview”. In: *Chemical Reviews* 110.1 (2010), pp. 111–131.

[111] A. Rosental, A. Tarre, A. Gerst, J. Sundqvist, A. Harsta, A. Aidla, J. Aarik, V. Sammelselg, and T. Uustare. “Gas sensing properties of epitaxial SnO_2 thin films prepared by atomic layer deposition”. In: *Sensors and Actuators B: Chemical* 93.1–3 (2003). Proceedings of the Ninth International Meeting on Chemical Sensors, pp. 552–555.

[112] X. Du and S. George. “Thickness dependence of sensor response for CO gas sensing by tin oxide films grown using atomic layer deposition”. In: *Sensors and Actuators B: Chemical* 135.1 (2008), pp. 152–160.

[113] G. Sberveglieri. “Classical and novel techniques for the preparation of SnO_2 thin-film gas sensors”. In: *Sensors and Actuators B: Chemical* 6.1 (1992), pp. 239–247.

[114] S.-C. Chang. “Thin-film semiconductor NOx sensor”. In: *IEEE Transactions on Electron Devices* 26.12 (1979), pp. 1875–1880.

[115] I. Simon, N. Barsan, M. Bauer, and U. Weimar. “Micromachined metal oxide gas sensors: opportunities to improve sensor performance”. In: *Sensors and Actuators B: Chemical* 73.1 (2001), pp. 1–26.

[116] FIS Inc. *Ozone Sensor Module SP-61 Datasheet*. 3-36-3 Kitazono, Japan.

[117] K. Schierbaum, U. Weimar, and W. Göpel. “Comparison of ceramic, thick-film and thin-film chemical sensors based upon SnO_2”. In: *Sensors and Actuators B: Chemical* 7.1–3 (1992), pp. 709–716.

[118] T. Sauerwald, M. Afshar, M. Rodner, E. Preiß, D. Feili, H. Seidel, and A. Schütze. “Stickoxidsensor aus einem einzelnen Indium Zinnoxid (ITO) Nanodraht”. In: *11. Dresdner Sensor Symposium*. 2013.

[119] M. Afshar, E. M. Preiß, T. Sauerwald, M. Rodner, D. Feili, M. Straub, K. König, A. Schütze, and H. Seidel. “Indium-tin-oxide single-nanowire gas sensor fabricated via laser writing and subsequent etching”. In: *Sensors and Actuators B: Chemical* 215 (2015), pp. 525–535.

[120] J. Santos, P. Serrini, B. O’Beirn, and L. Manes. “A thin film SnO_2 gas sensor selective to ultra-low NO_2 concentrations in air”. In: *Sensors and Actuators B: Chemical* 43.1–3 (1997), pp. 154–160.

[121] A. Sharma, M. Tomar, and V. Gupta. “SnO_2 thin film sensor with enhanced response for NO_2 gas at lower temperatures”. In: *Sensors and Actuators B: Chemical* 156.2 (2011), pp. 743–752.

[122] A. Sharma, M. Tomar, and V. Gupta. “Enhanced response characteristics of SnO_2 thin film based NO_2 gas sensor integrated with nanoscaled metal oxide clusters”. In: *Sensors and Actuators B: Chemical* 181 (2013), pp. 735–742.

[123] V. Demarne, A. Grisel, R. Sanjines, D. Rosenfeld, and F. Levy. “Electrical transport properties of thin polycrystalline SnO_2 film sensors”. In: *Sensors and Actuators B: Chemical* 7.1 (1992), pp. 704–708.

[124] H. Steffes, C. Imawan, P. Fricke, H. Vöhse, J. Albrecht, R. Schneider, F. Solzbacher, and E. Obermeier. “New $In_xO_yN_z$ films for the application in NO_2 sensors”. In: *Sensors and Actuators B: Chemical* 77.1–2 (2001). Proceeding of the Eighth International Meeting on Chemical Sensors IMCS-8 - Part 2, pp. 352–358.

[125] H. Steffes and E. Obermeier. “$In_xO_yN_z$ films with a Ta_2O_5 promoter for the detection of CO, H_2, and CH_4”. In: *Sensors and Actuators B: Chemical* 95.1–3 (2003). Selected Papers from Eurosensors XVI, pp. 252–257.

[126] C. Papadopoulos, D. Vlachos, and J. Avaritsiotis. “Comparative study of various metal-oxide-based gas-sensor architectures”. In: *Sensors and Actuators B: Chemical* 32.1 (1996), pp. 61–69.

[127] S. Rembeza, E. Rembeza, T. Svistova, and O. Borsiakova. “Electrical Resistivity and Gas Response Mechanisms of Nanocrystalline SnO_2 Films in a Wide Temperature Range”. In: *physica status solidi (a)* 179.1 (2000), pp. 147–152.

[128] J. Wöllenstein, H. Böttner, M. Jaegle, W. Becker, and E. Wagner. “Material properties and the influence of metallic catalysts at the surface of highly dense SnO_2 films”. In: *Sensors and Actuators B: Chemical* 70.1–3 (2000). Special Issue in Memory of Professor Wolfgang Gopel, pp. 196–202.

[129] S. Kim, K. Lee, S. Lee, J. Moon, and B.-T. Lee. “Effects of Pt/Pd Co-Doping on the Sensitivity of SnO_2 Thin Film Sensors”. In: *Japanese Journal of Applied Physics* 41.9A (2002), p. L1002.

[130] D. Haridas, V. Gupta, and K. Sreenivas. “Enhanced catalytic activity of nanoscale platinum islands loaded onto SnO_2 thin film for sensitive LPG gas sensors”. In: *Bulletin of Materials Science* 31.3 (2008), pp. 397–400.

[131] D. Haridas and V. Gupta. “Enhanced response characteristics of SnO_2 thin film based sensors loaded with Pd clusters for methane detection”. In: *Sensors and Actuators B: Chemical* 166–167 (2012), pp. 156–164.

[132] J. Wöllenstein, M. Burgmair, G. Plescher, T. Sulima, J. Hildenbrand, H. Böttner, and I. Eisele. “Cobalt oxide based gas sensors on silicon substrate for operation at low temperatures”. In: *Sensors and Actuators B: Chemical* 93.1–3 (2003). Proceedings of the Ninth International Meeting on Chemical Sensors, pp. 442–448.

[133] A. Bejaoui, J. Guerin, J. Zapien, and K. Aguir. “Theoretical and experimental study of the response of CuO gas sensor under ozone”. In: *Sensors and Actuators B: Chemical* 190 (2014), pp. 8–15.

[134] C. Baratto, R. Kumar, G. Faglia, K. Vojisavljevic, and B. Malic. “p-Type copper aluminum oxide thin films for gas-sensing applications”. In: *Sensors and Actuators B: Chemical* 209 (2015), pp. 287–296.

[135] E. Traversa, S. Matsushima, G. Okada, Y. Sadaoka, Y. Sakai, and K. Watanabe. “NO_2 sensitive $LaFeO_3$ thin films prepared by r.f. sputtering”. In: *Sensors and Actuators B: Chemical* 25.1–3 (1995). Proceedings of the Fifth International Meeting on Chemical Sensors, pp. 661–664.

[136] M. Ferroni, V. Guidi, G. Martinelli, P. Nelli, M. Sacerdoti, and G. Sberveglieri. “Characterization of a molybdenum oxide sputtered thin film as a gas sensor”. In: *Thin Solid Films* 307.1–2 (1997), pp. 148–151.

[137] M. S. Aleksanyan, V. M. Arakelyan, V. M. Aroutiounian, and G. E. Shahnazaryan. “Investigation of gas sensor based on In_2O_3:Ga_2O_3 film”. In: *Journal of Contemporary Physics (Armenian Academy of Sciences)* 46.2 (2011), pp. 86–92.

[138] G. Kiriakidis, K. Moschovis, I. Kortidis, and V. Binas. “Ultra-low gas sensing utilizing metal oxide thin films”. In: *Vacuum* 86.5 (2012). Special Issue: Sensors, pp. 495–506.

[139] C. Cantalini, W. Wlodarski, Y. Li, M. Passacantando, S. Santucci, E. Comini, G. Faglia, and G. Sberveglieri. “Investigation on the O_3 sensitivity properties of WO_3 thin films prepared by sol-gel, thermal evaporation and r.f. sputtering techniques”. In: *Sensors and Actuators B: Chemical* 64.1–3 (2000), pp. 182–188.

[140] Y. Ishikawa and K. Hara. “Thin-film gas sensors operating in a perpendicular current mode”. In: *Sensors and Actuators B: Chemical* 181 (2013), pp. 932–937.

[141] Y. Min, H. L. Tuller, S. Palzer, J. Wöllenstein, and H. Böttner. “Gas response of reactively sputtered ZnO films on Si-based micro-array”. In: *Sensors and Actuators B: Chemical* 93.1–3 (2003). Proceedings of the Ninth International Meeting on Chemical Sensors, pp. 435–441.

[142] A. Tischner, T. Maier, C. Stepper, and A. Köck. "Ultrathin SnO_2 gas sensors fabricated by spray pyrolysis for the detection of humidity and carbon monoxide". In: *Sensors and Actuators B: Chemical* 134.2 (2008), pp. 796–802.

[143] G. Korotcenkov, V. Brinzari, J. Schwank, M. DiBattista, and A. Vasiliev. "Peculiarities of SnO_2 thin film deposition by spray pyrolysis for gas sensor application". In: *Sensors and Actuators B: Chemical* 77.1–2 (2001). Proceeding of the Eighth International Meeting on Chemical Sensors IMCS-8 - Part 2, pp. 244–252.

[144] L. Mädler, T. Sahm, A. Gurlo, J.-D. Grunwaldt, N. Barsan, U. Weimar, and S. Pratsinis. "Sensing low concentrations of CO using flame-spray-made Pt/SnO_2 nanoparticles". In: *Journal of Nanoparticle Research* 8.6 (2006), pp. 783–796.

[145] J. Rebholz, P. Bonanati, C. Jaeschke, M. Hübner, L. Mädler, U. Weimar, and N. Barsan. "Conduction mechanism in undoped and antimony doped SnO_2 based FSP gas sensors". In: *Sensors and Actuators B: Chemical* 188 (2013), pp. 631–636.

[146] C. Wang. "Metal organic chemical vapor deposition of indium oxide for ozone sensing". PhD thesis. Albert-Ludwigs-Universität Freiburg i. Br., 2009.

[147] T. Oyabu. "Sensing characteristics of SnO_2 thin film gas sensor". In: *Journal of Applied Physics* 53.4 (1982), pp. 2785–2787.

[148] C.-H. Shim, D.-S. Lee, S.-I. Hwang, M.-B. Lee, J.-S. Huh, and D.-D. Lee. "Gas sensing characteristics of SnO_2 thin film fabricated by thermal oxidation of a Sn/Pt double layer". In: *Sensors and Actuators B: Chemical* 81.2–3 (2002), pp. 176–181.

[149] A. Khanna, R. Kumar, and S. S. Bhatti. "CuO-doped SnO_2 thin films as hydrogen sulfide gas sensor". In: *Applied Physics Letters* 82.24 (2003), pp. 4388–4390.

[150] D. J. Yoo, J. Tamaki, S. J. Park, N. Miura, and N. Yamazoe. "Effects of Thickness and Calcination Temperature on Tin Dioxide Sol-Derived Thin-Film Sensor". In: *Journal of the Electrochemical Society* 142.7 (1995), pp. L105–L107.

[151] O. K. Varghese and L. Malhotra. "Electrode-sample capacitance effect on Ethanol sensitivity of nano-grained SnO_2 thin films". In: *Sensors and Actuators B: Chemical* 53.1–2 (1998), pp. 19–23.

[152] P. Siciliano. “Preparation, characterisation and applications of thin films for gas sensors prepared by cheap chemical method”. In: *Sensors and Actuators B: Chemical* 70.1–3 (2000). Special Issue in Memory of Professor Wolfgang Göpel, pp. 153–164.

[153] G. Korotchenkov, V. Brynzari, and S. Dmitriev. “Electrical behavior of SnO_2 thin films in humid atmosphere”. In: *Sensors and Actuators B: Chemical* 54.3 (1999), pp. 197–201.

[154] G. Korotcenkov and B. Cho. “Thin film SnO_2-based gas sensors: Film thickness influence”. In: *Sensors and Actuators B: Chemical* 142.1 (2009), pp. 321–330.

[155] G. Korotcenkov, I. Boris, V. Brinzari, S. Han, and B. Cho. “The role of doping effect on the response of SnO_2-based thin film gas sensors: Analysis based on the results obtained for Co-doped SnO_2 films deposited by spray pyrolysis”. In: *Sensors and Actuators B: Chemical* 182 (2013), pp. 112–124.

[156] M. Munji, P. Mwathe, R. Musembi, B. Odari, L. Munguti, A. A. Ntilakigwa, J. Mwabora, W. Njoroge, B. Aduda, and B. Muthoka. “Surface passivation effect on CO_2 sensitivity of spray pyrolysis deposited Pd-F: SnO_2 thin film gas sensor”. In: *Advances in Materials* (2014).

[157] S. W. Lee, P. P. Tsai, and H. Chen. “Comparison study of SnO_2 thin- and thick-film gas sensors”. In: *Sensors and Actuators B: Chemical* 67.1–2 (2000), pp. 122–127.

[158] A. Rosental, A. Tarre, A. Gerst, T. Uustare, and V. Sammelselg. “Atomic-layer chemical vapor deposition of SnO_2 for gas-sensing applications”. In: *Sensors and Actuators B: Chemical* 77.1–2 (2001). Proceeding of the Eighth International Meeting on Chemical Sensors IMCS-8 - Part 2, pp. 297–300.

[159] D. Dijkkamp, T. Venkatesan, X. D. Wu, S. A. Shaheen, N. Jisrawi, Y. H. Min-Lee, W. L. McLean, and M. Croft. “Preparation of Y-Ba-Cu oxide superconductor thin films using pulsed laser evaporation from high T_c bulk material”. In: *Applied Physics Letters* 51.8 (1987), pp. 619–621.

[160] D. H. Lowndes, D. B. Geohegan, A. A. Puretzky, D. P. Norton, and C. M. Rouleau. “Synthesis of Novel Thin-Film Materials by Pulsed Laser Deposition”. In: *Science* 273.5277 (1996), pp. 898–903.

[161] E. Vasco and J. L. Sacedón. “Role of Cluster Transient Mobility in Pulsed Laser Deposition-Type Growth Kinetics”. In: *Phys. Rev. Lett.* 98 (3 2007), p. 036104.

[162] R. Eason. *Pulsed laser deposition of thin films: applications-led growth of functional materials*. John Wiley & Sons, 2007.

[163] C. Kim, S. Choi, I. Noh, J. Lee, C. Hong, H. Chae, G. Jang, and H. Park. "A study on thin film gas sensor based on SnO_2 prepared by pulsed laser deposition method". In: *Sensors and Actuators B: Chemical* 77 (2001). Proceeding of the Eighth International Meeting on Chemical Sensors IMCS-8 - Part 2, pp. 463–467.

[164] T. Ohgaki, R. Matsuoka, K. Watanabe, K. Matsumoto, Y. Adachi, I. Sakaguchi, S. Hishita, N. Ohashi, and H. Haneda. "Synthesizing SnO_2 thin films and characterizing sensing performances". In: *Sensors and Actuators B: Chemical* 150.1 (2010), pp. 99–104.

[165] S. Henley, M. Ashfold, and D. Cherns. "The growth of transparent conducting ZnO films by pulsed laser ablation". In: *Surface and Coatings Technology* 177–178 (2004). Proceedings of the 30th International Conference on Metallurgical Coatings and Thin Films, pp. 271–276.

[166] R. Dolbec and M. A. E. Khakani. "Sub-ppm sensitivity towards carbon monoxide by means of pulsed laser deposited SnO_2:Pt based sensors". In: *Applied Physics Letters* 90.17, 173114 (2007), p. 173114.

[167] Z. Chen, J. Lai, C. Shek, and H. Chen. "Nucleation and growth of SnO_2 nanocrystallites prepared by pulsed laser deposition". In: *Applied Physics A* 81.5 (2005), pp. 959–962.

[168] A. Pereira, L. Cultrera, A. Dima, M. Susu, A. Perrone, H. Du, A. Volkov, R. Cutting, and P. Datta. "Pulsed laser deposition and characterization of textured Pd-doped-SnO_2 thin films for gas sensing applications". In: *Thin Solid Films* 497 (2006), pp. 142–148.

[169] W. T. Silfvast. *Laser fundamentals*. Cambridge University Press, 2004.

[170] R. K. Singh and J. Narayan. "Pulsed-laser evaporation technique for deposition of thin films: Physics and theoretical model". In: *Physical Review B* 41 (1990), pp. 8843–8859.

[171] M. N. R. Ashfold, F. Claeyssens, G. M. Fuge, and S. J. Henley. "Pulsed laser ablation and deposition of thin films". In: *Chemical Society Reviews* 33 (2004), pp. 23–31.

[172] M. Stafe, A. Marcu, and N. Puscas. *Pulsed Laser Ablation of Solids*. Vol. 53. Springer-Verlag Berlin Heidelberg, 2014.

[173] D. Chrisey. *Pulsed laser deposition of thin films*. New York: J. Wiley, 1994.

[174] A. Infortuna, A. Harvey, and L. Gauckler. “Microstructures of CGO and YSZ thin films by pulsed laser deposition”. In: *Advanced Functional Materials* 18.1 (2008). cited By 105, pp. 127–135.

[175] J. A. Thornton. “Influence of apparatus geometry and deposition conditions on the structure and topography of thick sputtered coatings”. In: *Journal of Vacuum Science & Technology* 11.4 (1974), pp. 666–670.

[176] J. A. Thornton. “High Rate Thick Film Growth”. In: *Annual Review of Materials Science* 7.1 (1977), pp. 239–260.

[177] C. M. Dai, C. S. Su, and D. S. Chuu. “Growth of highly oriented tin oxide thin films by laser evaporation deposition”. In: *Applied Physics Letters* 57.18 (1990), pp. 1879–1881.

[178] W. Hu, Z. Liu, Z. Wu, and D. Feng. “Comparative study of laser ablation techniques for fabricating nanocrystalline SnO_2 thin films for sensors”. In: *Materials Letters* 28.4–6 (1996), pp. 369–372.

[179] S. Nicoletti, L. Dori, F. Corticelli, M. Leoni, and P. Scardi. “Tin Oxide Thin-Film Sensors for Aromatic Hydrocarbons Detection: Effect of Aging Time on Film Microstructure”. In: *Journal of the American Ceramic Society* 82.5 (1999), pp. 1201–1206.

[180] Y. Zhao, Z. Feng, and Y. Liang. “SnO_2 gas sensor films deposited by pulsed laser ablation”. In: *Sensors and Actuators B: Chemical* 56.3 (1999), pp. 224–227.

[181] R. Khandelwal, A. P. Singh, A. Kapoor, S. Grigorescu, P. Miglietta, N. E. Stankova, and A. Perrone. “Effects of deposition temperature on the structural and morphological properties of SnO_2 films fabricated by pulsed laser deposition”. In: *Optics & Laser Technology* 41.1 (2009), pp. 89–93.

[182] C. Ristoscu, L. Cultrera, A. Dima, A. Perrone, R. Cutting, H. Du, A. Busiakiewicz, Z. Klusek, P. Datta, and S. Rose. “SnO_2 nanostructured films obtained by pulsed laser ablation deposition”. In: *Applied Surface Science* 247.1–4 (2005). Proceedings of the European Materials Research Society 2004 - Symposium NEMRS-2004EMRS Symposium N 2004, pp. 95–100.

[183] R. Dolbec, M. E. Khakani, A. Serventi, M. Trudeau, and R. Saint-Jacques. “Microstructure and physical properties of nanostructured tin oxide thin films grown by means of pulsed laser deposition”. In: *Thin Solid Films* 419.1–2 (2002), pp. 230–236.

[184] L. Tien, S. Pearton, D. Norton, and F. Ren. "Synthesis and characterization of single crystalline SnO_2 nanorods by high-pressure pulsed laser deposition". In: *Applied Physics A* 91.1 (2008), pp. 29–32.

[185] E. Fazio, F. Neri, R. Ruggeri, G. Sabatino, S. Trusso, and G. Mannino. "Structural properties of pulsed laser deposited SnOx thin films". In: *Applied Surface Science* 257.7 (2011), pp. 2520–2525.

[186] Z. W. Chen, J. K. L. Lai, and C. H. Shek. "Insights into microstructural evolution from nanocrystalline SnO_2 thin films prepared by pulsed laser deposition". In: *Phys. Rev. B* 70 (2004), p. 165314.

[187] A. Serventi, R. Dolbec, M. Khakani, R. Saint-Jacques, and D. Rickerby. "High-resolution transmission electron microscopy investigation of the nanostructure of undoped and Pt-doped nanocrystalline pulsed laser deposited SnO_2 thin films". In: *Journal of Physics and Chemistry of Solids* 64.11 (2003), pp. 2097–2103.

[188] Z. Chen, J. Lai, C. Shek, and H. Chen. "Production of amorphous tin oxide thin films and microstructural transformation induced by heat treatment". English. In: *Applied Physics A* 81.5 (2005), pp. 1073–1076.

[189] S. Sinha, R. Bhattacharya, S. Ray, and I. Manna. "Influence of deposition temperature on structure and morphology of nanostructured SnO_2 films synthesized by pulsed laser deposition". In: *Materials Letters* 65.2 (2011), pp. 146–149.

[190] S. Mehraj, M. S. Ansari, and Alimuddin. "Annealed SnO_2 thin films: Structural, electrical and their magnetic properties". In: *Thin Solid Films* 589 (2015), pp. 57–65.

[191] S. Trusso, B. Fazio, E. Fazio, F. Neri, and F. Barreca. "Influence of the plasma expansion dynamics on the structural properties of pulsed laser ablation deposited tin oxide thin films". In: *Thin Solid Films* 518.19 (2010), pp. 5409–5415.

[192] R. Lal, R. Grover, R. Vispute, R. Viswanathan, V. Godbole, and S. Ogale. "Sensor activity in pulsed laser deposited and ion implanted tin oxide thin films". In: *Thin Solid Films* 206.1–2 (1991), pp. 88–93.

[193] J. Hu, Y. Bando, Q. Liu, and D. Golberg. "Laser-Ablation Growth and Optical Properties of Wide and Long Single-Crystal SnO_2 Ribbons". In: *Advanced Functional Materials* 13.6 (2003), pp. 493–496.

[194] S. Yu, W. Zhang, L. Li, D. Xu, H. Dong, and Y. Jin. "Fabrication of p-type SnO_2 films via pulsed laser deposition method by using Sb as dopant". In: *Applied Surface Science* 286 (2013), pp. 417–420.

[195] Y. Porte, R. Maller, H. Faber, H. N. AlShareef, T. D. Anthopoulos, and M. A. McLachlan. “Exploring and controlling intrinsic defect formation in SnO_2 thin films”. In: *Journal of Materials Chemistry C* 4 (2016), pp. 758–765.

[196] J. Huotari, J. Lappalainen, J. Puustinen, and A. L. Spetz. “Gas sensing properties of pulsed laser deposited vanadium oxide thin films with various crystal structures”. In: *Sensors and Actuators B: Chemical* 187 (2013). Selected Papers from the 14th International Meeting on Chemical Sensors, pp. 386–394.

[197] J. Huotari, R. Bjorklund, J. Lappalainen, and A. L. Spetz. “Pulsed Laser Deposited Nanostructured Vanadium Oxide Thin Films Characterized as Ammonia Sensors”. In: *Sensors and Actuators B: Chemical* 217 (2015). Selected Papers from the 15th International Meeting on Chemical Sensors, 16-19 March 2014, Buenos Aires, Argentina, pp. 22–29.

[198] P. R. Willmott and J. R. Huber. “Pulsed laser vaporization and deposition”. In: *Reviews of Modern Physics* 72 (2000), pp. 315–328.

[199] E. György, I. Mihailescu, M. Kompitsas, and A. Giannoudakos. “Particulates-free Ta thin films obtained by pulsed laser deposition: the role of a second laser in the laser-induced plasma heating”. In: *Applied Surface Science* 195.1 (2002), pp. 270–276.

[200] R. Rusanov, H. Rank, J. Graf, T. Fuchs, R. Mueller-Fiedler, and O. Kraft. “Reliability of platinum electrodes and heating elements on SiO_2 insulation layers and membranes”. In: *Microelectronics Reliability* 55.9–10 (2015), pp. 1920–1925.

[201] U. Schmid and H. Seidel. “Influence of thermal annealing on the resistivity of titanium/platinum thin films”. In: *Journal of Vacuum Science & Technology, A* 24.6 (2006), pp. 2139–2146.

[202] V. Demarne and A. Grisel. “An integrated low-power thin-film CO gas sensor on silicon”. In: *Sensors and Actuators* 13.4 (1988), pp. 301–313.

[203] U. Dibbern. “A substrate for thin-film gas sensors in microelectronic technology”. In: *Sensors and Actuators B: Chemical* 2.1 (1990), pp. 63–70.

[204] D. Briand, A. Krauss, B. Van der Schoot, U. Weimar, N. Barsan, W. Göpel, and N. De Rooij. “Design and fabrication of high-temperature micro-hotplates for drop-coated gas sensors”. In: *Sens. Actuators B* 68.1 (2000), pp. 223–233.

[205] G. Sberveglieri, W. Hellmich, and G. Müller. “Silicon hotplates for metal oxide gas sensor elements”. In: *Microsystem Technologies* 3.4 (1997), pp. 183–190.

[206] P. Bhattacharyya. “Technological Journey Towards Reliable Microheater Development for MEMS Gas Sensors: A Review”. In: *IEEE Transactions on Device and Materials Reliability* 14 (2014), pp. 589–599.

[207] O. Bartels. “Entwicklung eines low-power Gassensorarrays unter Verwendung von dicken Opferschichten aus Porösem Silizium als Basis für eine selektive Gasdetektion”. PhD thesis. Universität Bremen, 2002.

[208] F. Solzbacher. “A new SiC/HfB_2 based micro hotplate for metal oxide gassensors”. PhD thesis. Technischen Universität Ilmenau, 2003.

[209] G. Wiche. “Metalloxid-Gassensoren mit Siliziumcarbid Micro-Hotplate”. PhD thesis. Technischen Universität Berlin, 2007.

[210] P. Walden, J. Kneer, S. Knobelspies, W. Kronast, U. Mescheder, and S. Palzer. “Micromachined Hotplate Platform for the Investigation of Ink-Jet Printed, Functionalized Metal Oxide Nanoparticles”. In: *Journal of Microelectromechanical Systems* 24.5 (2015), pp. 1384–1390.

[211] I. Elmi, S. Zampolli, E. Cozzani, F. Mancarella, and G. Cardinali. “Development of ultra-low-power consumption MOX sensors with ppb-level VOC detection capabilities for emerging applications”. In: *Sensors and Actuators B: Chemical* 135.1 (2008), pp. 342–351.

[212] Z. Dai, L. Xu, G. Duan, T. Li, H. Zhang, Y. Li, Y. Wang, Y. Wang, and W. Cai. “Fast-response, sensitivitive and low-powered chemosensors by fusing nanostructured porous thin film and IDEs-microheater chip”. In: *Scientific Reports* 3 (2013).

[213] A. Friedberger, P. Kreisl, E. Rose, G. Müller, G. Kühner, J. Wöllenstein, and H. Böttner. “Micromechanical fabrication of robust low-power metal oxide gas sensors”. In: *Sensors and Actuators B: Chemical* 93.1–3 (2003). Proceedings of the Ninth International Meeting on Chemical Sensors, pp. 345–349.

[214] S. Semancik, R. Cavicchi, M. Wheeler, J. Tiffany, G. Poirier, R. Walton, J. Suehle, B. Panchapakesan, and D. DeVoe. “Microhotplate platforms for chemical sensor research”. In: *Sensors and Actuators B: Chemical* 77.1–2 (2001). Proceeding of the Eighth International Meeting on Chemical Sensors IMCS-8 - Part 2, pp. 579–591.

[215] L. Sheng, Z. Tang, J. Wu, P. C. Chan, and J. K. Sin. “A low-power CMOS compatible integrated gas sensor using maskless tin oxide sputtering”. In: *Sensors and Actuators B: Chemical* 49.1–2 (1998), pp. 81–87.

[216] H. Seidel, L. Csepregi, A. Heuberger, and H. Baumgärtel. “Anisotropic etching of crystalline silicon in alkaline solutions I. Orientation dependence and behavior of passivation layers”. In: *Journal of the electrochemical society* 137.11 (1990), pp. 3612–3626.

[217] S. K. Fung, Z. Tang, P. C. Chan, J. K. Sin, and P. W. Cheung. “Thermal analysis and design of a micro-hotplate for integrated gas-sensor applications”. In: *Sensors and Actuators A: Physical* 54.1–3 (1996), pp. 482–487.

[218] F. Laermer and A. Schilp. “Method of anisotropically etching silicon”. US Patent 5,501,893. 1996.

[219] S. Z. Ali, F. Udrea, W. I. Milne, and J. W. Gardner. “Tungsten-based SOI microhotplates for smart gas sensors”. In: *Microelectromechanical Systems, Journal of* 17.6 (2008), pp. 1408–1417.

[220] R. Rusanov, J. Graf, H. Rank, T. Fuchs, and R. Mueller-Fiedler. “Reliability characterization of a soot particle sensor”. In: *DTIP2014 Symposium on Design, Test, Integration & Packaging of MEMS/MOEMS*. 2014.

[221] P. A. Koellensperger, W. J. Karl, M. M. Ahmad, W. T. Pike, and M. Green. “Patterning of platinum (Pt) thin films by chemical wet etching in Aqua Regia”. In: *Journal of Micromechanics and Microengineering* 22.6 (2012), p. 067001.

[222] P. Norgate and V. Hammond. “Ion beam etching”. In: *Physics in Technology* 5.3 (1974), p. 186.

[223] H.-W. Kim, B.-S. Ju, C.-J. Kang, and J.-T. Moon. “A study on the Pt electrode etching for 0.15 μm technologies”. In: *Microelectronic Engineering* 65.1 (2003), pp. 185–195.

[224] W. Daves. *Silicon Carbide Field-Effect Transistor (FET) Transducers for Harsh Environment Applications*. Shaker Verlag, 2013.

[225] A. Learn. “Evolution and current status of aluminum metallization”. In: *J. Electrochem. Soc.* 123.6 (1976), pp. 894–906.

[226] L. Bissi, M. Cicioni, P. Placidi, S. Zampolli, I. Elmi, and A. Scorzoni. “A programmable interface circuit for an ultralow power gas sensor”. In: *IEEE Trans. Instrum. Meas.* 60.1 (2011), pp. 282–289.

[227] T. Serikawa and S. Shirai. “Modelling of lift-off sputter deposition and application to fabrication of a microlens”. In: *Thin Solid Films* 281–282 (1996), pp. 246–248.

[228] W. Westwood. “Calculation of deposition rates in diode sputtering systems”. In: *Journal of Vacuum Science and Technology* 15.1 (1978), pp. 1–9.

[229] M. Spak, D. Mammato, S. Jain, and D. Durham. “Mechanism and lithographic evaluation of image reversal in AZ 5214 photoresist”. In: *Seventh International Technical Conference on Photopolymers, Ellenville, New York*. Vol. 120. 1985.

[230] S. MacDonald, H. Ito, and C. G. Willson. “Advances in the design of organic resist materials”. In: *Microelectronic Engineering* 1.4 (1983), pp. 269–293.

[231] Y. Chen, K. Peng, and Z. Cui. “A lift-off process for high resolution patterns using PMMA/LOR resist stack”. In: *Microelectronic Engineering* 73–74 (2004), pp. 278–281.

[232] L. Ouattara, M. Knutzen, S. Keller, M. Hansen, and A. Boisen. “Double layer resist process scheme for metal lift-off with application in inductive heating of microstructures”. In: *Microelectron. Eng.* 87.5–8 (2010). The 35th International Conference on Micro- and Nano-Engineering (MNE), pp. 1226–1228.

[233] E. Preiss, A. Krauss, and H. Seidel. “Comparative study of large area pulsed laser deposited metal oxides for gas sensors applications”. In: *Solid-State Sensors, Actuators and Microsystems (TRANSDUCERS), 18th International Conference on*. June 2015, pp. 1499–1502.

[234] E. M. Preiss, A. Krauss, and H. Seidel. “Sputtered Pt electrode structures with smoothly tapered edges by bi-layer resist lift-off”. In: *Thin Solid Films* (2015), pp. 158–164.

[235] X. Xia, H. Yang, Y. Sun, Z. Wang, L. Wang, Z. Cui, and C. Gu. “Fabrication of terahertz metamaterials using S1813/LOR stack by lift-off”. In: *Microelectronic Engineering* 85.5–6 (2008), pp. 1433–1436.

[236] I. Safi. “Recent aspects concerning DC reactive magnetron sputtering of thin films: a review”. In: *Surface and Coatings Technology* 127.2–3 (2000), pp. 203–218.

[237] P. Kelly and R. Arnell. “Magnetron sputtering: a review of recent developments and applications”. In: *Vacuum* 56.3 (2000), pp. 159–172.

[238] J. J. Broekmaat, J. M. Dekkers, and J. A. Janssens. “Device for projecting an image on a surface and device for moving said image”. US Patent 2011/0292354. 2011.

[239] D. H. A. Blank, M. Dekkers, and G. Rijnders. “Pulsed laser deposition in Twente: from research tool towards industrial deposition”. In: *Journal of Physics D: Applied Physics* 47.3 (2014), p. 034006.

[240] L. M. Doeswijk. *Pulsed Laser Deposition of Oxides on Silicon: Exploring Their Passivating Qualities*. 2002.

[241] R. G. Gordon. “Criteria for Choosing Transparent Conductors”. In: *MRS Bulletin* 25 (2000), pp. 52–57.

[242] E. M. Preiß, A. Krauß, V. Kekkonen, N. Barsan, and H. Seidel. “Characterization of WO_3 thin films prepared by picosecond laser deposition for gas sensing”. In: *Sensors and Actuators B: Chemical* 248 (2017), pp. 153–159.

[243] D. S. Perloff, F. E. Wahl, and J. Conragan. “Four-Point Sheet Resistance Measurements of Semiconductor Doping Uniformity”. In: *Journal of The Electrochemical Society* 124.4 (1977), pp. 582–590.

[244] R. Rusanov. *Characterization and Reliability Testing of Thin-Film Materials for Robust MEMS Sensors*. Berichte aus der Mikrosystemtechnik. Shaker Verlag, 2016.

[245] G. K. Reeves and H. B. Harrison. “Obtaining the specific contact resistance from transmission line model measurements”. In: *IEEE Electron Device Letters* 3.5 (1982), pp. 111–113.

[246] U. Hoefer, K. Steiner, and E. Wagner. “Contact and sheet resistance of SnO_2 thin films from transmission-line model measurements”. In: *Sensors and Actuators B: Chemical* 26.1 (1995), pp. 59–63.

[247] R. S. Zeisluft. “Charakterisierung und Modellierung des Leistungsbedarfs mikroskalierter Gassensoren”. MA thesis. Karlsruher Institut für Technologie, 2016.

[248] T. Rogge. *Praktikumsbericht: Herstellung und Charakterisierung von gassensitiven Schichten*. Tech. rep. Robert Bosch GmbH, 2015.

[249] D. Degler, H. W. P. de Carvalho, K. Kvashnina, J.-D. Grunwaldt, U. Weimar, and N. Barsan. “Structure and chemistry of surface-doped Pt:SnO_2 gas sensing materials”. In: *RSC Advances* 6.34 (2016), pp. 28149–28155.

[250] E. M. Preiss, A. Krauss, L. Spiess, T. Kups, and H. Seidel. “TEM and GIXRD investigations on SnO_2, unpublished”.

[251] A. Franz. “Komplexuntersuchungen an Metalloxidschichten für die Sensorik”. MA thesis. Technische Universität Ilmenau, 2016.

[252] C. Körber. “Herstellung und Charakterisierung polykristalliner kathodenzerstäubter Zinnoxid-Dünnschichten”. PhD thesis. Technische Universität Darmstadt, 2010.

[253] T. Tisone and J. Bindell. “Step coverage in the vacuum deposition of thin metal films”. In: *J. Vac. Sci. Technol.* 11.1 (Jan. 1974), pp. 72–76.

[254] K. Green, D. Hayden, D. Juliano, and D. Ruzic. “Determination of flux ionization fraction using a quartz crystal microbalance and a gridded energy analyzer in an ionized magnetron sputtering system”. In: *Rev. Sci. Instrum.* 68.12 (1997), pp. 4555–4560.

[255] Q. Fan, X. Chen, and Y. Zhang. “Computer simulation of film thickness distribution in symmetrical magnet magnetron sputtering”. In: *Vacuum* 46.3 (1995), pp. 229–232.

[256] R. Gnaedinger. “Some calculations of the thickness distribution of films deposited from large area sputtering sources”. In: *J. Vac. Sci. Technol.* 6.3 (1969), pp. 355–362.

[257] H. Gnaser. *Energy and angular distributions of sputtered species*. Vol. 110. Top. Appl. Phys. Springer Berlin Heidelberg, 2007, pp. 231–328.

[258] I. Blech. “Evaporated film profiles over steps in substrates”. In: *Thin Solid Films* 6.2 (1970), pp. 113–118.

[259] J. Bindell and T. Tisone. “Step coverage from an extended sputtering source”. In: *Thin Solid Films* 23.1 (1974), pp. 31–47.

[260] S. Swann. “Film thickness distribution in magnetron sputtering”. In: *Vacuum* 38.8–10 (1988), pp. 791–794.

[261] E. M. Preiß, T. Rogge, A. Krauß, and H. Seidel. “Tin oxide-based thin films prepared by pulsed laser deposition for gas sensing”. In: *Sensors and Actuators B: Chemical* 236 (2016), pp. 865–873.

[262] A. Oprea, E. Moretton, N. Barsan, W. J. Becker, J. Wöllenstein, and U. Weimar. “Conduction model of SnO_2 thin films based on conductance and Hall effect measurements”. In: *Journal of Applied Physics* 100.3, 033716 (2006).

[263] G. Korotcenkov. “The role of morphology and crystallographic structure of metal oxides in response of conductometric-type gas sensors”. In: *Materials Science and Engineering: R: Reports* 61.1 (2008), pp. 1–39.

[264] G. J. McCarthy and J. M. Welton. “X-Ray Diffraction Data for SnO_2. An Illustration of the New Powder Data Evaluation Methods”. In: *Powder Diffraction* 4 (03 1989), pp. 156–159.

[265] P. Hidalgo, R. H. Castro, A. C. Coelho, and D. Gouvêa. “Surface segregation and consequent SO_2 sensor response in SnO_2-NiO”. In: *Chemistry of materials* 17.16 (2005), pp. 4149–4153.

[266] K. Jain, R. Pant, and S. Lakshmikumar. “Effect of Ni doping on thick film SnO_2 gas sensor”. In: *Sensors and Actuators B: Chemical* 113.2 (2006). Special Issue - In honour of Professor Karl Cammann, pp. 823–829.

[267] F. Gyger, A. Sackmann, M. Hübner, P. Bockstaller, D. Gerthsen, H. Lichtenberg, J.-D. Grunwaldt, N. Barsan, U. Weimar, and C. Feldmann. “Pd@SnO_2 and SnO_2@Pd Core@Shell Nanocomposite Sensors”. In: *Particle & Particle Systems Characterization* 31.5 (2014), pp. 591–596.

[268] W. Schmid, N. Barsan, and U. Weimar. “Sensing of hydrocarbons and CO in low oxygen conditions with tin dioxide sensors: possible conversion paths”. In: *Sensors and Actuators B: Chemical* 103.1–2 (2004). The 17th Euopean Conference on Solid-State Transducers, University of Minho, Guimares, Portugal, September 21-24, 2003, pp. 362–368.

[269] D. Koziej, N. Barsan, K. Shimanoe, N. Yamazoe, J. Szuber, and U. Weimar. “Spectroscopic insights into CO sensing of undoped and palladium doped tin dioxide sensors derived from hydrothermally treated tin oxide sol”. In: *Sensors and Actuators B: Chemical* 118.1-2 (2006). EUROSENSORS XIX - The 19th European Conference on Solid-State Transducers, pp. 98–104.

[270] N. Ma, K. Suematsu, M. Yuasa, and K. Shimanoe. “Pd Size Effect on the Gas Sensing Properties of Pd-Loaded SnO_2 in Humid Atmosphere”. In: *ACS Applied Materials & Interfaces* 7.28 (2015). PMID: 26111855, pp. 15618–15625.

[271] K. Grossmann, R. G. Pavelko, N. Barsan, and U. Weimar. “Interplay of H_2, water vapor and oxygenat the surface of SnO_2 based gas sensors - An operando investigation utilizing deuterated gases”. In: *Sensors and Actuators B: Chemical* 166–167 (2012), pp. 787–793.

[272] W. Yu-De, C. Zhan-Xian, L. Yan-Feng, Z. Zhen-Lai, and W. Xing-Hui. “Electrical and gas-sensing properties of WO_3 semiconductor material”. In: *Solid-State Electronics* 45.5 (2001), pp. 639–644.

[273] M. Penza, M. Tagliente, L. Mirenghi, C. Gerardi, C. Martucci, and G. Cassano. “Tungsten trioxide (WO_3) sputtered thin films for a NOx gas sensor”. In: *Sensors and Actuators B: Chemical* 50.1 (1998), pp. 9–18.

[274] C. Wang, X. Li, C. Feng, Y. Sun, and G. Lu. “Nanosheets assembled hierarchical flower-like WO_3 nanostructures: Synthesis, characterization, and their gas sensing properties”. In: *Sensors and Actuators B: Chemical* 210 (2015), pp. 75–81.

[275] Y. Zhao, Z.-C. Feng, and Y. Liang. “Pulsed laser deposition of WO_3-base film for NO_2 gas sensor application”. In: *Sensors and Actuators B: Chemical* 66 (2000), pp. 171–173.

[276] F. Mitsugi, E. Hiraiwa, T. Ikegami, and K. Ebihara. “Pulsed laser deposited WO_3 thin films for gas sensor”. In: *Surface and Coatings Technology* 169–170 (2003). Proceedings of Frontiers of Surface Engineering, pp. 553–556.

[277] J. Polleux, A. Gurlo, N. Barsan, U. Weimar, M. Antonietti, and M. Niederberger. “Template-Free Synthesis and Assembly of Single-Crystalline Tungsten Oxide Nanowires and their Gas-Sensing Properties”. In: *Angewandte Chemie* 118.2 (2006), pp. 267–271.

[278] V. Kekkonen, S. Chaudhuri, F. Clarke, J. Kaisto, J. Liimatainen, S. K. Pandian, J. Piirto, M. Siltanen, and A. Zolotukhin. “Picosecond pulsed laser deposition of metal-oxide sensing layers with controllable porosity for gas sensor applications”. In: *Applied Physics A* 122.3 (2016), pp. 1–7.

[279] J. Huotari, V. Kekkonen, T. Haapalainen, M. Leidinger, T. Sauerwald, J. Puustinen, J. Liimatainen, and J. Lappalainen. “Pulsed laser deposition of metal oxide nanostructures for highly sensitive gas sensor applications”. In: *Sensors and Actuators B: Chemical* (2016), pp. 978–987.

[280] A. Staerz, C. Berthold, T. Russ, S. Wicker, U. Weimar, and N. Barsan. “The oxidizing effect of humidity on WO_3 based sensors”. In: *Sensors and Actuators B: Chemical* 237 (2016), pp. 54–58.

[281] J. Huotari, J. Lappalainen, J. Puustinen, T. Baur, C. Alepee, T. Haapalainen, S. Komulainen, J. Pylvaenaeinen, and A. L. Spetz. “Pulsed Laser Deposition of Metal Oxide Nanoparticles, Agglomerates, and Nanotrees for Chemical Sensors”. In: *Procedia Engineering* 120 (2015). Eurosensors 2015, pp. 1158–1161.

[282] J. Puigcorbe, D. Vogel, B. Michel, A. Vila, I. Gracia, C. Cane, and J. Morante. “Thermal and mechanical analysis of micromachined gas sensors”. In: *Journal of Micromechanics and Microengineering* 13.5 (2003), p. 548.

[283] M. Schweizer-Berberich, S. Strathmann, U. Weimar, R. Sharma, A. Seube, A. Peyre-Lavigne, and W. Göpel. “Strategies to avoid VOC cross-sensitivity of SnO_2-based CO sensors”. In: *Sensors and Actuators B: Chemical* 58.1 (1999), pp. 318–324.

[284] A. Krauss and E. Preiss. “Herstellungsverfahren für eine mikromechanische Sensorvorrichtung und entsprechende mikromechanische Sensorvorrichtung”. Patent application *pending*. 2017.

Gassensoren in Smartphones und anderen mobilen Geräten haben das Potential, zukünftig Lebensqualität und Sicherheit zu verbessern. Dafür ist ein hoher Grad an Miniaturisierung und die Reduzierung der Leistungsaufnahme notwendig. In dieser Arbeit wurden verschiedene Aspekte miniaturisierter, resistiver COSensoren auf Basis von Metalloxiden (MOX) untersucht. Herstellung erfolgte mit gepulster Laserabscheidung (PLD) auf Platinstrukturen, die mit einem Lift-Off-Prozess strukturiert wurden. Per Simulation und Experiment wurden Einflüsse der Lackgeometrie auf die Metallstruktur aufgezeigt. Bei den untersuchten MOX-Dünnschichten lag der Fokus auf SnO_2. Dessen elektrische und gassensitive Eigenschaften hängen stark von den Abscheidungsbedingungen ab: Höhere Abscheidungsdrücke (>10 Pa) führen zu höheren Grundwiderständen sowie zu einem höheren Signal für CO in trockener Luft. Diese Eigenschaften korrelieren mit der nanoporösen Morphologie des Materials. Bei Messungen in feuchter Luft reduzierte sich das CO-Signal im Vergleich zu trockener Luft. Durch den per Sputtern aufgebrachten Zusatz von Edelmetallen, insbesondere von Palladium (Pd), konnten die Eigenschaften deutlich verbessert werden. COSensitivität in feuchter Luft konnte für hochporöses WO3 ebenfalls gezeigt werden. In einer Parameterstudie wurde in Experiment und Simulation zudem der Einfluss der geheizten Membrangeometrie auf die Leistungsaufnahme des Sensors untersucht.